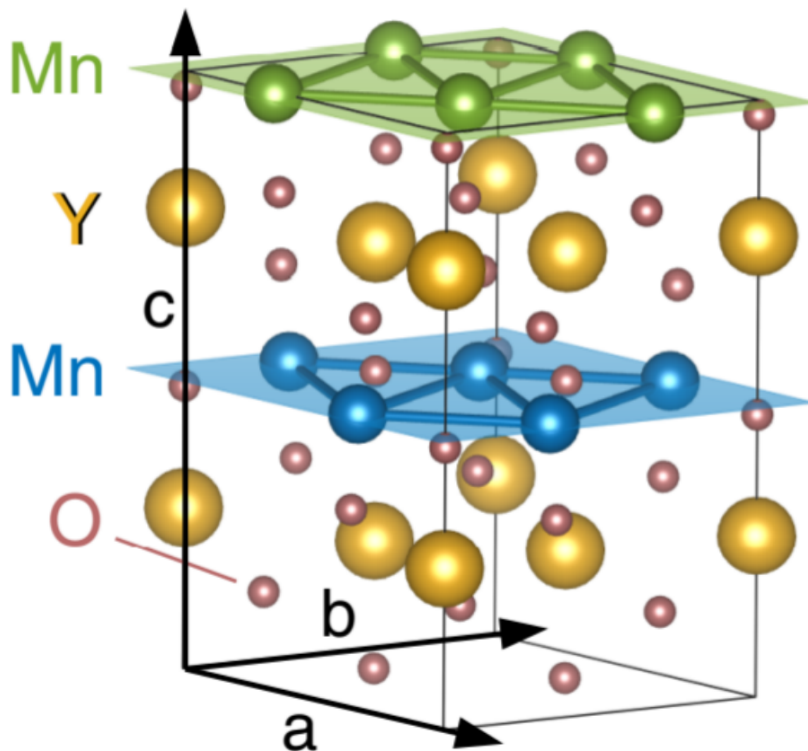




The Critical Magnetic Phase Transition of h -YMnO₃



Master Thesis

Niels Christian Rand Momsen
Niels Bohr Institute

Supervisor: Prof. Dr. Kim Lefmann, Niels Bohr Institute

Handed in: September 30, 2020

Abstract

In this thesis the critical Néel temperature, T_N , of the magnetic critical phase transition and the associated critical exponents of h -YMnO₃ have been measured using elastic and inelastic neutron scattering. The thesis introduces relevant theoretical concepts related to crystal structures, magnetism, critical phase transitions and their associated critical exponents, as well as the theory of neutron scattering used to carry out the measurements in this work.

The Néel temperature, $T_N = 71.48 \pm 0.04$ K, were computed by fitting the Magnetization vs temperature data from the elastic neutron scattering data measured at the $\mathbf{q} = (0\bar{1}0)$ Bragg-peak by fitting the critical range to a power law relation. The critical range were estimated from plotting the data on double logarithmic plots, which should make the critical range appear linear. The power law fits to the magnetization in addition to the intensity and width of the critical scattering occurring close to T_N yielded their corresponding critical exponents. These are $\beta = 0.179 \pm 0.002$ associated with the magnetization, $\gamma = 1.063 \pm 0.002$ and $\gamma = 1.12 \pm 0.02$ from the intensity of the critical scattering above and below T_N respectively, and $\nu = 4.1 \pm 1.0$ and $\nu = 6.3 \pm 0.2$ associated with the width of the critical scattering again above and below T_N respectively.

The Néel temperature and the values of the critical exponents match those reported in the literature quite well, except for ν which is much too high. The critical exponents does not match any known universality class and as such support the notion that a new universality class of triangular frustrated systems is needed.

The inelastic neutron scattering data revealed two visually distinct magnon modes at $\hbar\omega = 2.3$ meV and $\hbar\omega = 5.4$ meV respectively at base temperature. As the temperature increases the excitation gab of the lower magnon mode decreases until it reaches 0 meV at T_N . The temperature dependence of this excitation gab were fitted to a power law and its critical exponent, suspected of being similar to β from the elastic measurements, gave a value of $\beta = 0.28 \pm 0.08$. These two β 's are within two standard deviations of each other and are assumed similar given the data.

The inelastic measurements also yielded two novel critical exponents, $\zeta = 0.72 \pm 0.07$ and $\rho = 0.45 \pm 0.02$, associated with the temperature dependence of the intensity and width of the quasi-elastic scattering at $\hbar = 0$ meV. To the best of the authors knowledge these have not been measured anywhere before. Their significance, if any, is unknown.

Finally a new method of estimating the critical range of the elastic data is proposed in this thesis. This method is based on systemically varying the temperature range of the supposed critical region and then computing the values of T_N and/or β for each range. Based on the analysis in this thesis the values one obtains becomes constant within the correct critical range and when plotted as done here seems to reach a plateau, indicating that the true critical range has been found.

Resumé

I dette speciale måles den kritiske Néel temperatur, T_N , for den magnetiske kritiske faseovergang i h -YMnO₃ og de associerede kritiske eksponenter med både elastisk og inelastisk neutronspreddning. Afhandlingen lægger ud med at give en introduktion til den relevante teori om magnetisme, krystaller, kritiske faseovergange og kritiske eksponenter og introducerer også den teoretiske baggrund for neutronspreddning, der er blevet brugt til at udføre målingerne i dette speciale.

Néel temperaturen blev målt til $T_N = 71.48 \pm 0.04$ K ud fra den elastiske neutron spredning ved at lave et potenslovfit af magnetiseringen som funktion af temperaturen målt ved Bragg-peaket ved $\mathbf{q} = (0\bar{1}0)$ i det kritiske område. Det kritiske område blev fundet ved at lave et dobbelt logaritmisk plot af data, hvori den kritiske region burde ligne en lige linje. Udover at bestemme T_N på denne måde så gav dette fit også den kritiske eksponent $\beta = 0.179 \pm 0.002$. Den kritiske eksponent γ , der findes ved at fitte en potenslov til intensiteten af den kritiske spredning som funktion af temperatur, gav to forskellige værdier på hver side af T_N , nemlig $\gamma = 1.063 \pm 0.002$ og $\gamma = 1.12 \pm 0.02$ afhængig af om det var over eller under T_N . På samme måde blev den kritiske eksponent ν , der er associeret med bredden af den kritiske spredning som funktion af temperatur bestemt både over $\nu = 4.1 \pm 1.0$ og under $\nu = 6.3 \pm 0.2$ den kritiske temperatur T_N .

Den kritiske temperatur samt eksponenterne β og γ passer alle overens med resultaterne fra tidligere eksperimentelle studier, mens ν er væsentligt over, hvad den burde være ifølge alle tidligere studier og teoretiske modeller. Værdierne for β og γ stemmer dog ikke overens med de forventede værdier i nogen kendte universalitetsklasser, hvorfor der nok er behov for at lave en ny universalitetsklasse specifikt for frustrerede trekantsystemer som dette.

Målingerne udført med uelastisk neutron spredning viser to klart adskilte magnon excitationer med energier på hhv $\hbar\omega = 2.3$ meV og $\hbar\omega = 5.4$ meV ved den laveste temperatur, der blev taget data ved. Når temperaturen øges, så reduceres den laveste magnons excitationens energi, indtil den når $\hbar\omega = 0$, hvilket sker, når temperaturen rammer T_N . Dette excitationsgab kan også fittes til en potenslov. Den kritiske eksponent man får ud af det, bør være den samme β fra de elastiske neutronspreddningsmålinger. Denne nye $\beta = 0.28 \pm 0.08$ passer inden for to standardafvigelser med β fra de elastiske målinger, og derfor kan det med god sandsynlighed konkluderes, at de to er ens.

De nye kritiske eksponenter $\zeta = 0.72 \pm 0.07$ og $\rho = 0.45 \pm 0.02$ blev også fundet ud fra de uelastiske neutronspreddningsmålinger. Intensiteten som funktion af temperatur af det quasielastiske signal omkring $\hbar\omega = 0$ udviklede sig også som en potenslov og gav værdien for ζ , mens bredden af den samme spredning gav ρ . Disse to eksponenter er, så vidt forfatteren er orienteret, ukendte i litteraturen, og der er derfor tale om to helt nye kritiske eksponenter.

Afslutningsvist introduceres der i dette speciale en ny og måske bedre metode til at bestemme den kritiske region. Metoden er baseret på systematisk at variere den region, der fittes til en potenslov. For en given maksimal fittemperatur plottes de værdier for T_N og/eller β , som opnås, når man varierer den laveste fittemperatur. Denne procedure gentages herefter for en række nye maksimale

temperaturer. Med udgangspunkt i dette speciales analyse kan det konkluderes, at de værdier, der opnås for T_N og/eller β , når et konstant niveau, når de plottes på denne facon og former et plateau. Dette plateau indikerer dermed den sande kritiske region.

Acknowledgments

First of all I would like to extend my warm thanks to my supervisor Kim Lefmann who, despite all my setbacks and issues throughout my time as his masters student, always were willing to offer guidance and counseling in matters related to this thesis and beyond. Secondly I would like to thank Sonja Holm-Dahlin for thorough scientific advice and proof reading many chapters in this thesis and for good company on the beam times I went on. Sofie Janas deserves thanks as well for providing a great deal of scientific insight related to several topics in this thesis. Thanks to Else Nielsen, Günther Momsen, and Isabella Christensen for correcting (hopefully) all my spelling mistakes. A final thanks to both Paul Scherrer Institute for supplying the facilities to conduct these experiments and to DANSCATT for funding my travel expenses.



Contents

List of Figures	vi
List of Tables	viii
1 Introduction	1
2 Theoretical Background	3
2.1 Crystals	3
2.2 Magnetism	5
2.2.1 Magnetic moments	7
2.2.2 The Heisenberg model	8
2.2.3 Other models	10
2.2.4 Magnetic structures	10
2.3 Excitations in Crystals	12
2.3.1 Phonons	12
2.3.2 Magnons	14
2.4 Multiferroics	15
2.5 Critical Phase Transitions	18
2.5.1 Landau theory	21
2.5.2 Critical exponents	23
2.5.3 Universality	24
2.5.4 Scaling	24
3 Methods	26
3.1 Properties of the Neutron	26
3.2 Why Neutrons?	27
3.3 Neutron Scattering	28
3.3.1 Differential scattering cross section	28
3.3.2 Semi-classical description of elastic scattering	29
3.3.3 Inelastic neutron scattering	32
3.3.4 One-phonon cross section	32
3.3.5 Magnetic neutron scattering	33
3.3.6 Critical scattering	35
3.4 Neutron Instrumentation	36
3.4.1 Neutron production	36
3.4.2 The moderator	36
3.4.3 Neutron guides	37
3.4.4 Monochromators	38

3.4.5	Filters, slits and collimators	38
3.4.6	Neutron detectors	39
3.5	Neutron Spectroscopy	40
3.5.1	Triple axis spectrometers	40
3.5.2	Instrument resolution	42
3.5.3	RITA-II	43
3.6	Line Forms	43
3.7	Introduction to YMnO_3	46
3.8	Experimental Setup	49
3.8.1	The sample	49
3.8.2	Measurements	49
4	Experimental Results	51
4.1	Results of the Elastic Measurements	51
4.1.1	Fitting the line forms	51
4.1.2	The instrument resolution function	51
4.1.3	Fitting the critical scattering	55
4.1.4	The Néel temperature and critical exponents	56
4.1.5	Variational analysis of the temperature range used for fitting T_N and β	61
4.2	Results of the Inelastic Neutron Scattering Measurements	65
4.2.1	Fitting the magnon	65
4.2.2	Finding β using the magnon	66
4.2.3	Novel critical exponents	66
5	Summarizing Discussion and Conclusion	72
5.1	Summary of the Results	72
5.2	The Néel Temperature	73
5.3	Critical Exponents	74
5.4	The Fitting Method in Light of the Variational Analysis	75
6	Outlook	76
7	Bibliography	77
A		82

List of Figures

2.1	Examples of crystal lattices	4
2.2	Lattice spacing	4
2.3	Brillouin zones	5
2.4	Examples of magnetic structures	6
2.5	Magnetic structures in reciprocal space	6
2.6	ferro- and antiferromagnetic lattices	11
2.7	Geometrically frustrated lattice	12
2.8	Longitudinal and transverse phonons	13
2.9	Phonon dispersion relations	14
2.10	Spin waves	15
2.11	Magnon dispersion relations	16
2.12	ferroic couplings and symmetry	17
2.13	Multiferroic couplings	17
2.14	Phase diagram of water	19
2.15	Illustration of a critical phase transition	20
2.16	Illustration of the critical region	23
3.1	Illustration of the scattering geometry	31
3.2	Production of neutrons	37
3.3	Neutron Guides	38
3.4	Picture of a neutron slit and a soller collimator	39
3.5	Sketch of a triple axis spectrometer	41
3.6	Measured resolution ellipsoids	42
3.7	Resolution ellipsoid and dispersions	43
3.8	Sketh of RITA-II	44
3.9	unit cell of h -YMnO ₃	47
3.10	Phonon and magnon dispersion relations in h -YMnO ₃	48
3.11	Sample picture	49
4.1	Resoluton function of YMnO ₃	53
4.2	Log plots of the resolution function of YMnO ₃	54
4.3	Scans of YMnO ₃ Bragg peak	55
4.4	Double logarithmic plots	57
4.5	Magnetization versus temperature	58
4.6	The critical scattering	59
4.7	Power law fit of the magnetization versus temperature	60
4.8	Magnetization and critical scattering fits close to T_N	60
4.9	Width of the critical scattering	61

4.10	Variational analysis	62
4.11	Sensitivity analysis	63
4.12	variational analysis, zoomed	64
4.13	Inelastic neutron scattering data fits	67
4.14	excitation gap	68
4.15	Quasi-elastic intensity	69
4.16	Width of the quasi-elastic scattering	70
A.1	Magnon fitting parameters	82

List of Tables

3.1	Critical temperatures and exponents	48
4.1	reduced χ^2 values of resolution functions	52
4.2	Results	71

Chapter 1

Introduction

The study of the properties of materials is one of the most relevant branches of science to the lives of the general population. The fact that historians have named many of the early epochs of human history after the new dominant material used in them, namely the stone, bronze and iron ages, show the significance this branch of science can have on the society. More recent inventions such as computers, jet airplanes, plastics, photo voltaic cells, and many more are tied to advancements in materials science. The information age we live in today for an example is to a large degree made possible by the microchip which relies on the developments of solid state semiconductors in the decades following the 2nd World War.

Since then many new materials with exotic properties have emerged such as the superconductors, nano materials, graphene and so on. This thesis will focus on one material called YMnO_3 from a group of materials with exotic properties called multiferroics. Multiferroics are classified as being materials which have a coupling between the order parameters of two or all three ferroic properties namely the ferromagnetism, ferroelectricity and ferroelasticity. This makes it possible to e.g. induce a magnetization by applying an electric field or squeezing the material. Multiferroics are a rare occurrence in nature because the various ferroic properties are mutually exclusive in most materials.

Multiferroics are however of great interest both scientifically as well as in the industry, because the coupling of these order parameters can be used in many applications such as actuators, multi-memory devices, and transducers [1, 2].

As the temperature of a material changes it can undergo changes from one distinct phase to another. This is probably best known from water which can change back and forth from solid ice, to liquid water, and finally to air as steam by changing the temperature of the material. Phase changes do not however need to be as visually obvious. If a common refrigerator magnet is heated above a certain temperature threshold it will suddenly stop being magnetic, even though it is still a solid both before and after. This is another and much more subtle form of phase transition, where the change of state happens without any visual trace.

All magnets undergo phase transition from a magnetically ordered phase to one of disorder when the temperature increases. This is because macroscopic

magnetism, as seen in a refrigerator magnet, stems from the ordering of individual atomic magnets situated on each of the magnetic ions within the material. Below a certain critical temperature all these atomic magnets align with each other thus creating a macroscopic magnetic structure. This alignment or ordering can be complicated, and does not necessarily mean that a magnetic material will be macroscopically magnetic, in fact this is rarely the case as one of the most common ways for magnetic materials to order is to align all the atomic magnets anti-parallel with one another in pairs. This means that the net magnetic moment of each atomic magnet is exactly canceled by the anti-parallel magnetic moment of its neighbour thereby rendering the macroscopic material seemingly nonmagnetic. If the temperature is increased enough so that the thermal energy exceeds that of the exchange energy between the atomic magnets, the magnetic structure is broken and all the tiny magnets within the material will orient themselves randomly.

When water transitions from one phase to another there is an energy requirement, called latent heat, to transition, e.g. you can have ice cubes in a glass of water on a hot day, and the ice cubes will only slowly melt because of the latent heat required to melt the ice. For magnets there is no latent heat requirement, meaning that at the critical temperature the whole material will very rapidly transition from one phase to the next. The phase transitions of water are called 1st order phase transitions, while that of magnets are called 2nd order phase transition, continuous phase transition, or critical phase transitions. The critical magnetic phase transition of YMnO_3 will be one of the main topics of this thesis.

The study of magnetism is rich. One of the most efficient techniques for studying magnetism is neutron scattering. Neutrons are uniquely suited to the study of magnetism because they are electrically neutral, but carries a magnetic moment. This means that they can interact with magnetic structures, while not being influenced by any electric fields in the vicinity. In addition the neutron interacts fairly weakly with matter, meaning that it can penetrate deep into materials and thus it is excellent to study the three dimensional physical and magnetic structure of materials. Further the energy of the neutron can be tuned by, such that it is of the same order of magnitude as the dynamic excitations of the material allowing one to study these dynamics in great detail as well. A significant portion of this thesis will be explaining the art of neutron scattering and how it can be utilized to study especially magnetism.

It is the goal of this thesis to determine the critical temperature at which the magnetic phase transition occurs for YMnO_3 , in addition some of the critical order parameters associated with the phase transition will also be determined. The behavior of spin waves as a function of temperature will also be investigated and their critical parameters compared to that of the phase transition.

This study will reanalyze the same data as were used in a recent article published in Quantum Beam Science by Holm-Dahlin et al. [3].

Chapter 2

Theoretical Background

This section introduces crystal structures and magnetism. In addition the theory of excitations of both physical and magnetic structures are introduced as well as critical phase transitions and their associated critical exponents.

2.1 Crystals

A crystal is formed when atoms order in repeated patterns. The basic unit which repeats itself is called the unit cell, and the lattice of the crystal is created by translating the length of a lattice vector and then placing a new unit cell. In 3 dimensions you can naturally translate along 3 different axes, each axis is represented by a vector which will be known as \mathbf{a} , \mathbf{b} , and \mathbf{c} and therefore the volume V of the unit cell is

$$V = \mathbf{a} \cdot \mathbf{b} \times \mathbf{c} \quad (2.1.1)$$

The crystal will look similar when you translate any integer number of lattice vectors from your origin \mathbf{r} , such that

$$\mathbf{r}' = \mathbf{r} + u_1\mathbf{a} + u_2\mathbf{b} + u_3\mathbf{c} \quad (2.1.2)$$

where \mathbf{r}' is the new site and u_1 , u_2 , and u_3 are integers [4].

Each unit cell contains a number lattice points where the atoms that make up the crystal will be situated, such that at each lattice point an atom or a group of atoms is placed, the atom or group of atoms placed at these points is known as the basis of the crystal.

The simplest unit cell, that of the simple cubic cell, has a lattice point on each corner of the unit cell, see figure 2.1 (a). The angles between the lattice vectors are denoted α , β , and γ . In total 14 lattice types exists in 3 dimensions, there is 1 triclinic, 2 monoclinic, 4 orthorhombic, 2 tetragonal, 3 cubic, 1 trigonal, and 1 hexagonal [6]. The triclinic and hexagonal are shown in figure 2.1 (b) and (c). A total of 230 space groups exists which describes all possible symmetries within the crystal. This is of great value, since the symmetries of a crystal determines which reflections can occur within the crystal.

When conducting a scattering experiment you measure the reciprocal lattice. like the real lattice, the reciprocal lattice is made up of three vectors \mathbf{a}^* , \mathbf{b}^* ,

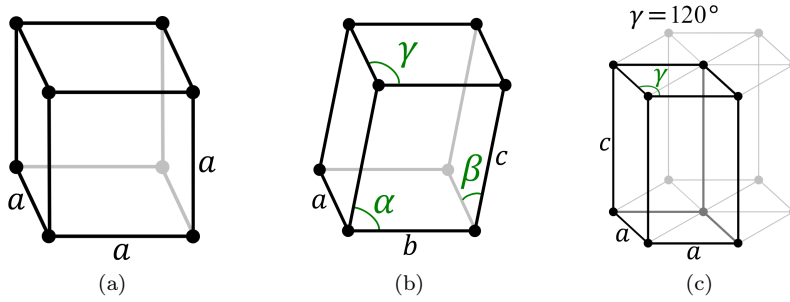


Figure 2.1: Above is shown 3 examples of simple crystal lattices, black dots denote lattice points. **(a)** a simple cubic structure with 1 lattice point at each corner, for a cubic lattice $a = b = c$, and $\alpha = \beta = \gamma = 90^\circ$. **(b)** The triclinic lattice, where $a \neq b \neq c$ and $\alpha \neq \beta \neq \gamma$. **(c)** The hexagonal where $a = b$, but c has a different length and $\alpha = \beta = 90^\circ$ and $\gamma = 120^\circ$. from [5]

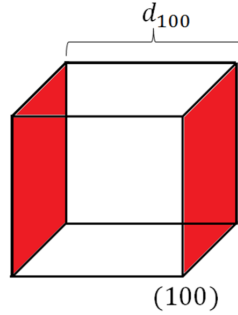


Figure 2.2: Lattice spacing in a simple cubic crystal structure. d_{100} is the distance between the $(hkl) = (100)$ planes in the crystal, which are colored red. Figure from [7]

and \mathbf{c}^* . These vectors are related to the real vectors by

$$\mathbf{a}^* = 2\pi \frac{\mathbf{b} \times \mathbf{c}}{\mathbf{a} \cdot \mathbf{b} \times \mathbf{c}}, \quad \mathbf{b}^* = 2\pi \frac{\mathbf{c} \times \mathbf{a}}{\mathbf{a} \cdot \mathbf{b} \times \mathbf{c}}, \quad \mathbf{c}^* = 2\pi \frac{\mathbf{a} \times \mathbf{b}}{\mathbf{a} \cdot \mathbf{b} \times \mathbf{c}}. \quad (2.1.3)$$

We define the reciprocal lattice vector $\boldsymbol{\tau}$ as

$$\boldsymbol{\tau} = h\mathbf{a}^* + k\mathbf{b}^* + l\mathbf{c}^* \quad (2.1.4)$$

where the indices hkl , known as the *Miller indices*, are integers. The distance d_{hkl} between real space lattice planes and the reciprocal lattice vector is

$$d_{hkl} = \frac{2\pi}{|\boldsymbol{\tau}|} \quad (2.1.5)$$

as seen in figure 2.2.

The reciprocal unit cell is known as the (first) Brillouin zone [4]. A Brillouin zone is constructed by bisecting a reciprocal lattice vector and then extending the line perpendicular to the reciprocal lattice vector from the bisection point. A

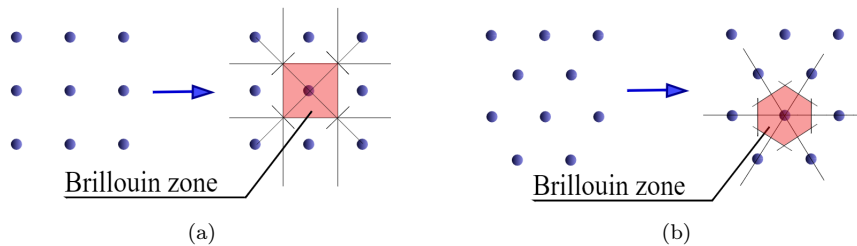


Figure 2.3: Two examples of the real lattice structure and reciprocal lattice structures the square 2 dimensional lattice a) and the hexagonal 2D lattice b). The first Brillouin zones are shown in pink. Any \mathbf{k} -vector outside the first Brillouin zone is equal to one inside. Figure from [8]

Brillouin zone is then the space that these lines envelop, see figure 2.3. Brillouin zones are interesting, because they contain all information about the crystal dynamics, since any \mathbf{k} -vector outside the first Brillouin zone is equal to one inside the zone. If a crystal contains magnetic ions on some of the lattice sites, a magnetic structure will be present. This is in many ways analogous to the physical structure, and a magnetic ordering vector, \mathbf{Q} , can be defined, which is analogous to $\boldsymbol{\tau}$ from the physical lattice. The length of the magnetic ordering vector is given by

$$|\mathbf{Q}| = \frac{2\pi}{L} \quad (2.1.6)$$

where L is the distance between periodic sites on the lattice. For a ferromagnetic lattice, where the spin on each site points in the same direction, the distance L will be between two neighbouring sites and then $\mathbf{Q} = 0$. For the antiferromagnetic lattice L will be the distance between two next nearest neighbours, as the AFM lattice repeats itself on every other lattice point. This puts \mathbf{Q} on the Brillouin zone edge. For more complicated lattices, where nearest neighbour interactions alone cannot account for the structure, then \mathbf{Q} will have some value and not reside on the Brillouin zone edge. e.g. the helicoidal structure [9]. Examples of these structures are shown in figure 2.4 and their individual \mathbf{Q} 's are shown in figure 2.5.

2.2 Magnetism

In our macroscopic world, only few systems show magnetic properties of which the most well known today is probably refrigerator magnets. It is easy to observe the magnetic properties of these materials because it is clearly evident that they attract or repel other magnetic materials. However the story of magnetism is much richer and are intrinsic to a multitude of other phenomena whose origin is more subtly magnetic than the magnetism observed in e.g. refrigerator magnets or compass needles.

This section introduces magnetism and largely follows Blundell [11].

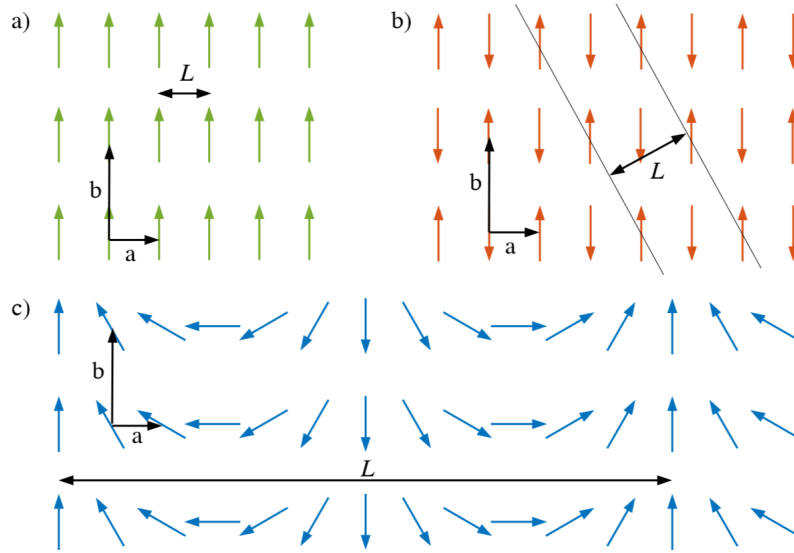


Figure 2.4: Examples of various magnetic lattice structures and the distance L between periods in said structure. In a) we see the ferromagnetic lattice, where all spins point in the same direction. b) Shows the antiferromagnetic lattice, where every spin is surrounded by spins pointing in the opposite direction. Finally in c) the helicoidal magnetic structure is shown, where the spins gradually are angled compared to its neighbours. Figure from [10]

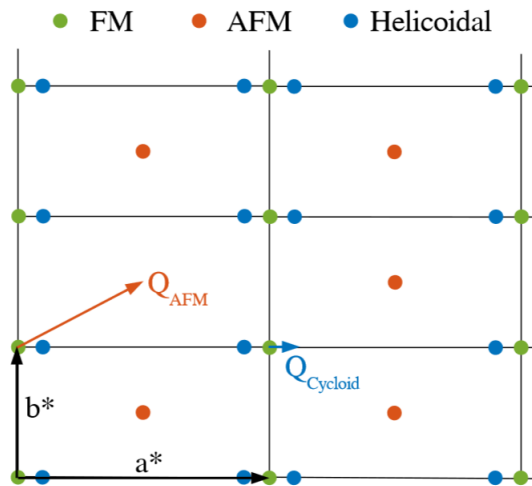


Figure 2.5: The various structures shown in figure 2.4 in reciprocal space and their associated magnetic ordering vectors \mathbf{Q} . Figure from [10]

2.2.1 Magnetic moments

Magnetism in materials is due to magnetic moments already present or generated within the material. An example of the former could be unpaired electrons. Electrons are charged particles and when they orbit the nucleus of an atom, they form a closed loop in which the charge moves around the nucleus. From Maxwell we know that any current gives rise to a magnetic moment, and as such the revolution of unpaired electrons about the nucleus generate an orbital magnetic moment

$$\boldsymbol{\mu}_l = \mu_B \mathbf{l} \quad (2.2.1)$$

where μ_B is the Bohr magneton and \mathbf{l} is the angular momentum of an electron.

In addition to the orbital angular moment of the electrons, they also possess an intrinsic angular moment called spin, denoted \mathbf{s}

$$\boldsymbol{\mu}_s = g\mu_B \mathbf{s} \quad (2.2.2)$$

here g is the gyromagnetic ratio, which takes the value of 2.0023 [11]. The spin of a particle is given by its spin quantum number s , which in the case of electrons are $s = \frac{1}{2}$ because they are in the family of half-integer spin particles called fermions. Hence in any particular direction the angular momentum of the spin of an electron must be $\hbar s^z = \pm \frac{1}{2}\hbar$. The total orbital \mathbf{L} and spin \mathbf{S} angular momentum of an atom is found by summing the individual momentums

$$\mathbf{L} = \sum_i \mathbf{l}_i \quad \mathbf{S} = \sum_i \mathbf{s}_i. \quad (2.2.3)$$

The total angular momentum of an atom, \mathbf{J} , is the sum of the orbital angular momentum and the spin angular momentum

$$\mathbf{J} = \mathbf{L} + \mathbf{S} \quad (2.2.4)$$

these contribute to the magnetic moment of the atom.

One notices immediately that for filled atomic shells, all possible positive and negative values of \mathbf{l}_i and \mathbf{s}_i will be present, and that these will cancel one another, as such there will be no net angular momentum since $\mathbf{S} = \mathbf{L} = \mathbf{J} = 0$. So we only see magnetism in atoms with unfilled shells. To determine the ground state of an atom, one can use Hund's rules [11]:

1. Hund's first rule is to maximize S . Because of the Pauli exclusion principle, which prevents particles from being in the same state, maximizing S , which is the same as having all spins parallel, the electrons will need to separate as much as possible. This minimizes the Coulomb repulsion and therefore the energy.
2. Next you maximize L . L of the same sign orbits in the same direction, and therefore you again reduce the Coulomb repulsion, by ensuring that as few as possible electrons need to cross paths.
3. Finally for less than half filled shells you need to minimize J , while for more than half filled shells J needs to be maximized. This is done in order to minimize the energy in the spin-orbit coupling.

These rules however, are not really rules and in certain cases they will not find the correct ground state. For an example Quenching may occur because the ions in a material cannot be considered free due to the fact that they interact with their neighbours through electrostatic forces. Often this will lead to a breaking of rotational symmetry of the atomic orbitals and so \mathbf{L} is no longer a good quantum number and the average contribution from \mathbf{L} will tend to 0. In this case $\mathbf{J} = \mathbf{S}$. This is seen mostly in the 3d-metals, named such because of their partially filled 3d-shells. This is exactly the case for h -YMnO₃, see section 3.7 for a general introduction to the properties of h -YMnO₃.

A generic magnetic moment from any source is

$$\boldsymbol{\mu} = \mu_B g_J \mathbf{J} \quad (2.2.5)$$

where μ_B is called the Bohr magneton and g_J is the Landé g -value, see Blundell appendix C for an introduction [11]. The magnetization of a material, \mathbf{M} is then defined as $\mathbf{M} = \sum_i \boldsymbol{\mu}_i$. Another relevant property is the magnetic susceptibility of the material χ . The susceptibility determines how severely the magnetic moments in the material responds to an applied external magnetic field \mathbf{H} . As such the magnetization can also be defined in relation to the susceptibility and the strength of the applied field as $\mathbf{M} = \chi \mathbf{H}$ for small fields.

A negative susceptibility leads to diamagnetism, the applied field generates magnetic moments in the material which aligns anti parallel to the applied field and thus opposing it. Diamagnetism appears in all materials due to the influence of the magnetic field on the electron orbitals, though the effect is usually fairly weak. On the other hand a positive susceptibility leads to paramagnetism. Paramagnetism is dependent on magnetic moments already being present within the material, e.g. atoms should have unfilled electronic orbitals, which creates a magnetic moment. Without the application of a magnetic field these moments will point in random directions, though as you apply a field, these moments will align along the direction and parallel to the applied field.

2.2.2 The Heisenberg model

When considering magnetism, interactions between the magnetic moments within the crystal becomes highly relevant, and is the cause of several interesting phenomena and properties of the crystal.

The relevant interaction is the so called exchange interaction, which leads to the existence of exchange symmetry, so that the system is unchanged if you exchange two particles. The fact that electrons are fermions requires their wave function must be antisymmetric overall. If we consider just two electrons in states $\psi_a(\mathbf{r}_1)$ and $\psi_b(\mathbf{r}_2)$ at the positions of \mathbf{r}_1 and \mathbf{r}_2 respectively, then we can create an overall antisymmetric singlet state Ψ_S from a symmetric singlet spatial state $\psi_{space,S}$ and an antisymmetric Triplet spin state χ_T , as well as an overall antisymmetric triplet state Ψ_T from an antisymmetric spatial singlet state $\psi_{space,T}$ and a symmetric triplet spin state χ_S . If \uparrow denotes spin-up and \downarrow denotes spin down, then the antisymmetric spin state of a 2-electron system is

$$\chi_S = \frac{|\uparrow\downarrow\rangle - |\downarrow\uparrow\rangle}{\sqrt{2}} \quad (2.2.6)$$

while the symmetric ones are

$$\chi_T = |\uparrow\uparrow\rangle, \text{ or } \chi_T = \frac{|\uparrow\downarrow\rangle + |\downarrow\uparrow\rangle}{\sqrt{2}}, \text{ or } \chi_T = |\downarrow\downarrow\rangle \quad (2.2.7)$$

The spatial part of the wave function is then given by

$$\psi_{space,S} = \frac{\psi_a(\mathbf{r}_1)\psi_b(\mathbf{r}_2) + \psi_a(\mathbf{r}_2)\psi_b(\mathbf{r}_1)}{\sqrt{2}} \quad (2.2.8)$$

$$\psi_{space,T} = \frac{\psi_a(\mathbf{r}_1)\psi_b(\mathbf{r}_2) - \psi_a(\mathbf{r}_2)\psi_b(\mathbf{r}_1)}{\sqrt{2}} \quad (2.2.9)$$

The combined spatial and spin wave functions of the singlet and triplet states are then

$$\Psi_S = \psi_{space,S}\chi_T \quad (2.2.10)$$

$$\Psi_T = \psi_{space,T}\chi_S \quad (2.2.11)$$

with the corresponding energies

$$E_S = \int \Psi_S^* \mathcal{H} \Psi_S d\mathbf{r}_1 d\mathbf{r}_2 \quad (2.2.12)$$

$$E_T = \int \Psi_T^* \mathcal{H} \Psi_T d\mathbf{r}_1 d\mathbf{r}_2 \quad (2.2.13)$$

if the wave functions are normalized then the difference in energy is

$$E_S - E_T = 2 \int \psi_a^*(\mathbf{r}_1)\psi_b^*(\mathbf{r}_2)\mathcal{H}\psi_a(\mathbf{r}_2)\psi_b(\mathbf{r}_1)d\mathbf{r}_1 d\mathbf{r}_2 = 2J \quad (2.2.14)$$

where the exchange constant J has been defined as

$$J = \frac{E_S - E_T}{2}. \quad (2.2.15)$$

We want an effective Hamiltonian for the system, and in order to get that we use that the product of two spins \mathbf{S}_1 and \mathbf{S}_2 is

$$\mathbf{S}_1 \cdot \mathbf{S}_2 = \begin{cases} -\frac{3}{4} & \text{for singlets} \\ \frac{1}{4} & \text{for triplets} \end{cases}$$

Using this to parametrize the difference between singlet and triplet states we achieve an effective Hamiltonian given by:

$$\mathcal{H} = \frac{1}{4}(E_S + 3E_T) - (E_S - E_T)\mathbf{S}_1 \cdot \mathbf{S}_2 \quad (2.2.16)$$

If we only consider the spin part of the Hamiltonian we get

$$\mathcal{H}_{\text{spin}} = -2J\mathbf{S}_1 \cdot \mathbf{S}_2 \quad (2.2.17)$$

If we then assume that similar interactions, as the two-electron interaction derived above, is present between all neighbouring atoms in a lattice, then we arrive at the Heisenberg Hamiltonian

$$\mathcal{H}_{\text{Heisenberg}} = - \sum_{ij} J_{ij} \mathbf{S}_i \cdot \mathbf{S}_j \quad (2.2.18)$$

Where J_{ij} is the exchange constant between the i 'th and j 'th spin. The factor of 2 disappears due to the fact that you double count each pair in the double sum. The method of exchange can vary substantially from system to system. The most simple is just a direct exchange between two neighbouring sites as introduced above. Another, more common, is the indirect exchange, where an intermediate, non-magnetic, site is used in the interaction. Using an intermediate non-magnetic site can be a kinetic energy advantage for antiferromagnets because the electrons can become delocalized over the whole structure and as such reduce their kinetic energy. Several other methods of exchange interactions exists, but will not be discussed in this thesis.

2.2.3 Other models

A number of other models exist that describe magnetism. Which model you need depend on the dimensionality of the system, d , and the symmetry of the order parameter D . A short review of some of these are given here. The first model is the Ising model ($D = 1$) with the Hamiltonian H given by

$$H = - \sum_n \sum_i J_i S_n^z S_{n+i}^z \quad (2.2.19)$$

Where S_n^z is the z component of the spin on site n , J_i is the exchange interaction between site n and site i , for nearest neighbour $i = 1$. The order parameter for the ferromagnetic case ($J > 0$) is $\sum_n S_n^z$ is one dimensional.

The X-Y model ($D = 2$):

$$H = - \sum_n \sum_i J_i (S_n^x S_{n+i}^x + S_n^y S_{n+i}^y) \quad (2.2.20)$$

The order parameter is the vector sum of the two spin components in the x and y direction, which is two dimensional.

The Heisenberg model ($D = 3$):

$$H = - \sum_{ni} J_i (S_n^x S_{n+i}^x + S_n^y S_{n+i}^y + S_n^z S_{n+i}^z) \quad (2.2.21)$$

Where the spin is a three-dimensional vector. Finally there is the spherical model for $D = \infty$. Which is solvable, but so far does not correspond to any actual system.

2.2.4 Magnetic structures

Below a certain critical temperature T_c , the thermal energy of the system becomes so low that the dominant energy concern is the alignment of the magnetic spins within the sample. Above T_c the spins behaves either as diamagnets or paramagnets, and are oriented randomly throughout the sample. At T_c the rotational symmetry of the system is broken and all the spins orientates themselves according to their environments. The orientation of the spins within a crystal creates the magnetic structure. Depending on the sign of the exchange constant J the spins will prefer to align in the same direction as their neighbours or in the opposite direction of them. This effect gives rise to the two most simple

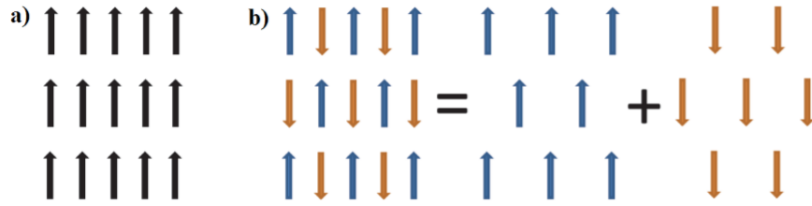


Figure 2.6: Depending on the sign of the exchange constant J then a square lattice of spins will align either a) parallel or b) antiparallel. The case in a) is called ferromagnetism while the case in b) is called antiferromagnetism. The antiferromagnetic lattice can also be seen as a superlattice of two ferromagnetic sublattices each in opposite direction. From [7]

large scale magnetic structures which can be found in crystals, namely ferromagnetism and antiferromagnetism. In addition to the breaking of rotational symmetry, time-reversal symmetry is also broken because if you flip the direction of time, the orbital angular momentum as well as the spin angular momentum will turn in the opposite direction, as such effectively flipping the sign of the magnetic moment.

In a ferromagnet, $J > 0$, at the critical temperature, which for ferromagnets is called the Curie-temperature T_c , the spins all align in the same direction. This happens because the electrons in the crystals attempt to minimize their energy. Looking at the Heisenberg Hamiltonian eq. 2.2.18 if $J > 0$ then the product of the spins $\mathbf{S}_i \cdot \mathbf{S}_j$ should be positive as well because the minus sign at the front ensures that the energy is then lowered. The product is positive only if the spins have the same sign, and as such it is energetically preferable for the spins to align in the same direction.

In a very similar way antiferromagnetism, $J < 0$, where all spins prefer to be aligned anti parallel to their neighbours at the critical temperature now called the Néel-temperature T_N . This is due to a negative exchange constant, if $J < 0$ then the spin product should be negative in order for energy to be lowered. These two structures can be seen in figure 2.6.

If we allow for more complex types of lattices beside the square one, the sign of the coupling constant can lead to some very interesting phenomena. If we look at a triangular lattice, which arises as part of one of the most commonly found lattices in nature, namely the hexagonal lattice structure, then if $J < 0$ such that the spins want to align antiferromagnetically, only two of the spins can fulfill the requirement of pointing in opposite directions, while this task is impossible for the last one. The last spin is called frustrated and the structure is called geometrically frustrated, see figure 2.7, because the system cannot order into a specific groundstate. Geometrically frustrated systems lead to extremely degenerate ground states, where large numbers of spins in the lattice cannot align and so there is a myriad of ways you can arrange the spins which all share the same lowest possible energy. The material which is the focus of this thesis, h-YMnO₃ is geometrically frustrated, see section 3.7. The frustration index, f ,

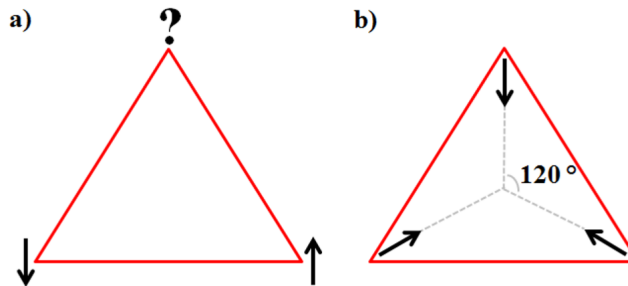


Figure 2.7: When spins align antiferromagnetically, they want to point in opposite directions. On a triangular lattice with a spin at each corner a), this leads to geometrical frustration where two of the three spins align in opposite directions, while the 3rd spin cannot align anti parallel to both of them. Therefore the last spin will be able to fluctuate. From a classical point of view b) the spins would simply minimize their energy by pointing towards the middle of the triangle, each with an angle of 120° between them. From [7]

is defined for an antiferromagnet as

$$f = \frac{|\theta_{CW}|}{T_N} \quad (2.2.22)$$

where θ_{CW} is the Curie-Weiss temperature and T_N is the Néel temperature. The frustration index tells you how frustrated the system is and in general systems with $f > 5 - 10$ indicates a strong suppression of ordering due to frustration [12].

2.3 Excitations in Crystals

According to Goldstones-theorem, excitations can occur in all systems with a broken continuous symmetry. These excitations are quantized and known as Goldstone-bosons [13]. The Heisenberg model is one model with such a continuous symmetry. The ordering of atoms into a crystal lattice breaks the rotational symmetry, and as such excitations will be possible. The structural excitation of a crystal lattice is vibrational modes, which are quantized and known as phonons the energy cost of creating a phonon tends to 0 as \mathbf{q} tends to 0. In a somewhat similar fashion the magnetic structure can be excited, such that the spins of the magnetic sites precess, this then causes the nearby spins to precess as well, making a spin wave propagating through the magnetic sites, this is quantized as magnons.

2.3.1 Phonons

Phonons are elementary excitations of the crystal lattice. The energy of these excitations are quantized and the associated quasi particle is called a phonon. In our three dimensional world each atom has three degrees of freedom, one along each of the euclidean axis (x, y, z) . This gives three vibrational modes,

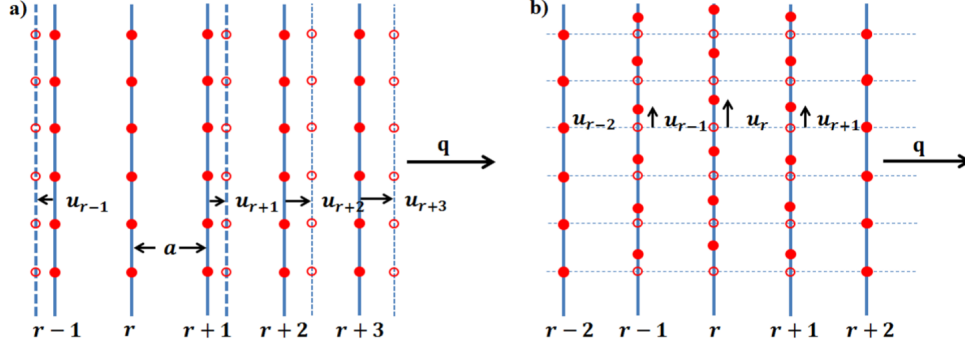


Figure 2.8: The two types of phonon excitations. In **a)** the vibration is longitudinal as it is along the direction of \mathbf{q} , while in **b)** the vibration is perpendicular to \mathbf{q} and is therefore a transverse mode. From [7]

two of which are transverse - vibrations perpendicular to the direction the wave is propagating \mathbf{q} , See figure 2.8 b), and one which is longitudinal - along the direction of propagation \mathbf{q} , See figure 2.8 a).

In a crystal lattice with N unit cells and p atoms in each unit cell there is a total of pN atoms in the crystal. Each of these have three degrees of freedom, so the total number of degrees of freedom for the crystal must be $3pN$. Because you can have N \mathbf{q} -values inside a Brillouin zone you get $3N$ acoustic phonons. Acoustic phonons correspond to coherent movements of the crystal lattice out of their equilibrium positions, see figure 2.9 a) bottom. The remaining $(3p - 3)N$ degrees of freedom become optical phonons. Optical phonons can only occur if there are two or more atoms in the unit cell, they are out of phase vibrations where e.g. one type of atom moves to the right while the other type moves to the left, see figure 2.9 a) top. The energy of the vibrations of a chain of single atoms or ions can be described by the following Hamiltonian

$$H = \sum_{i=1}^N \frac{\mathbf{p}_i^2}{2m} + \frac{1}{2}m\omega_0 \sum_i (\mathbf{x}_i - \mathbf{x}_{i+1}) \quad (2.3.1)$$

where \mathbf{p} and \mathbf{x} are the momentum and position operators, m is the mass of the atom or ion, and ω_0 is the characteristic frequency of the oscillation, defined as $\omega_0 = \sqrt{K/M}$. The first term is the kinetic energy while the 2nd term is the potential energy of a harmonic oscillator. This gives the dispersion relation for the one-dimensional chain of single atoms

$$\omega^2(q) = 2\omega_0^2 (1 - \cos(qa)) = 4\omega_0^2 \sin^2\left(\frac{qa}{2}\right) \quad (2.3.2)$$

where a is the distance between two sites in the lattice [9]. For a diatomic chain the dispersion relation is given by [4]

$$\omega_{\pm}^2(q) = K \left(\frac{1}{m_1} + \frac{1}{m_2} \right) \pm K \sqrt{\left(\frac{1}{m_1} + \frac{1}{m_2} \right)^2 - \frac{4\omega_0^2 \sin^2\left(\frac{qa}{2}\right)}{m_1 m_2}}. \quad (2.3.3)$$

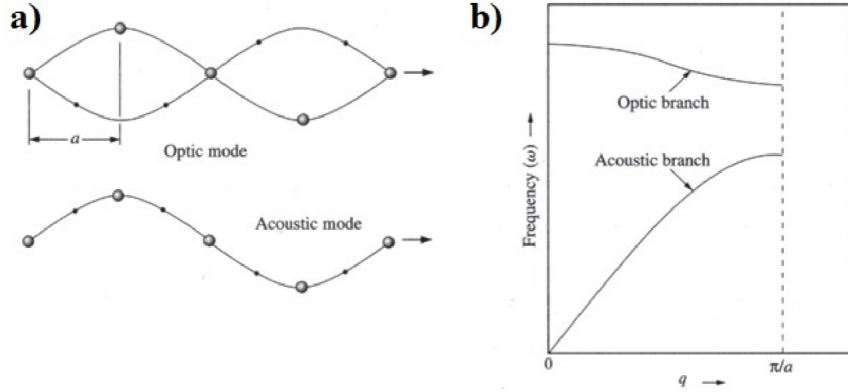


Figure 2.9: **a)** top: Acoustical phonons where the movement of the atoms are in phase. **a)** bottom: Optical phonons characterized by an out of phase movement of the atoms in the unit cell. **b)** dispersion relations of the acoustical and optical phonons branch of a diatomic chain of atoms. Figure from [14]

In the long wavelength limit, which is for small qa , the dispersion relation of the acoustic phonon branch becomes

$$\omega_-^2 \approx \frac{K}{2(m_1 + m_2)} q^2 a^2 \quad (2.3.4)$$

while the dispersion relation of the optical phonon is

$$\omega_+^2 \approx 2K \left(\frac{1}{m_1} + \frac{1}{m_2} \right). \quad (2.3.5)$$

As can be seen in figure 2.9 b) the acoustic phonon branch is 0 at the zone center, for small q it increases linearly. For small q the optical phonon branch is non-zero at the zone center, and approximately does not depend on q in the long wavelength limit. One can see that the energy required to create an acoustic phonon is approaching zero, and therefore acoustic phonons are present even at extremely low temperatures, while for the optical phonons there is an energy requirement to create them. Phonons are bosons, and as such the number of phonons n_j with frequency ω_j at a given temperature T is given by the Bose factor [14].

$$n_j(q) = \frac{1}{\exp(\hbar\omega_j/k_B T) - 1}. \quad (2.3.6)$$

2.3.2 Magnons

Spin waves are caused by the exchange interaction by spins close to each other. If one spin begins to precess or flip, this will affect the nearest spins, which will react accordingly and thus a wave of precession or flips will propagate through a lattice of magnetic spin sites. Like lattice vibrations, which are quantized as phonons, the energy of spin waves are also quantized and called magnons. A ferromagnetic spin-wave of precessing spins are shown in figure 2.10.

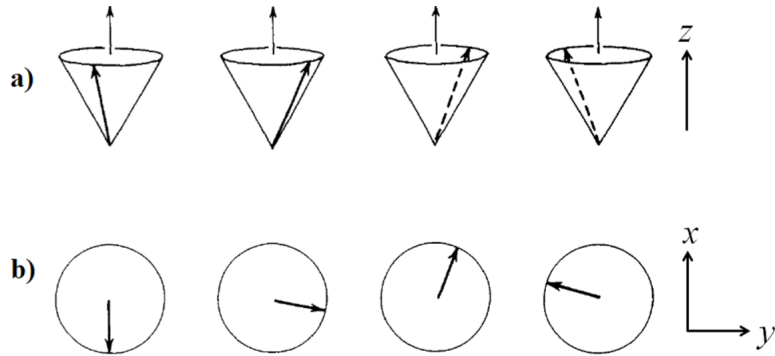


Figure 2.10: A ferromagnetic spin-wave precession about the z -axis. a) is the view from the xy -plane, while b) is the view looking down from the z -axis. Figure from [15]

For a linear chain of magnetic sites coupled by a ferromagnetic exchange coupling J , the dispersion relation is given by

$$\hbar\omega = 4JS(1 - \cos(qa)) \quad (2.3.7)$$

where $\hbar\omega$ is the wave energy, S is the magnitude of the spin, a is the distance between two adjacent atoms and q is the magnitude of the wave-vector [16]. At small q the dispersion is $\hbar\omega \propto q^2$. For a chain of antiferromagnetically coupled sites the dispersion relation is instead

$$\hbar\omega = 4|JS|\sin(qa) \quad (2.3.8)$$

which for small q becomes $\hbar\omega \propto q$. A dispersion relation for a ferromagnetic chain can be seen in figure 2.11 a) and for an antiferromagnetic chain in b). Both the ferromagnetic spin chain and the antiferromagnetic chain goes to 0 at $q = 0$. In reality this is rarely the case due to next-nearest neighbour interactions and beyond within the crystal, which introduces an energy gap. The general approach to determining the dispersion relation for a real system is described in [16], and is given by

$$\hbar\omega = 2S(J(0) - J(\mathbf{q})) \quad (2.3.9)$$

where $J(\mathbf{q})$ is the fourier transform of the spin-spin coupling

$$J(\mathbf{q}) = \sum_{\delta} J_{\delta} e^{i\mathbf{q} \cdot \mathbf{r}_{\delta}}. \quad (2.3.10)$$

2.4 Multiferroics

Ferroics are materials that, below some critical temperature T_c , exhibit a spontaneous breaking of some symmetry and thereby also undergoes a phase transition. This new phase is one of three possible ferroic states. The first one is the already covered (anti)ferromagnetic state, where a spontaneous breaking of

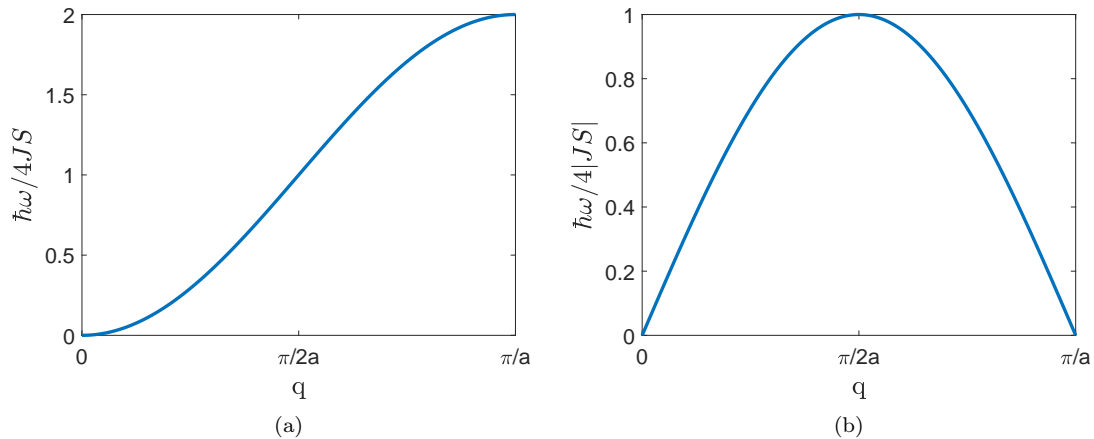


Figure 2.11: *Dispersion relations for magnons. (a) a chain of ferromagnetically coupled spins. (b) a chain of antiferromagnetically coupled spins.*

time-reversal and rotational symmetry gives rise to a spontaneous magnetization \mathbf{M} with an associated magnetic field \mathbf{H} . In addition there is the ferroelectric state which is a breaking of the spatial symmetry, such that a spontaneous polarization \mathbf{P} , the polarization will then create an electric field \mathbf{E} . Finally there is the ferroelastic phase, where a phase transition from one point group symmetry to another spontaneously occurs. This creates strain $\boldsymbol{\sigma}$ and induces a stress $\boldsymbol{\epsilon}$ on the crystal. See figure 2.12.

Common to all the types of ferroics is that they make hysteresis loops in their magnetization, polarization, and strain depending on whether they are (anti)ferromagnetic, ferroelectric, or ferroelastic. e.g. the first polarization hysteresis loop measured for a ferroelectric material was for the compound $\text{KNaC}_4\text{H}_4\text{O}_6 \cdot \text{H}_2\text{O}$, also known as Rochelle salt, in 1921 [18].

Multiferroics are materials that exhibit at least two, possibly all three, of the ferroic properties: (anti)ferromagnetism, ferroelectricity, or ferroelasticity. If the ordering parameters of the ferroic properties are coupled, it is possible to induce, for an example, a magnetization using an electric field because the polarization that is directly created by the electric field, will couple to the magnetization and thereby create both, see figure 2.13. These couplings have a wide range of possible uses in science and technology, and is therefore one of the primary reasons to study multiferroics in depth.

Multiferroics are however rare, because ferroelectricity and (anti)ferromagnetism are mutually exclusive in most cases [20]. Only a few materials allow the spatial and time-reversal symmetries to be broken simultaneously. Of the 230 possible crystallographic space groups, only 13 allow for simultaneous polarization and magnetization [21]. A further restriction is that many materials that crystallizes to one of the allowed 13 groups are not multiferroics for other reasons. Most ferroelectric systems contain a non-magnetic transition metal ion, therefore lacking the unpaired spin required for the system to order (anti)ferromagnetically. In


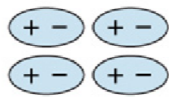
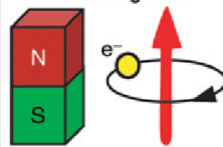
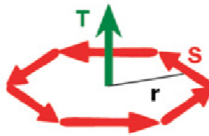
Time \ Space	Invariant	Change
Invariant	Ferroelastic 	Ferroelectric 
Change	Ferromagnetic 	Ferrotoroidic 

Figure 2.12: Ferroelastics are space and time invariant. Ferroelectrics break spatial symmetry, while maintaining its time symmetry. Ferromagnetics break time-reversal symmetry, but maintains its spatial symmetry. Finally ferrotoroidics break both spatial and time symmetry. Figure from [17]

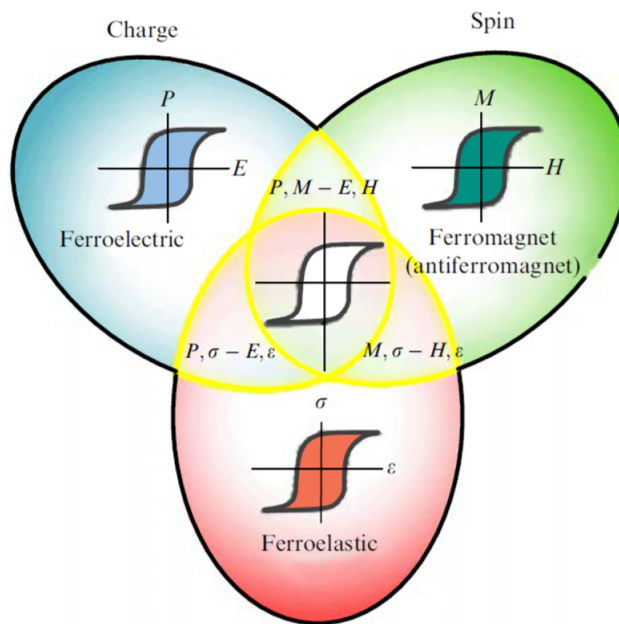


Figure 2.13: The possible couplings in multiferroics. A multiferroic is a material that exhibits several of the ferroic properties simultaneously. The coupling between the order parameters of the different ferroic states allows one to induce magnetism with an electric field, if the magnetization and polarization is coupled. Figure from [19]

addition most materials that contain magnetic ions are metallic, and therefore not insulators, which makes ferroelectricity an impossibility [20]. With all these constraints multiferroic materials are indeed a rare occurrence.

Multiferroics are generally divided into two categories, type-I and type-II. In type-I multiferroics the ferroelectric transition temperature T_c is higher than the (anti)ferromagnetic transition temperature T_N . While in type-II the transition temperature is equal or reversed such that $T_c \leq T_N$ [22].

One particular category of materials that are multiferroics are the rare earth manganites. The rare earth manganites have been the subject of considerable study in the scientific community. They show phenomena and dynamics that have great interest from a fundamental physics standpoint, but also has many properties which is sought after by the industry. The family of rare earth manganites RMnO_3 , where R simply refers to one of the rare earth metal ions defined by the IUPAC as the lanthanides (La, Ce, Pr, Nd, Pm, Sm, Eu, Gd, Tb, Dy, Ho, Er, Tm, Yb, Lu) with the addition of the transition metals (Y and Sc) [23]. All of the rare earth manganites are multiferroics, but whether they are type-I or type-II depends entirely on their structure. All the rare earth manganites can form stable hexagonal crystal structures, when they do so they are always type-I multiferroics. The lighter rare earth elements (La-Ho) as well as Y and Sc however, can also be made as an orthorhombic distorted perovskite structure in which case they will be type-II multiferroics [24].

2.5 Critical Phase Transitions

The entirety of section 2.5 largely follows the book by Collins [13].

As material changes from one phase to another, e.g. liquid to solid, we say that the material has made a phase transition. Phase transitions come in two variants. Historically known as 1st order and 2nd order phase transitions due to the fact that first order phase transitions have a discontinuity in the first differential of the free energy of the system involved, while similarly 2nd order phase transitions were expected to have a discontinuity in the 2nd differential of the free energy. However 2nd order phase transitions were later renamed as critical phase transitions because it became clear that the free energy does not behave analytically at the point of the phase transition, which for critical phase transitions are known as a critical point. Critical phase transitions are also sometimes called continuous phase transitions.

A critical point is a point in parameter space where the difference between two different phases become extinct. This happens between the gas and liquid phase of water at high pressure and high temperature, $P_c = 22.064\text{MPa}$ and $T_c = 647.096\text{K}$ respectively, see Figure 2.14. Above these values the gas and liquid phase become indistinguishable, and as such you can move from one phase to the other without ever crossing a phase transition. E.g. if you start in the gas phase at $T > T_c$ and $P < P_c$, then increase the pressure such that it goes above the critical pressure, then you lower the temperature below T_c and finally you reduce the pressure again below P_c . You will then have moved from the gas phase to the liquid phase, without ever crossing a phase transition.

While the critical point of water is situated at some rather arbitrary and, you could argue, not very interesting values of pressure and temperature, other

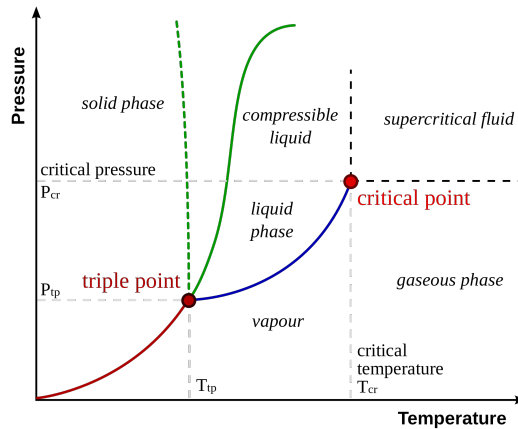


Figure 2.14: The phase diagram of water. At the critical point, which is situated at the critical temperature of $T_c = 647.096K$ and a critical pressure of $P_c = 22.064MPa$ the phase transition through the critical point becomes a 2nd order phase transition, or a critical phase transition. You can circumvent the phase transition completely by going around the critical point. This is however not possible for magnetism where the critical point is at $0T$, which is impossible to circumvent due to negative magnetic fields being unphysical.

systems have critical points much closer to values that you would normally encounter. Most notably the phase transition between the ferro- or antiferromagnetic state and the paramagnetic state has a critical point at $0T$ external magnetic field. The external field that we are influenced by on the surface of the earth is very low, between $25 \mu T$ and $65 \mu T$, as such normal experimental conditions approach this critical point and therefore it is of great interest experimentally.

Another crucial difference between first order and critical phase transitions is that there is a latent heat involved in the first order transition, thus it requires energy to change the system from one phase to the other, for a critical phase transition this is not so. Alternatively a critical phase transition exhibits some rather remarkable features close to the critical point such as a power law decay of the correlation length, which is assumed to reach infinity at the actual critical point.

Critical phase transitions are always characterized by the fact that experiments show critical scattering near the phase transition. The origin of this critical scattering is the fact that as you approach the critical temperature from either side, micro regions of the opposite phase appear, these are short lived, but nevertheless contribute to the coherent scattering of the sample. These microregions grow in size the closer to the critical point you get and at the critical temperature these micro regions are of the same size as the ordinary regions, above the critical temperature, the micro regions become larger than the ordinary regions until what we previously called the micro regions take up all space, and the system is effectively in a new state. This is illustrated in figure 2.15.

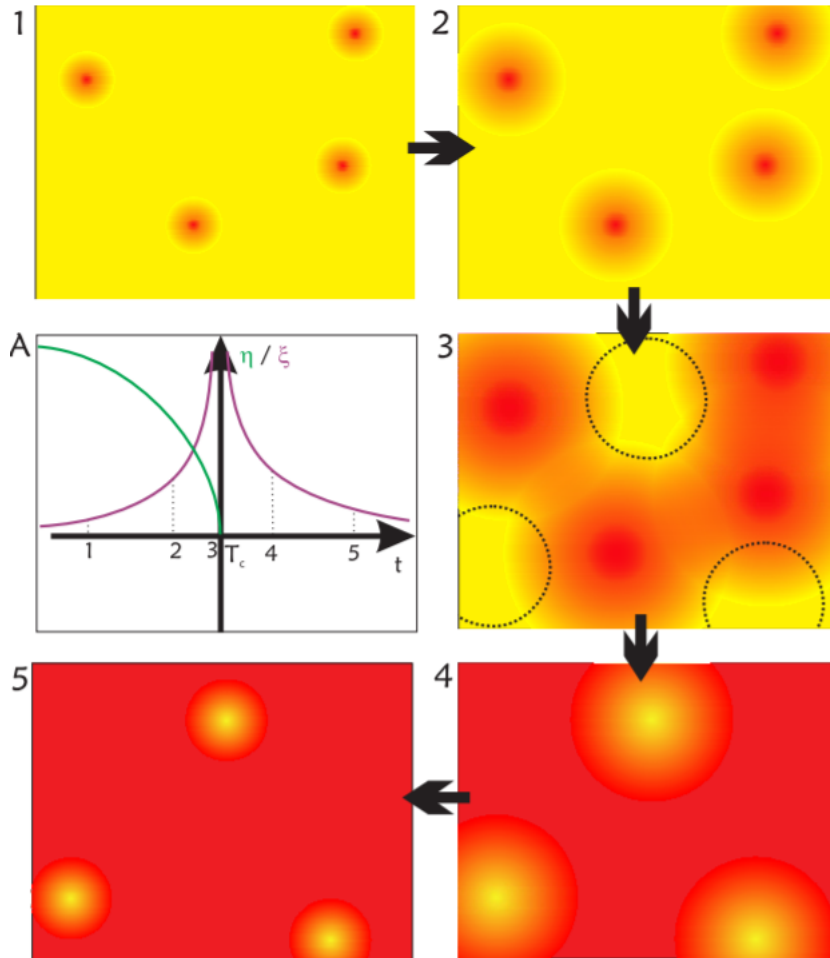


Figure 2.15: Figure (A) shows the evolution of the order parameter (green) and the correlation length (purple) as the critical temperature of the phase transition is approached. Figures (1) through (5) show the growth of the disordered phase (red) within the ordered phase (yellow). As the critical temperature is approached these micro regions of the disordered state will start to appear and grow larger the higher the temperature gets. At the phase transition (3) the size of the regions of the disordered state is just as large as that of the ordered one. Above the critical temperature the regions of the disordered state dominate until the regions of ordered state disappear completely as the temperature increases even further. Figure from [25].

Critical phase transitions can be described as a global symmetry which breaks at the critical temperature T_c . For example the orientation of the spins of a paramagnet is randomized in all possible directions, when you cool the paramagnet below T_c all the spins align in some direction and a general magnetization of the material takes place, therefore the magnetization of the system now depends on the rotation of the sample which means that the rotational symmetry that was present above T_c has been broken below. The magnetization of the material can therefore be used as an indicator of whether we are below or above T_c , as such we can call the magnetization an *order parameter* because it tells us whether the system is ordered or not. A general order parameter η have the following properties: For temperatures T above the critical temperature of the phase transition T_c the order parameter is 0, while below it is different from 0, or put more simply

$$\eta = 0, \quad T > T_c \quad (2.5.1)$$

$$\eta \neq 0, \quad T < T_c \quad (2.5.2)$$

Each global symmetry has an order parameter related to it, for the spin orientation it is the magnetization M , which will be our main interest in this work. Other examples could be the polarization \mathbf{P} as well as the strain ϵ .

Near the critical point there will be fluctuations between the two phases in small micro regions throughout the crystal. The correlation length ξ , which corresponds to the linear extend of these regions approaches infinity at the critical point. The response time of the system also tends to infinity as the critical point is approached from any direction. This is known as critically slowing down [13].

Several methods have been introduced over the years to describe critical phase transitions, some of those will be shown below.

2.5.1 Landau theory

Landau theory or sometimes known as mean field theory is the simplest approach to handle critical phase transitions. The basic assumption of Landau theory is that the properties of the system can be described by a Taylor expansion of the free energy $F(T, \eta)$ of the system. For the magnetic case the free energy is the Helmholtz free energy $F(T, M)$. Since the free energy of the magnetization is the same for positive and negative values of M the odd terms in the Taylor expansion will be 0 and we are left with:

$$F(T, M) = F_0(T) + a(T)M^2 + b(T)M^4 + \dots \quad (2.5.3)$$

If the constant in front of the highest order term is positive, and enough terms need to be included until this requirement is fulfilled, then the free energy will have a minimum somewhere and the system will be in equilibrium. This criteria can also be stated as

$$\left. \frac{\partial F}{\partial M} \right|_T = 0 \quad (2.5.4)$$

$$\left. \frac{\partial^2 F}{\partial M^2} \right|_T > 0 \quad (2.5.5)$$

which yields the following equations

$$a(T)M + 2b(T)M^3 = 0 \quad (2.5.6)$$

and

$$a(T) + 6b(T)M^2 > 0 \quad (2.5.7)$$

above T_c the order parameter must be zero, $M = 0$, therefore it follows from equation 2.5.7 that

$$a(T) > 0, \quad T > T_c \quad (2.5.8)$$

Below T_c we require that $M \neq 0$, from equation 2.5.6 this gives

$$a(T) = -2b(T)M^2, \quad T < T_c \quad (2.5.9)$$

from which it is clear that the only possibility to create a minimum at a place where $M \neq 0$ is to require that $a(T) < 0$ for $T < T_c$. As such

$$b(T)M^2 > 0 \implies b(T) > 0, \quad T < T_c \quad (2.5.10)$$

now by expanding $a(T)$ around $T = T_c$ to the lowest nonzero term, we get

$$a(T) = (T - T_c)a_0 \quad (2.5.11)$$

where a_0 is a positive constant, and solve for the magnetization M below T_c :

$$a(T) = -2b(T)M^2 \quad (2.5.12)$$

$$a_0(T - T_c) = -2b(T)M^2 \quad (2.5.13)$$

$$M^2 = -\frac{a_0(T - T_c)}{2b(T)} \quad (2.5.14)$$

$$M^2 = \frac{a_0(T_c - T)}{2b(T)} \quad (2.5.15)$$

$$M = \left(\frac{a_0(T_c - T)}{2b(T)} \right)^{\frac{1}{2}} \quad (2.5.16)$$

Putting this back into equation 2.5.3 the free energy at equilibrium above and below T_c is given by

$$F(T, M) = F_0(T), \quad T > T_c \quad (2.5.17)$$

$$F(T, M) = F_0(T) - \frac{a_0^2(T_c - T)^2}{4b(T)}, \quad T < T_c \quad (2.5.18)$$

From this we can compute several thermodynamic properties like the specific heat and the thermal susceptibility, however these often give results which are vastly different from experiment. this is because the assumption that you can Taylor expand the free energy usually breaks down near a critical phase transition because the free energy, as stated previously, is a nonanalytical function at the critical point.

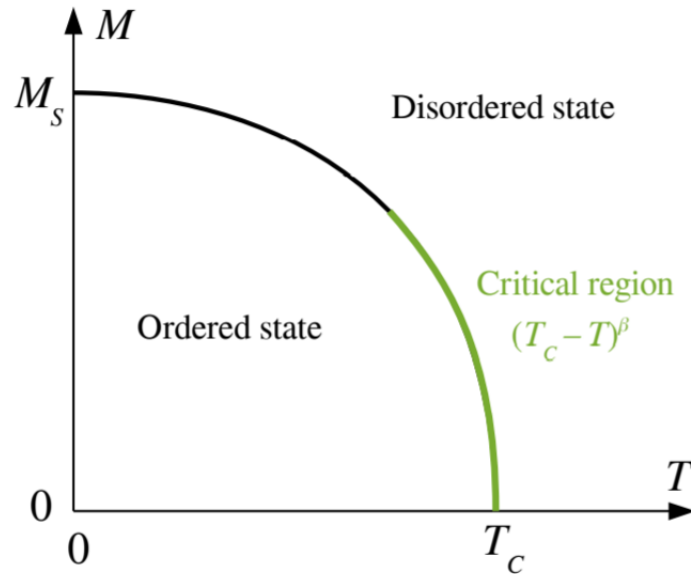


Figure 2.16: An illustration of the relationship between the magnetization and the temperature. Below the critical temperature T_C the system is in an ordered state, while this order breaks down above T_C . Close to T_C the magnetization generally follow a power law relation with temperature indicated in green on the figure. Figure from [10].

2.5.2 Critical exponents

Experimentally it has been shown that close to a critical phase transition properties like the susceptibility, specific heat, the correlation length and the magnetization all obey power laws, of which the first three diverge while the last one goes to 0 at T_c . First a reduced temperature t is defined as

$$t = \frac{T - T_c}{T_c} \quad (2.5.19)$$

such that $t = 0$ when we reach the critical temperature T_c . Then e.g. the magnetization can be described by the power law:

$$M(t) = (-t)^\beta = \left(\frac{T_c - T}{T_c} \right)^\beta. \quad (2.5.20)$$

In general plotting the magnetization versus temperature yields a plot that looks similar to figure 2.16 where the ordered state is below the critical temperature T_C while the disordered state is above it. Close to T_C the magnetization as a function of temperature will follow a power law relation. This critical region can be determined as seen in section 4.1.3 and then fitted to determine the value of the critical exponent. From equation 2.5.16 it is clear that in Landau Theory the value of β is simply $\frac{1}{2}$. Two other critical exponents will be determined in this thesis, that is the critical exponent ν related to the correlation length by

the power law

$$\xi(t) \sim t^\nu \quad (2.5.21)$$

and the critical exponent γ associated with the magnetic susceptibility χ

$$\chi(t) \sim t^{-\gamma} \quad (2.5.22)$$

Other critical exponents exist, such as α associated with the specific heat and η with the correlation function. These however will not be measured in this work, and as such will not be used further.

2.5.3 Universality

The concept of universality is that the features of phase transitions are universal, and therefore independent of the system involved.

For a continuous phase transition the static critical exponents depend only on the dimensionality of the system, d . The symmetry of the order parameter, D (which in simple cases is equivalent to the number of dimensions in which the order parameter is free to vary). Whether the forces involved are short or long range. To include the dynamical critical exponents (e.g. those originating from phonons and magnons) a fourth condition is added which is: The dynamical critical exponents also depend on the conservation law of the system.

As such you can know everything there is about a continuous phase transition of any material with parameters d , D and the same range, simply by studying it in the simplest case, which is usually magnetism.

The standard models are: Ginzburg-Landau for long range forces. And for short range forces we have the Ising Model, X-Y model, and the 3 dimensional Heisenberg model as introduced in section 2.2.3.

While these models are interesting, they are only in special cases solvable analytically. The general cases that can be solved are one dimensional ($d = 1$), but no critical phase transitions can occur in a one dimensional chain when you only consider short range order. According to Landau this is due to the fact that the energy cost of creating a domain wall in one dimension is finite, while the entropy gain of creating such a wall increases with the length of the system [26]. In four or more dimensions ($d \geq 4$), which is always solvable and always give Ginzburg-Landau solutions, however these are obviously non physical solutions. The two dimensional Ising model ($d = 2, D = 1$) and the spherical model ($D = \infty$) also have analytical solutions. And finally all cases where the interaction range is infinite which give Ginzburg-Landau solutions.

As should be apparent most physically interesting systems cannot be solved analytically, so experimental methods and to some degree numerical simulations is the way forward to understanding these systems.

2.5.4 Scaling

In order to tackle the problem of short range interactions in multidimensional systems, the scaling theory approach can be applied. The basis of scaling theory is that regions of the other phase exist in the primary phase close to the critical temperature T_c . These regions have a volume with dimensions of the order of the correlation length ξ , see equation 2.5.21, inside any given volume it is a good

approximation that the order parameter remains equal throughout the region, while only fluctuating slowly in time. If we divide a region into cells with L lattice sites on each side, then in a d -dimensional lattice this would yield L^d sites per cell. As we enter the critical region near T_c , ξ increases as we approach T_c and diverge at T_c , if L is chosen such that there is always a large number of sites, then we can always make the assumption that

$$a \ll La \ll \xi \quad (2.5.23)$$

where a is the lattice parameter. The assumption that the form of the Hamiltonian does not change as we vary the cell size, only the spin, S , and the effective field between cells H_e change. In the correlated region S and H_e should be similar for neighbouring cells while H_e should be uniform within a cell. This approach yields the so called scaling laws between the various critical exponents. The derivation of this can be found in [13], but will be omitted here.

A selection of scaling laws can be seen here. In this thesis the exponents β , γ , and ν will be measured, so scaling laws with these are of particular interest. The first scaling laws relates α to ν .

$$2 - \alpha = d\nu \quad (2.5.24)$$

where d is the spatial dimensions of the system and α is the critical exponent related to the specific heat. The three critical exponents used in this thesis relates to each other by

$$d\nu = 2\beta + \gamma \quad (2.5.25)$$

The critical exponent η is a measure of the size of the correlations at the critical temperature. It relates to γ and ν in the following way.

$$2 - \eta = \frac{\gamma}{\nu} \quad (2.5.26)$$

The critical exponent for the specific heat α can be determined from β and γ by combining equations 2.5.24 and 2.5.25 to

$$2 - \alpha = 2\beta + \gamma \quad (2.5.27)$$

Chapter 3

Methods

For this thesis several experiments were conducted on the SINQ neutron source at the Paul Scherrer Institut [27] in Switzerland, using the triple axis spectrometer RITA-II [28] and eiger [29]. Following is an introduction to the experimental technique of neutron scattering.

3.1 Properties of the Neutron

The neutron is a electrically neutral spin-1/2 particle with a magnetic moment μ_n given by [30]

$$\boldsymbol{\mu}_n = \gamma \mu_N \boldsymbol{\sigma} = \gamma \frac{e\hbar}{2m_p} \boldsymbol{\sigma} \quad (3.1.1)$$

where $\gamma = -1.913$ is the gyromagnetic ratio for a neutron, μ_N is the nuclear magneton, which consists of the elementary charge e , the reduced Planck constant \hbar , and the mass of the proton m_p . At first glance it is odd that the neutron has a magnetic moment in the first place since it requires the particle in question to have an electric charge, and the neutron has 0. However the neutron is a composite particle made up of one up quark and two down quarks each with electric charge of $+2/3$ and $-1/3$ respectively. Each of these quarks have a magnetic moment of their own, which combine to give the neutron its magnetic moment as shown in [31]. In addition neutrons possess the particle-wave duality common to all particles. A neutron moving with constant speed v has a De-Broglie wavelength of

$$\lambda = \frac{2\pi\hbar}{mv}. \quad (3.1.2)$$

The neutron wave number k is defined as

$$k = \frac{2\pi}{\lambda}. \quad (3.1.3)$$

k is the length of the wave vector \mathbf{k} , which has the same direction as the velocity.

3.2 Why Neutrons?

The experimental technique used in the work of this thesis is all based on neutron scattering. Neutron scattering is used to investigate the structure and dynamics of materials, so the use of it covers much the same area of investigation as X-ray scattering. However, compared to X-rays, you need large scale facilities to produce neutrons in any significant amount to do experiments other than of the most elementary sort. As such neutron facilities are sadly fairly rare despite the fact that the properties of neutrons make it an extremely efficient probe to measure several properties of interest to a broad range of scientific fields, and in a number of cases the neutron is vastly superior to X-rays.

The wavelength of a neutron beam can be tuned to be in the same order of magnitude as the typical inter-atomic distances in a crystal lattice ($\sim 2\text{\AA}$). As such neutron scattering can be used alongside X-rays to do crystallography experiments. In addition, due to the fact that a neutron has a magnetic moment, it can be used to resolve magnetic structures as well, giving it a distinct edge over X-rays when it comes to the study of magnetism.

Using a moderator the energy of neutrons can be tuned to that of excitations in the crystal lattice, and those in the magnetic structure, section 2.3 gives a general introduction to the theory of these excitations. The energy of these excitations are typically in the meV range, which can be achieved by cold and thermal neutrons ($\sim 1 - 200\text{meV}$). The possibility to study excitations with neutrons is one of the premier reasons to choose the technique over X-rays, which typically has energies in the $\sim 100\text{keV}$ range, which are much too large to effectively study excitations. You can produce X-rays with more reasonable energies, down to around 20 meV, but this comes with a large loss of flux and the energy resolution will be considerably worse than that of e.g. a Triple Axis Spectrometer, see section 3.5.1.

Neutrons only interact weakly with most atoms, this allows neutrons to penetrate deep into samples and are such able to study bulk samples. In addition neutrons can fairly easily penetrate sample environments, making the technique ideal for experiments requiring a cryostat, furnace, high pressure, etc. One last bonus of this is that higher order effects e.g. more than one interaction with the sample are fairly uncommon, and therefore neutron data is fairly simple to compare with theoretical models.

The scattering cross section of neutrons varies enormously between atoms, and even between isotopes of the same atom. The reason for this seemingly random cross section is not fully understood, however it is very useful. For an example the scattering cross section of hydrogen is much larger for neutrons than it is for X-rays, which hardly interacts with hydrogen at all. This makes neutrons ideal for studying samples where hydrogen matter like biological samples and certain types of cements. In addition the huge contrast between isotopes of the same atom can be used to distinguish between them using neutrons, and clever use of isotope concentrations can give valuable insight into the structure of e.g. biological samples.

3.3 Neutron Scattering

The method of neutron scattering is an experimental technique, where neutrons are fired at a sample, interacts with it in some manner, and then hits a detector. This section will deal with neutrons interaction with the sample, where the next one will explain how neutrons are produced, guided to their target, and then finally measured.

Scattering Cross Section

When neutrons interact with a sample, its cross section σ is a measure of how large the interaction is. For low cross sections the sample is very transparent and neutrons easily penetrate deep and all the way through the sample, whereas for high cross sections the sample becomes more opaque and interacts heavily with the neutrons. To develop an expression for the cross section we first need to define the flux Ψ . The flux is defined as the number of neutrons per second that goes through a given surface area perpendicular to the beam of neutrons [9]:

$$\Psi = \frac{\text{Number of neutrons per second}}{\text{Surface area perpendicular to the neutron beam}}. \quad (3.3.1)$$

The flux is often given in the unit n/cm^2 . Now the scattering cross section σ can be defined as the fraction between the number of neutrons scattered per second and the flux

$$\sigma = \frac{\text{Number of neutrons scattered pr second}}{\Psi} \quad (3.3.2)$$

which is in units of area.

3.3.1 Differential scattering cross section

A relevant parameter is the angular dependence of the scattered neutrons, as such we define a differential scattering cross section as the number of neutrons per second scattered into a given solid angle $d\Omega$

$$\frac{d\sigma}{d\Omega} = \frac{\text{Number of neutrons scattered per second into solid angle } d\Omega}{\Psi d\Omega}. \quad (3.3.3)$$

This can be further developed to allow inelastic scattering, where energy is exchanged between the incident neutrons and the sample. In inelastic scattering a energy transfer to or from the sample of size $\Delta E = \hbar\omega$ is given by

$$\hbar\omega = E_i - E_f = \frac{\hbar(k_i^2 - k_f^2)}{2m_n} \quad (3.3.4)$$

where E denotes the energy, the "i" and "f" subscript denotes initial and final state respectively, k is the length of the wave vector. The energy transfer of inelastic neutron scattering can be included in the cross section, by defining the

$$\frac{d^2\sigma}{d\Omega dE_f} = \frac{\text{Number of neutrons scattered per second into solid angle } d\Omega \text{ with energies } [E_f; E_f + dE_f]}{\Psi d\Omega dE_f}. \quad (3.3.5)$$

partial differential cross section as

3.3.2 Semi-classical description of elastic scattering

Following a semi-classical approach we can determine how neutrons scatter elastically of the nuclei of atoms.

First the neutron can be described as a complex plane wave function ψ with the form [9]

$$\psi_i(\mathbf{r}) = \frac{1}{\sqrt{Y}} e^{i\mathbf{k}_i \cdot \mathbf{r}} \quad (3.3.6)$$

where Y is simply a normalization factor. When the initial neutron plane wave interacts with a single nuclei labeled j , it scatters, and the final neutron wave has the form of a sphere. If we assume elastic scattering the final neutron wave is on the form

$$\psi_f(\mathbf{r}) = \psi_i(\mathbf{r}_j) \frac{-b_j}{|\mathbf{r} - \mathbf{r}_j|} e^{ik_f |\mathbf{r} - \mathbf{r}_j|} \quad (3.3.7)$$

where b_j is called the scattering length since it has the dimension of length. The value of the scattering length is an intrinsic property of any given nuclei and can have both positive and negative values. The sign in front of b_j is chosen such that most nuclei has a positive value of scattering length [9].

Expanding the above to elastic scattering from two nuclei, labeled j and j' , with equal scattering lengths $b_j = b_{j'} \equiv b$. The above becomes

$$\psi_f(\mathbf{r}) = -b \left(\frac{\psi_i(\mathbf{r}_j)}{|\mathbf{r} - \mathbf{r}_j|} e^{ik_f |\mathbf{r} - \mathbf{r}_j|} + \frac{\psi_i(\mathbf{r}_{j'})}{|\mathbf{r} - \mathbf{r}_{j'}|} e^{ik_f |\mathbf{r} - \mathbf{r}_{j'}|} \right) \quad (3.3.8)$$

which following the procedure in [9] can be rewritten as

$$\psi_f(\mathbf{r}) = -\frac{b}{r\sqrt{Y}} e^{i\mathbf{k}_f \cdot \mathbf{r}} \left(e^{i(\mathbf{k}_i - \mathbf{k}_f) \cdot \mathbf{r}_j} + e^{i(\mathbf{k}_i - \mathbf{k}_f) \cdot \mathbf{r}_{j'}} \right). \quad (3.3.9)$$

By defining the central concept of the scattering vector

$$\mathbf{q} = \mathbf{k}_i - \mathbf{k}_f \quad (3.3.10)$$

and generalizing to a system of particles, potentially with different scattering lengths we get

$$\psi_f(\mathbf{r}) = -\frac{1}{r\sqrt{Y}} e^{i\mathbf{k}_f \cdot \mathbf{r}} \sum_j b_j e^{i\mathbf{q} \cdot \mathbf{r}_j}. \quad (3.3.11)$$

where the sum is over all particles j with scattering lengths b_j . To get the differential scattering cross section we use that the flux can be written as the

$$\Psi = v|\psi|^2 \quad (3.3.12)$$

which means that the flux through any small area dA can be expressed as $v|\psi|^2 dA$ [9], such that the number of neutrons scattered through the small area dA is $v_f |\psi_f|^2 dA$. Now the differential scattering cross section (3.3.3) can be rewritten as

$$\frac{d\sigma}{d\Omega} = \frac{v_f |\psi_f|^2 dA}{v_i |\psi_i|^2 d\Omega}. \quad (3.3.13)$$

Using (3.1.2) and (3.1.3) and assuming all scattering to be elastic, we see that $v_f = v_i$ and as such the above becomes

$$\frac{d\sigma}{d\Omega} = \frac{|\psi_f|^2 dA}{|\psi_i|^2 d\Omega}. \quad (3.3.14)$$

Using that $dA = r^2 d\Omega$ [9] we get

$$\frac{d\sigma}{d\Omega} = \frac{|\psi_f|^2 r^2}{|\psi_i|^2}. \quad (3.3.15)$$

inserting the expression for the initial (3.3.6) and final (3.3.11) wave functions we get

$$\frac{d\sigma}{d\Omega} = \frac{|\frac{1}{r\sqrt{Y}} e^{i\mathbf{k}_f \cdot \mathbf{r}} \sum_j b_j e^{i\mathbf{q} \cdot \mathbf{r}_j}|^2 r^2}{|\frac{1}{\sqrt{Y}} e^{i\mathbf{k}_i \cdot \mathbf{r}}|^2}. \quad (3.3.16)$$

the minus sign has been removed from the final wave function, since we take the numerical value and square it anyway. Reducing the above yields

$$\frac{d\sigma}{d\Omega} = \frac{|e^{i\mathbf{k}_f \cdot \mathbf{r}} \sum_j b_j e^{i\mathbf{q} \cdot \mathbf{r}_j}|^2}{|e^{i\mathbf{k}_i \cdot \mathbf{r}}|^2}. \quad (3.3.17)$$

Now using that $|e^{i\mathbf{a}}|^2 = 1$ we obtain the final equation for the elastic scattering of neutrons on a system of nuclei

$$\frac{d\sigma}{d\Omega} = \left| \sum_j b_j e^{i\mathbf{q} \cdot \mathbf{r}_j} \right|^2. \quad (3.3.18)$$

For any system with a significant amount of nuclei the above sum will almost always be zero, except when $\mathbf{q} \cdot \mathbf{r}_j = 2\pi n$. When this condition is fulfilled constructive interference occurs and scattering occurs for that value of \mathbf{q} . When using neutron scattering on a periodic crystalline sample, with reciprocal lattice vector length $\tau = 2\pi/d$, where d is the inter-atomic distance between neighboring nuclei, then the length of \mathbf{r}_j must be $r_j = a$ as such the condition $\mathbf{q} \cdot \mathbf{r}_j = 2\pi n$ is therefore met when

$$\mathbf{q} = \boldsymbol{\tau} \quad (3.3.19)$$

which is often called the Laue condition.

The figure 3.1 illustrates the scattering geometry and shows the scattering \mathbf{q} vector, as well as the initial and final wave vectors \mathbf{k}_i and \mathbf{k}_f . In addition the figure illustrates the concept of the scattering angle θ . In an experiment however, one would measure 2θ . In an elastic experiment the scattering angle relates to the scattering vector by the following equation

$$q = 2k \sin(\theta) = \frac{4\pi \sin(\theta)}{\lambda} \quad (3.3.20)$$

Using the Laue condition and rearranging the terms we obtain Bragg's law.

$$n\lambda = 2d \sin(\theta). \quad (3.3.21)$$

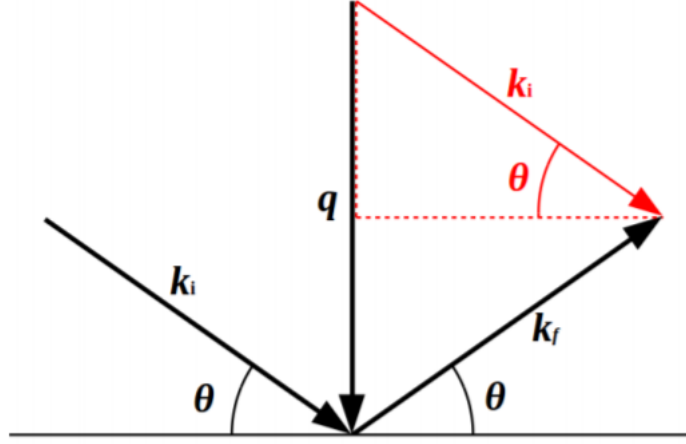


Figure 3.1: This figure demonstrates the scattering geometry, with the initial \mathbf{k}_i and \mathbf{k}_f wave vectors, the scattering vector \mathbf{q} , and the scattering angle θ . Figure from [10].

Expanding (3.3.18) to allow for more complex structures, the sum is divided into a sum over the atoms in a unit cell, denoted with subscript j , and a sum over the unit cells themselves, denoted with subscript k ,

$$\frac{d\sigma}{d\Omega} = \left| \sum_{j,k} b_j e^{i\mathbf{q}\cdot(\mathbf{r}_j + \mathbf{r}_k)} \right|^2 = \left| \sum_j b_j e^{i\mathbf{q}\cdot\mathbf{r}_j} \right|^2 \left| \sum_k e^{i\mathbf{q}\cdot\mathbf{r}_k} \right|^2 \quad (3.3.22)$$

since scattering only occurs when the Laue-condition is fulfilled such that the scattering vector is equal to that of a reciprocal lattice vector, the sum over the unit cells can be simplified to

$$\left| \sum_k e^{i\mathbf{q}\cdot\mathbf{r}_k} \right|^2 = N \sum_k \delta(\mathbf{q} - \boldsymbol{\tau}) \quad (3.3.23)$$

where N is the number of cells and $\delta(\mathbf{q} - \boldsymbol{\tau})$ is a delta function ensuring that the Laue-condition are met. As such (3.3.22) becomes

$$\frac{d\sigma}{d\Omega} = N \sum_k \delta(\mathbf{q} - \boldsymbol{\tau}) \left| \sum_j b_j e^{i\mathbf{q}\cdot\mathbf{r}_j} \right|^2 \quad (3.3.24)$$

The sum over the atoms inside the unit cell is known as the nuclear structure factor F_N

$$F_N = \left| \sum_j b_j e^{i\mathbf{q}\cdot\mathbf{r}_j} \right|^2 \quad (3.3.25)$$

The intensity you measure in a neutron scattering experiment is proportional to

$$I \propto \sum_k \delta(\mathbf{q} - \boldsymbol{\tau}) |F_N|^2 \quad (3.3.26)$$

where the proportionality depends on a number of factors including the sample volume the incoming intensity on the sample, and the so called Debye-Waller factor e^{-2W} which is a term that accounts for the thermal vibrations of neutrons [9].

3.3.3 Inelastic neutron scattering

When a neutron interacts with the nuclei of a sample it may transfer energy to or from the sample. This process is known as inelastic scattering. When conducting inelastic scattering experiments the partial differential cross section is measured (3.3.5). The explicit derivation of the partial differential cross section is shown in Lefmann [9], which finds

$$\left(\frac{d^2\sigma}{d\Omega dE_f} \right)_{\lambda_i \rightarrow \lambda_f} = \frac{k_f}{k_i} \left(\frac{m_n}{2\pi\hbar^2} \right)^2 \left| \langle \lambda_i \psi_i | \hat{V} | \lambda_f \psi_f \rangle \right|^2 \delta(\hbar\omega - (E_{\lambda_f} - E_{\lambda_i})) \quad (3.3.27)$$

where $\langle \lambda_f \psi_f |$ and $| \lambda_i \psi_i \rangle$ is the final and initial state of the sample, the delta function ensures that energy is conserved such that the energy transferred to or from the sample equals the energy transferred from or to the neutron. Finally \hat{V} is the scattering potential often approximated by the fermi pseudo potential

$$\hat{V} = \frac{2\pi\hbar^2}{m_n} \sum_j b_j \delta(\mathbf{r} - \mathbf{r}_j) \quad (3.3.28)$$

where the sum is over all the atoms j .

3.3.4 One-phonon cross section

As explained in section 2.3 if the sample is has a crystal structure, then the lattice vibrations will be quantized, each with energy $\hbar\omega$. For a simple Bravais lattice, with one atom in a unit cell, a single phonon can be created or absorbed by a neutron interacting with the lattice. The partial differential cross section for this simple lattice is computed in Lefmann [9] and is

$$\begin{aligned} \left(\frac{d^2\sigma}{d\Omega dE_f} \right)_{\lambda_i \rightarrow \lambda_f} &= e^{-2W} \frac{k_f}{k_i} b^2 \frac{(2\pi)^3}{2MV_0} \sum_{q'} \sum_{\tau} \sum_{p=1}^3 \frac{(\mathbf{q}' \cdot \mathbf{e}_{q',p})}{\omega_{q',p}} \\ &\times ((n_{q',p} + 1)\delta(\omega - \omega_{q',p})\delta(\mathbf{q} - \mathbf{q}' + \boldsymbol{\tau}) \\ &+ n_{q',p}\delta(\omega + \omega_{q',p})\delta(\mathbf{q} + \mathbf{q}' + \boldsymbol{\tau})) \end{aligned} \quad (3.3.29)$$

where e^{-2W} is the Debye-Waller Factor, M is the nuclear mass of the atoms in the unit cell, $\mathbf{e}_{q',p}$ is a polarization unit vector, such that the product $(\mathbf{q}' \cdot \mathbf{e}_{q',p})$ ensures that the neutron only interacts with vibrations that are parallel with the scattering vector \mathbf{q}' . The term on the second line accounts for a neutron transferring some energy to the lattice and as such creating a phonon, while the term on the third line is the opposite process, where a neutron absorbs energy from the lattice and as such annihilating a phonon. The term $n_{q',p}$ is the occupation number, which from Bose statistics is given by eq. 2.3.6. The $+1$ in the 2nd line illustrates the fact that at zero temperature you can only create phonons, while no phonons exists that can be absorbed, since $n_{q',p} = 0$.

3.3.5 Magnetic neutron scattering

Neutrons carry a magnetic moment, and as such interact with any magnetic field they encounter. Some atoms and ions create magnetic fields due to unpaired electrons orbiting in their shells and the spin of the electrons themselves. Because of this, and the high penetration of neutrons, they can be used as a probe to investigate the magnetic structure and dynamics within a sample. The neutron interacts with a magnetic field through the nuclear Zeeman term H_z in an external magnetic field \mathbf{B}

$$H_Z = -\boldsymbol{\mu} \cdot \mathbf{B} = -\gamma\mu_N \hat{\boldsymbol{\sigma}} \cdot \mathbf{B}, \quad (3.3.30)$$

where γ is the gyromagnetic ratio, μ_N is the magnetic moment of the neutron, and $\hat{\boldsymbol{\sigma}}$ is the Pauli spin matrices of the neutron. Since we assume that the angular contribution to the magnetic moment is quenched, see section 2.2.1, only the magnetic moment of the electrons spin $\boldsymbol{\mu}_{e,j}$ contribute

$$\boldsymbol{\mu}_{e,j} = -g\mu_B \mathbf{s}_j \quad (3.3.31)$$

where g is the g-factor, μ_B is the Bohr magneton and \mathbf{s}_j is the spin of the electron. The magnetic field from a dipole placed at the origin is

$$\mathbf{B} = \frac{\mu_0}{4\pi} \nabla \times \left(\boldsymbol{\mu}_e \times \frac{\mathbf{r}}{r^3} \right). \quad (3.3.32)$$

Inserting (3.3.31) yields

$$\mathbf{B}_j = -\frac{\mu_0}{4\pi} g\mu_B \nabla \times \left(\mathbf{s}_j \times \frac{\mathbf{r}}{r^3} \right) \quad (3.3.33)$$

which we insert into (3.3.30), giving

$$H_{Z,j} = \frac{\mu_0}{4\pi} g\mu_B \gamma\mu_N \hat{\boldsymbol{\sigma}} \cdot \nabla \times \left(\frac{\mathbf{s}_j \times (\mathbf{r} - \mathbf{r}_j)}{|\mathbf{r} - \mathbf{r}_j|^3} \right). \quad (3.3.34)$$

This term is used as the potential, V , in the expression for the partial differential cross section (3.3.27) leading to this expression for the magnetic partial differential cross section for neutrons

$$\begin{aligned} \left(\frac{d^2\sigma}{d\Omega dE_f} \right)_{\sigma_i \rightarrow \sigma_f, \lambda_i \rightarrow \lambda_f} &= \frac{k_f}{k_i} \left(\frac{m_n}{2\pi\hbar^2} \frac{\mu_0}{4\pi} g\mu_B \gamma\mu_N \right)^2 \sum_{\lambda_i, \lambda_f} p_{\lambda_i} \\ &\times \left| \langle \mathbf{k}_i \lambda_i \sigma_i | \sum_j \hat{\boldsymbol{\sigma}} \cdot \nabla \times \left(\frac{\mathbf{s}_j \times (\mathbf{r} - \mathbf{r}_j)}{|\mathbf{r} - \mathbf{r}_j|^3} \right) | \mathbf{k}_f \lambda_f \sigma_f \rangle \right|^2 \\ &\times \delta(\hbar\omega - (E_{\lambda_f} - E_{\lambda_i})) \end{aligned} \quad (3.3.35)$$

where $\sum_{\lambda_i, \lambda_f} p_{\lambda_i}$ is a sum over all possible final states of the sample, and over all initial states which occur with probability p_{λ_i} .

Again an explicit derivation of the full magnetic partial differential cross section can be seen in Lefmann [9], but the above is transformed into

$$\begin{aligned} \left(\frac{d^2\sigma}{d\Omega dE_f} \right)_{magn} &= (\gamma r_0)^2 \frac{k_f}{k_i} \left[\frac{g}{2} F(q) \right]^2 e^{-2W} \sum_{\alpha\beta} (\delta_{\alpha\beta} - \hat{\mathbf{q}}_\alpha \hat{\mathbf{q}}_\beta) \\ &\times \frac{N}{2\pi\hbar} \int_{-\infty}^{\infty} \sum_j e^{i\mathbf{q}\cdot\mathbf{r}_j} \langle s_0^\alpha(0) s_j^\beta(t) \rangle e^{-i\omega t} \end{aligned} \quad (3.3.36)$$

where $\exp(-2W)$ is the Debye-Waller factor, α and β run over the Cartesian coordinates (x, y, z) , $\langle \rangle$ means thermal average, and $F(q)$ is the magnetic form factor

$$F(q) = \int e^{i\mathbf{q}\cdot\mathbf{r}} \hat{s}(\mathbf{r}) d^3\mathbf{r} \quad (3.3.37)$$

where $\hat{s}(\mathbf{r})$ is the normalized spin density. Equation (3.3.36) is the starting point of most calculations of the magnetic scattering cross section. Equation (3.3.36) is the Fourier transform of the spin-spin correlation function, see e.g [32] for a more general introduction to correlation functions.

In the special case of elastic scattering off of a ordered magnetic crystal structure the magnetic differential cross section simplifies to

$$\left(\frac{d\sigma}{d\Omega} \right)_{magn.,el.} = (\gamma r_0)^2 \left[\frac{g}{2} F(q) \right]^2 \frac{N(2\pi)^3}{V_0} e^{-2W} |F_M(\mathbf{q})|^2 \sum_{\boldsymbol{\tau}} (\mathbf{q} - \boldsymbol{\tau} - \mathbf{Q}) \quad (3.3.38)$$

see section 2.1 for a description of the reciprocal lattice vector $\boldsymbol{\tau}$ and the ordering vector of the magnetic structure \mathbf{Q} , $F_M(\mathbf{q})$ is the magnetic structure factor, which is analogous to the nuclear structure factor, equation (3.3.25), in that it is a sum of the magnetic moments inside the magnetic unit cell. The magnetic structure factor takes the form

$$F_M(\mathbf{q}) = \sum_j e^{-i\mathbf{q}\cdot\boldsymbol{\Delta}_j} \langle \mathbf{s}_{j,\perp} \rangle \quad (3.3.39)$$

where $\boldsymbol{\Delta}_j$ is a vector pointing to the magnetic sites inside the magnetic unit cell and $\mathbf{s}_{j,\perp}$ is the spin component perpendicular to \mathbf{q} . Since YMnO₃ is an antiferromagnet, the result of the inelastic magnetic scattering cross section for an antiferromagnet will be stated here, see Lefmann [9] for a derivation from equation (3.3.36).

$$\begin{aligned} \left(\frac{d^2\sigma}{d\Omega dE_f} \right)_{magn} &= (\gamma r_0)^2 \frac{k_f}{k_i} \left[\frac{g}{2} F(q) \right]^2 e^{-2W} (1 + \hat{q}_z^2) \frac{1}{4} \frac{(2\pi)^3}{V_0} \\ &\times \left[\sum_{\mathbf{q}', \boldsymbol{\tau}, a} \left(n_B \left(\frac{\hbar\omega_{a,\mathbf{q}'}}{k_B T} \right) + 1 \right) \delta(\hbar\omega_{\mathbf{q}'} - \hbar\omega) \delta(\mathbf{q}' - \mathbf{q} - \boldsymbol{\tau}) \right. \\ &\left. + n_B \left(\frac{\hbar\omega_{a,\mathbf{q}'}}{k_B T} \right) \delta(\hbar\omega_{\mathbf{q}'} + \hbar\omega) \delta(\mathbf{q}' + \mathbf{q} - \boldsymbol{\tau}) \right] \\ &\times [u_{\mathbf{q}'}^2 + v_{\mathbf{q}'}^2 + 2u_{\mathbf{q}'}v_{\mathbf{q}'} \cos(\boldsymbol{\rho} \cdot \boldsymbol{\tau})] \end{aligned} \quad (3.3.40)$$

here $\boldsymbol{\tau}$ is the reciprocal lattice vector of a sub lattice, $\boldsymbol{\rho}$ is a vector joining the sub lattice, and n_B is the Bose factor. The equation is to be understood in the following way: The 2nd line creates a spin wave of energy $\hbar\omega$ by absorbing an equal amount of energy $\hbar\omega_{\mathbf{q}'}$ from a neutron, whereas the 3rd line annihilates a spin wave by transferring it to a neutron. The last line is a coherence factor, the final term, $\cos(\boldsymbol{\rho} \cdot \boldsymbol{\tau})$ is 1 at a nuclear peak and -1 at an anti ferromagnetic peak. The other terms are

$$\begin{aligned} u_{\mathbf{q}'}^2 + v_{\mathbf{q}'}^2 &= 2S \frac{2SJ(0) - 2s[J_1(0) - J_1(\mathbf{q}')] + 2g\mu_B B_A}{\Omega(\mathbf{q}')} \\ u_{\mathbf{q}'} v_{\mathbf{q}'} &= - \frac{(2S)^2 J(\mathbf{q}')}{2\Omega(\mathbf{q}')} \end{aligned} \quad (3.3.41)$$

where

$$\Omega(\mathbf{q}') = \sqrt{[SJ(0) - S(J_1(0) - J_1(\mathbf{q}')) + g\mu_B B_A]^2 - S^2 J(\mathbf{q}')^2} \quad (3.3.42)$$

where B_A is the size of the effective anisotropy field \mathbf{B}_A , S comes from the produkt of the spins on identical sites $S^2 = \mathbf{S}_j \cdot \mathbf{S}_j$, and finally $J(\mathbf{q}')$ is the fourier transform of the spin-spin interaction of neighbouring sites

$$J(\mathbf{q}') = \sum_{\delta} J_{\delta} e^{i\mathbf{q}' \cdot \mathbf{r}_{\delta}} \quad (3.3.43)$$

here the subscript δ refers to the neighbour number, such that 1 is nearest neighbour and so forth, J_{δ} is the coupling strength between a spin and its neighbour, see equation (2.2.18). J is the coupling of spins on the opposite sub lattice of the antiferromagnet, while J_1 is the coupling of spins on the same sublattice, see figure 2.6.

3.3.6 Critical scattering

Critical scattering is the additional scattering that occurs close to the Néel temperature T_N due to the divergence of the correlation length ξ between the magnetic moments in the sample as T_N is approached. In an experiment this critical scattering is seen as a Lorentzian broadening of the signal because the spin-spin correlation function from equation 3.3.36 can be reasonably approximated by an exponential function

$$\langle s_0^{\alpha}(0) s_j^{\beta}(t) \rangle \approx e^{-\frac{r}{\xi}} \quad (3.3.44)$$

where \mathbf{r} is the distance between the two spins and ξ is the correlation length at a given temperature. As such the correlation function decays exponentially as the distance between two spins is increased. When this expression is Fourier transformed into \mathbf{q} -space it becomes a Lorentzian distribution.

$$\mathcal{F}_{\mathbf{r}}(e^{-\frac{r}{\xi}})(\mathbf{q}) = \frac{1}{\xi} \frac{1}{|\mathbf{q} - \mathbf{Q}|^2 + \frac{1}{\xi^2}} \quad (3.3.45)$$

which is what is measured in an experiment using elastic neutrons.

3.4 Neutron Instrumentation

In order to utilize neutrons for scattering experiments, you need to ensure that you can produce and deliver neutrons to a target experiment, and finally also detect the neutrons that scatter off your sample. In addition you are often only interested in neutrons with the correct properties, e.g. a specific energy. Therefore the 'white' neutron beam is often attenuated to ensure that only neutrons with the desired properties interact with the sample or are detected.

3.4.1 Neutron production

An effective production method of neutrons is needed. Currently there are two main methods of neutron production. The first is using a nuclear reactor as the source, where the neutrons that escape the reactor core can be used as a continuous source. The second method is called spallation, where a heavy element is bombarded with high energy protons, exciting the nuclei of the atoms which then emits a number of neutrons.

Nuclear reactors fission heavy actinide elements, most commonly Uranium-235, by bombarding the nucleus of the isotope with thermal neutrons. During the fission process the nucleus of the atom split into two small nuclei and a number of new fast neutrons. A schematic of a typical fission reaction can be seen in the top of figure 3.2. To maintain the chain reaction in the reactor, these fast neutrons are then slowed by a moderator to thermal energies, and then interact with new Uranium nuclei. However, since reactors have a finite size, some of these produced neutrons will inevitably escape the reactor core. These escapees can then be used as the source of neutrons for experiments.

Spallation works differently. A spallation source works by accelerating a proton to a fraction of the speed of light. The energy of this proton at the end of the accelerator is usually in the $1 - 3\text{GeV}$ range. This proton is then fired into a heavy, neutron rich, element like wolfram [9]. This high energy proton highly excites the target nuclei releasing a large number of fragments of which 10-20 are neutrons. These neutrons can then be used for experiments. The reaction in a spallation source is illustrated in the bottom picture of figure 3.2. For a more detailed introduction to nuclear and reactor physics see textbooks like Krane [33] and Stacey [34].

3.4.2 The moderator

The neutrons produced in both reactors and spallation sources are fast neutrons, with energies in the MeV range. Fast neutrons are used in some reactors, and for experiments in reactor physics, however, for almost all scattering experiments in material research the energy of these 'raw' neutrons are several orders of magnitude too high. Therefore a moderator is used to slow them down. A moderator is simply a material which has some temperature. When the neutrons enters the moderator they will hit the molecules of the moderator and transfer some of their kinetic energy to them. Thus the neutrons will quickly reach thermal equilibrium with the moderator and have an energy similar to that of the temperature of the moderator. It is important that the material the moderator is made from has fairly high scattering cross section, thereby ensuring that thermal equilibrium between neutrons and moderator happens rapidly. At

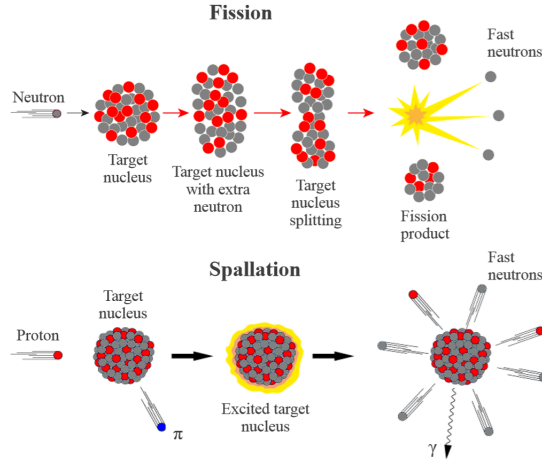


Figure 3.2: On the top figure the process of nuclear fission is depicted. A target nucleus is hit by an incoming neutron, this can create a highly unstable nucleus which splits into two daughter nuclei and a number of fast neutrons depending on the exact reaction. The bottom figure show the spallation process where a high energy proton hits a heavy target nucleus which become excited, the excited nucleus then releases a high number of fast neutrons. Figures adapted from [35] and [36]

the same time it should have a low absorption cross section as you want the neutrons to persist. Examples of moderators are water and graphite.

3.4.3 Neutron guides

having produced the neutrons and changed their energy to a more desirable level, the next step is to get the neutrons to the target. For this a neutron guide is used. A neutron guide uses that neutrons, like photons, can experience total reflection from a surface if the incident angle is low enough. As such it is possible to transport neutrons through a guide system to a target, as long as the incident angle is kept sufficiently low.

The maximum angle that can give rise to total reflection is defined as the critical angle $\theta(\lambda)_c$, which depends on the wavelength of the incident neutron. A critical scattering vector q_c can be defined from eq. 3.3.20 as

$$q_c = 2k \sin(\theta(\lambda)_c) \approx 4\pi \frac{\theta(\lambda)_c}{\lambda} \quad (3.4.1)$$

Above the critical angle, the reflectivity for neutrons falls off very quickly. Most commonly nickel is used as the guide material. The critical scattering vector for nickel is

$$q_{c,Ni} = 0.0217 \text{ \AA}^{-1} \quad (3.4.2)$$

To increase the reflectivity of guides above $\theta(\lambda)_c$, multiple layers are used. The effect of making multiple layers is that the reflectivity decreases more slowly as

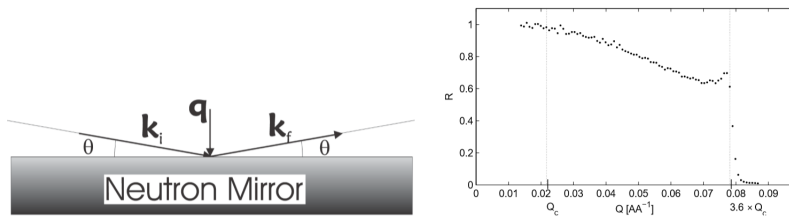


Figure 3.3: Left: The scattering geometry of a neutron guide, where total reflection occurs off of the side, when the incident neutrons come in at an angle at or below the critical angle $\theta(\lambda)_c$. Right: The reflectivity of a multilayer nickel neutron guide as a function of q . The effect of the multiple layers is to extend the range of q 's where the reflectivity of the guide is nonzero. Figures from [9].

you go above the critical angle of the outermost layer [9]. The geometry of total reflection from a neutron guide as well as the reflectivity as a function of q can be seen in figure 3.3.

The neutron guide will in most cases be slightly curved. With a curved guide high energy neutrons with a small wavelength will not be reflected by the sides of the guide. This ensures that none of the high energy neutrons that might make it through the moderator does not reach the experiment, in addition it will remove some of the higher order neutrons that would otherwise be Bragg reflected by the monochromator.

3.4.4 Monochromators

It is often of great value to know the properties of the incident neutrons on the target. One method to select a specific wavelength from a source of 'white' neutrons is to use a monochromator crystal. A monochromator crystal is a crystal with a well known lattice spacing d , if the direction of incoming neutrons is well known then according to Bragg's law, eq. 3.3.21, only neutrons with wavelengths which fulfill the Laue condition, eq. 3.3.19, will be scattered from the crystal. The first order of scattered neutrons from a monochromator correspond to $n = 1$ in Bragg's law, the 2nd order to $n = 2$ and so on, see equation 3.3.21. These neutrons are then Bragg reflected toward the sample position.

3.4.5 Filters, slits and collimators

To further refine the properties of the beam a number of inserts on the beam can be used if necessary. To remove any remaining higher order neutrons that made it through the guide and was reflected off of the monochromator a filter is often used. A typical filter is the beryllium filter or a berylliumoxide filter, these transmit neutrons below a certain energy because Bragg scattering cannot take place if the wavelength of the neutron is more than twice that of the lattice spacing in the crystal, see equation 3.3.21. Therefore a Be filter transmits neutrons with a energy of less than 5.2 meV, while a BeO filter transmits neutrons of less than 3.8 meV [9]. Using filters such as these, some or all of the undesired higher order neutrons from the monochromator can be removed.

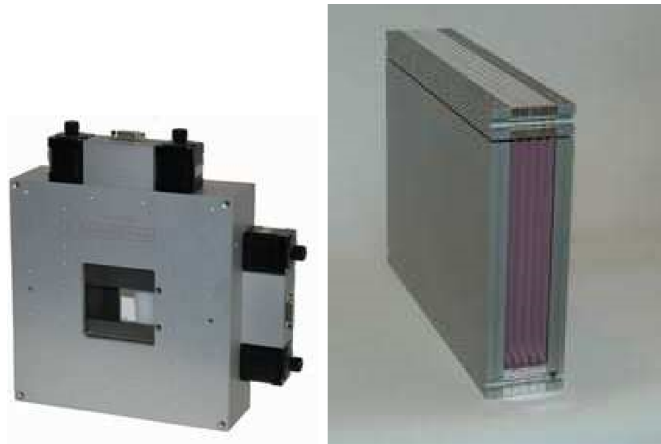


Figure 3.4: Left: A slit with an adjustable hole. A slit is used to remove neutrons that would not hit the sample from the beam, thus reducing background levels. Two slits in a row can be used to make a pinhole collimator, which in addition also reduces the divergence of the incident neutron beam. Right: A Soller collimator. The thin equidistant slices are made of a neutron absorbing material, the parallel slices reduce the divergence. Pictures are from the vendor JJ-Xray APS [37].

In an experiment one wants to minimize the number of neutrons not hitting the sample as these will contribute to the background. Therefore an adjustable slit is used, made from neutron absorbing materials, such that the opening is as close as possible to the dimensions of the sample. Two such slits can be used after one another to reduce the divergence of the beam, by only allowing neutrons which pass through both holes to reach the sample. This is called pinhole collimation.

Another type of collimator is a Soller collimator, which consists of a number of thin, equidistant slices of neutron absorbing materials placed parallel to each other. The walls of the collimator will absorb neutrons hitting the walls, and such the divergence is decreased depending on the distance between the slices and the length of the collimator. An example of a slit and Soller collimator can be seen in figure 3.4.

Sometimes the properties of the scattered neutrons will need to be controlled as well. As such a collimator and filter can also be installed after the sample, e.g. a filter could be used to remove higher order scattering from the sample. If you need to control the energy of your scattered neutrons a monochromator can be installed after the sample, if this is the case the monochromator crystal is called an analyzer crystal which is the principle in a Triple Axis Spectrometer as used in this work, see section 3.5.1.

3.4.6 Neutron detectors

The neutrons that scatter off of the sample, as described in section 3.3, then need to be detected. Neutrons can interact with the nuclei of atoms, as such detection processes involve measuring whether such an interaction has hap-

pened. Neutron capture is used as the detection method. When a neutron is captured by an atom it can create a fairly large amount of energy, the high energy particles released can then be detected in very much the same way as ionizing radiation in a Geiger-Müller counter. The most efficient and most used is neutron capture in Helium-3.



While He-3 detectors are the most common other types of detectors also see use. e.g. ${}^6_3\text{Li}$ and ${}^{10}_5\text{B}$.

The monitor is a special kind of neutron detector. The role of the monitor is to normalize the number of neutrons coming from the source, which may fluctuate. To ensure that a set of measurements all have the same counting statistics one usually takes data until a certain monitor count is reached before the next measurement happens. If time was used instead, you would have to take the fluctuations of the source into account. A monitor is a weak neutron detector that only detects a small fraction, usually in the range of 1 in 100 to 1 in 1000, of the neutrons passing through it, the rest is allowed to continue towards the experiment. The monitor is usually placed at the end of the guide system.

3.5 Neutron Spectroscopy

Of the myriad of possible neutron scattering experiments only the Triple Axis Spectrometer will be introduced in this work, as it is the only experimental technique that have been used. A triple axis instrument can perform both elastic and inelastic measurements, both techniques will be utilized in this work.

3.5.1 Triple axis spectrometers

A triple axis spectrometer, or TAS, is a kind of neutron scattering experiment, which is designed such that both the energy of the incoming neutrons and the energy of the scattered neutrons are known. This makes it possible to measure the energy transfer happening inside the sample and as such measure both structural excitations, phonons, and magnetic excitations, magnons, see section 2.3. Bertram Brockhouse shared the 1994 Nobel prize in physics for the innovative design of the TAS experiment which were developed in 1955-1956 at Chalk River Laboratories in Canada.

The basic layout of a TAS experiment can be seen in figure 3.5. From the source, the white neutron beam travel through a guide system to a monochromator crystal, which select a few specific wavelengths from the white beam. In a TAS experiment the monitor is usually placed right after the monochromator crystal.

A triple axis experiment has 3 axes of rotation hence why it is named so. These are the rotation of the monochromator crystal that is used to select the wavelength of the neutrons being reflected toward the sample position. Next is the rotation of the sample itself, which can be rotated to choose a specific reflection within the sample that the neutrons will scatter off, finally the analyzer

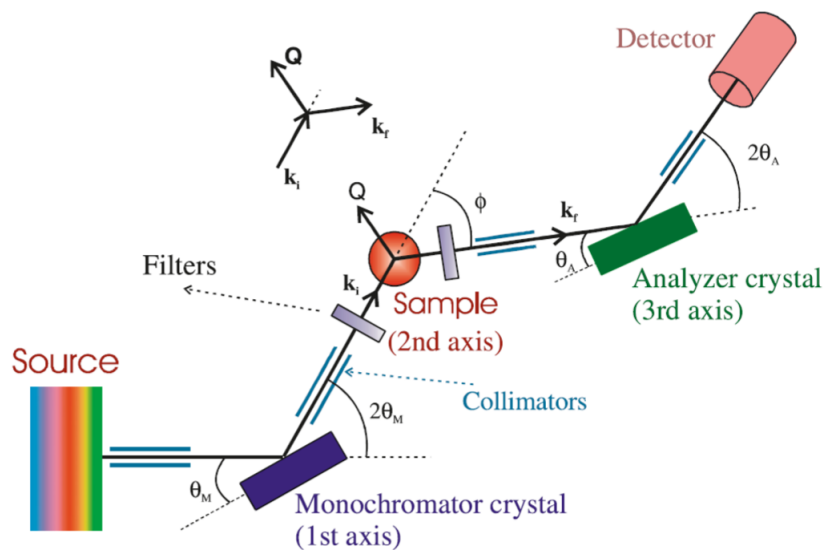


Figure 3.5: Sketch of a triple axis spectrometer. The white beam from the source is Bragg reflected off of the monochromator crystal to select the incoming energy of the neutrons. The rotation of the monochromator constitute the first axis of rotation. The reflected beam can be adjusted by various inserts like a filter and collimator before interacting with the sample itself. The rotation of the sample is the 2nd axis of rotation. The neutrons reflected from the sample can then pass through additional inserts before the final energy of the neutrons are selected by the analyzer crystal by rotating this about the third and final axis. Finally the neutrons are detected. Figure from [38]

crystal, which is essentially similar to the monochromator crystal but named differently to distinguish the two, can be rotated to once again select a specific wavelength to be Bragg reflected into the detector.

A Triple axis spectrometer is usually described with 6 angles, angles A1, A3, and A5 describe the angle of rotation of the monochromater, sample and analyzer respectively, while angle A2 is the angle between the incoming white beam and the reflected beam of off the monochromater, A4 is the angle between the beam coming from the monochromater and then the beam reflected by the sample toward the analyzer, finally A6 is the angle between the incoming beam from the sample toward the analyzer and the outgoing beam reflected toward the detector.

Both filters, collimators, and slits can usually be placed on both the incoming and outgoing beam to and from the sample position. The addition of the analyzer crystal is what sets a Triple Axis Spectrometer apart from a two axis one. In a two axis spectrometer there is no analyzer crystal and thus the detector integrates over all energies coming from the sample. This greatly increases the number of neutrons measured in the experiment and is therefore an excellent method to measure nuclear and magnetic structures. The trade off is then of course that you can no longer know the final energies of the neutrons scattered from the sample, therefore measurements of the dynamics are no longer possible.

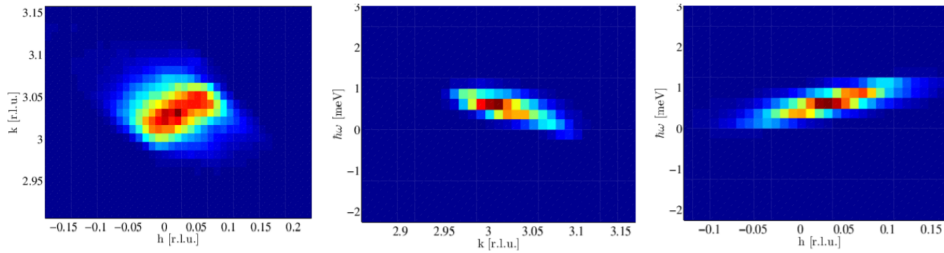


Figure 3.6: Resolution ellipsoids of h-YMnO₃ measured on the thermal TAS instrument EIGER at the $(hkl) = (030)$ Bragg reflection. Figure from [10].

Both elastic and inelastic measurements can be done with TAS instruments. To do elastic scattering the incoming and final energy is kept the same such that $E_i = E_f$ while scanning q , in this way only neutrons where the energy transfer $\hbar\omega = 0$ should reach the detector. Inelastic scans are usually then done by keeping the final energy and q constant, while scanning the incoming energy. One can choose to scan the final energy instead of the incoming, but the advantage of scanning the incoming energy is that you do not have to account for the factor $\frac{k_f}{K_i}$ in the partial differential scattering cross section see equation 3.3.27.

3.5.2 Instrument resolution

An instruments resolution is dictated by several factors. For a TAS experiment the following factors play a role. The path of the neutrons in the white beam from the moderator will never be perfectly parallel, as such neutrons will hit at slightly different angles, and thus a distribution of energies will be scattered from the monochromator. The monochromator itself is never completely perfect, due to imperfections and the mosaicity of the crystal itself a single wavelength will never be perfectly selected, see section 3.6. The same applies to the analyzer crystal after the sample. The finite physical size of the sample and detectors, which can never be infinitely small ensures that neutrons with slightly different \mathbf{q} will be counted in the same detector. All this means that any instrument will have a resolution function, which will be some distribution. Often the resolution function is a Gaussian, but it is not necessarily so.

The resolution function of a given instrument can be found by measuring the broadening of a Bragg peak at very low temperatures. The resolution of a TAS is usually an ellipsoid in four dimensions, three reciprocal space dimensions, (hkl) , and one with energy transfer $\hbar\omega$. For an example on the left plot in figure 3.6 a Bragg peak is measured on h-YMnO₃ in the h - k -plane. While the middle and right figure are the same peak but with k and h versus energy transfer $\hbar\omega$ respectively. The resolution ellipsoid of q versus energy is usually tilted to one side as is evident in the middle and right plots of figure 3.6. As such a better resolution can be obtained by measuring on the side of the dispersion where the direction of the elongation of the resolution ellipsoid matches the direction of the dispersion, which will yield a more well narrow energy resolution. See figure

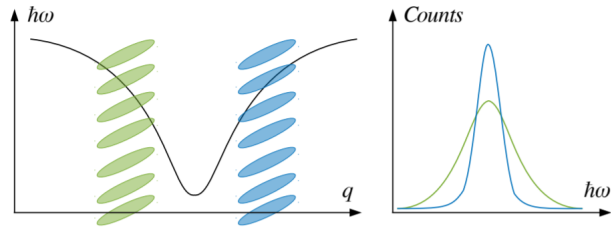


Figure 3.7: The left figure illustrates the dispersion relation and the resolution ellipsoid of the instrument, if the measurement is done to the left the resolution ellipsoid (green) overlaps the dispersion relation in a larger range of energy transfers, while if it is done on the right the ellipsoids (blue) only overlaps the dispersion in a much more narrow range of energy transfers. The right figure illustrates the intensity one would measure as a function of energy transfer and it is clear that the energy resolution is much better in the blue case. Figure from [10].

3.7. The q -resolution is determined by the angular resolution of the scattering angle and thus depends mainly on how well collimated the beam is both before and after the sample.

3.5.3 RITA-II

The experiments in this thesis were done on the cold neutron triple axis spectrometer, RITA-II, situated at the SINQ neutron spallation source at PSI in Switzerland. A sketch of RITA-II can be seen in figure 3.8. The neutrons for RITA-II comes from a cold moderator of liquid Deuterium, these are fed into a 42 m long curved guide system at the end of which sits the monochromator of RITA-II. The vertically focused pyrolytic graphite (PG) monochromator crystal can select neutrons within the energy range of 2.5meV-20meV. The flux at the sample is on the order of $\sim 10^6$ neutrons/second. However both the flux and the resolution depends on the wavelength used. The resolution improves as the wavelength is increased. Be and BeO filters can be inserted if desired both before and after the sample, which will remove higher order neutrons.

The analyzer on RITA-II is rather unique. The analyzer consists of 9 blades of PG crystal, which can be individually turned to reflect a unique wavelength towards a detector. This allows one to make 9 simultaneous measurements of $(\mathbf{q}, \hbar\omega)$. Finally the detector is a position sensitive ^3He -detector.

I took part in several experiments with h-YMnO_3 on RITA-II and on the thermal TAS instrument EIGER, also located at PSI, in the period 2014-2016. The data analyzed in this thesis however came from an earlier period of experiments conducted at RITA-II in 2012.

3.6 Line Forms

When making a theoretical scattering experiment on an infinite crystal, all Bragg-peaks are δ -functions. However in reality several factors limit the validity of this assumption. First the size of the crystal is relevant, for small

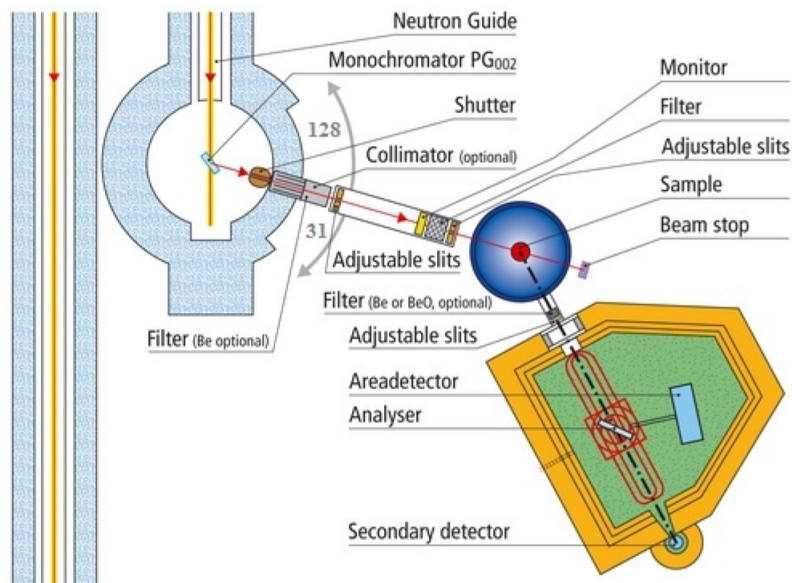


Figure 3.8: Sketch of the RITA-II instrument at PSI, Switzerland. Figure from [28]

crystals the finite size of the crystal allows for scattering when the Laue condition, 3.3.19, is not met. Since no crystal is infinite, this always play some role, however the relevance of this decreases as the size of the crystal is increased. For experiments with dimensions of millimeters or larger, one can fairly safely assume that the Laue condition is satisfied for almost all scattering within the crystal, and as such one can keep the assumption that scattering is δ -functions.

Almost no crystal of this size is a true single crystal though as these are notoriously difficult to manufacture, the exception to this is of course the semiconductor industry that have managed to produce extremely pure silicon single crystals in the length of meters and with a weight of hundreds of kilograms, but for almost all other crystals of fairly large sizes the crystal will be made up of smaller crystallites that are oriented in slightly different directions. This gives rise to the mosaicity of the crystal that is a measure of the difference in orientation of the different crystallites within the larger crystal. The mosaicity of the crystal also plays a role in the line form measured from a crystal, but its contribution is small if the variance of the crystallite orientations are small.

One factor that always impacts a measurement is the resolution function of an instrument. Any signal in the sample will always be broadened by the resolution function of the measurement. The measured signal can be determined from the true signal and the resolution function of the instrument by doing a convolution. The convolution of the theoretical line form $L(x)$ and the Resolution

function $R(x)$ of the instrument is

$$L(x) * R(x) = \int_{-\infty}^{\infty} L(y)R(x - y)dy \quad (3.6.1)$$

Convolutions follow several mathematical rules. In the following the distributions f , g , and h are all line forms of the same variable t . Convolutions are commutative, such that

$$f(t) * g(t) = \int_{-\infty}^{\infty} f(\tau)g(t - \tau)d\tau = \int_{-\infty}^{\infty} g(u)f(t - u)du = g(t) * f(t) \quad (3.6.2)$$

where a simple substitution of integration variable $u = t - \tau$ yields the result. Convolutions are also associative

$$f * (g * h) = (f * g) * h \quad (3.6.3)$$

and distributive

$$f * (g + h) = f * g + f * h. \quad (3.6.4)$$

A very important identity is the convolution of a function with the delta function simply gives the function

$$f * \delta = f. \quad (3.6.5)$$

From this it immediately follows that if you can assume your signal to be a delta function, the resolution function is simple whatever line form you measure. As such the resolution function can be determined by measuring a Bragg peak in a sufficiently large crystal, and that is how the resolution is measured as in figure 3.6.

As previously stated the resolution function is usually a simple Gaussian function, however on RITA-II a small Lorentzian contribution exists. In this thesis it is of great concern to get an as good resolution function as possible, as such both the Gaussian and the Lorentzian part of the resolution function must be included in the analysis. Therefore a good approximation of the true resolution function is the convolution of a Gaussian, $G(x)$, distribution function and a Lorentzian, $L(x)$, which is called a Voigt function, $V(x)$, defined as

$$V(x) = G(x) * L(x). \quad (3.6.6)$$

The Voigt function does not have an analytical expression, but can be handled by most modern fitting routines, such as those used by Spec1D for Matlab.

Close to the Néel temperature, critical scattering will begin to be part of the signal. Critical scattering is seen as a Lorentzian contribution, see section 3.3.6, and this signal will also be convolved by the instrument resolution function, leading to an expression of the form

$$Critical(\mathbf{q}) = L_{cri}(\mathbf{q}) * V_{res}(\mathbf{q}) \quad (3.6.7)$$

Where the subscripts *cri* and *res* represents the contribution from the critical scattering and the resolution function respectively. Using the definition of the

Voigt function in equation 3.6.6 and the fact that convolutions are both commutative and associative the following expression can be found for the critical scattering

$$L_{cri}(\mathbf{q}) * V_{res}(\mathbf{q}) = L_{cri}(\mathbf{q}) * (G_{res}(\mathbf{q}) * L_{res}(\mathbf{q})) = G_{res}(\mathbf{q}) * (L_{cri}(\mathbf{q}) * L_{res}(\mathbf{q})) \quad (3.6.8)$$

To evaluate this expression the convolution of two Lorentzian distributions is needed. Fortunately the convolution of a Lorentzian with another Lorentzian is just a new Lorentzian where the intensity is the product of the individual intensities, and the width is the sum of the widths of the two convoluted Lorentzians [39]. As such the above equation becomes

$$G_{res}(\mathbf{q}) * (L_{cri}(\mathbf{q}) * L_{res}(\mathbf{q})) = G_{res}(\mathbf{q}) * L_{conv}(\mathbf{q}) \quad (3.6.9)$$

where $L_{conv}(\mathbf{q})$ is the new Lorentzian stemming from the convolution of the critical scattering signal and the Lorentzian part of the resolution function.

This means that the measured signal with critical scattering is once again just the convolution of a Gaussian and a Lorentzian

$$G_{res}(\mathbf{q}) * L_{conv}(\mathbf{q}) = V_{final}(\mathbf{q}) \quad (3.6.10)$$

where the width of the Lorentzian part of this Voigt function is the sum of widths of the critical scattering and the Lorentzian part of the resolution function.

3.7 Introduction to YMnO₃

The most studied of the rare earth manganites is YMnO₃. In this thesis the focus is on hexagonal *h*-YMnO₃. Below the Néel temperature, T_N , *h*-YMnO₃ transitions from a paramagnet to a spin 2 ($S = 2$) antiferromagnet, where the Mn³⁺ ions have the quantum numbers $S = 2$ and $L = 2$, however due to quenching L is not a good quantum number and as such the Mn³⁺ ions in *h*-YMnO₃ just become $J = S = 2$, see section 2.2.1. *h*-YMnO₃ has a ferroelectric ordering at a temperature of 1258K [40], while the magnetic phase transition happens at a much lower temperature of roughly 72K [41, 42, 3]. The temperature of the magnetic phase transition is however heavily debated in the literature. Some report the magnetic transition temperatures to be as low as 69.9K [43], where others are as high as 74-75K [44, 45].

The unit cell of *h*-YMnO₃ consists of two layers of manganese ions stacked on top of each other, with Yttrium and oxygen filling the void between the layers, see figure 3.9 left. The magnetic structure of *h*-YMnO₃ is formed of triangles of the magnetic manganese ($S = 2$) ions with 120 degrees between the spins in the $a - b$ plane, which are then stacked in the c -direction. The exact magnetic structure have been a subject of considerable debate, but the study by Holm-Dahlin et al. confirmed the magnetic structure to be $P6'_3cm'$, see figure 3.9 right.

Holm-Dahlin et al. [46] show that the magnetic interactions in *h*-YMnO₃ are mainly an Heisenberg nearest-neighbor exchange interaction with $J = -2.4$ meV, the second most relevant term, although much weaker, is an easy-plane anisotropy of strength $D = 0.32$ meV and lastly an even weaker ferromagnetic interlayer exchange of strength $J_z = 0.151$ meV. That means that *h*-YMnO₃ are

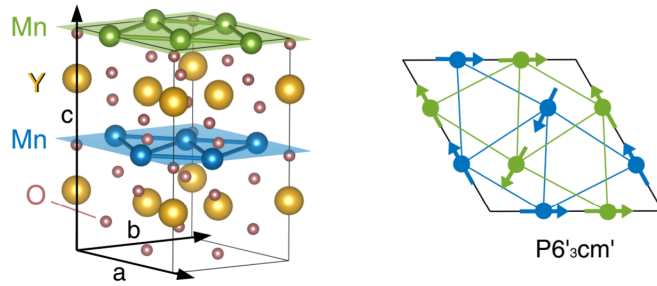


Figure 3.9: *Left: The unit cell of $h\text{-YMnO}_3$ with stacked layers of manganese ions with Yttrium and oxygen in between. Right: The best candidate for the magnetic structure of $h\text{-YMnO}_3$. Figure from [3]*

described well as a 2-dimensional triangular lattice Heisenberg antiferromagnet with a small easy-plane anisotropy.

Because of the hexagonal lattice of $h\text{-YMnO}_3$ and the antiferromagnetic interaction between the spins, they also become frustrated meaning the spins have difficulty ordering even below the Néel temperature, see section 2.2.4. The Curie-Weiss temperature of $h\text{-YMnO}_3$ is $\theta_{CW} = -500K$ [45] yielding a rather large frustration index f , as defined in equation 2.2.22, between roughly 6.7 and 7.1. depending on the Néel temperature one uses from literature.

In addition to being a frustrated antiferromagnetic system $h\text{-YMnO}_3$ is also multiferroic with couplings between the magnetic, electric, and elastic order parameters. The much higher ferroelectric ordering temperature compared to that of the magnetic ordering means that $h\text{-YMnO}_3$ is a type-I multiferroic.

The excitations of $h\text{-YMnO}_3$ have been studied as well, the phonon and magnon dispersions were measured and calculated by Holm et al [46] and can be seen in figure 3.10 where the measured data are in the top row, while the corresponding theoretical models are shown in the bottom row. Their data show a phonon-magnon interaction due to an avoided crossing at the K point in inserts d and h. they also show that the upper magnetic mode is degenerate and splits into two modes with an applied field as seen when comparing inserts b and c as well as f and g.

The recent study by Holm-Dahlin et al [3] on the same data as used in this thesis investigates the magnetic phase transition temperature as well as how the excitation energy of the magnon depends on the temperature of the sample. They also determine the value of the relevant critical exponent β associated with the magnetic phase transition and show that the temperature dependence of the excitation energy of the lower magnon also follow a power law with a critical exponent β' which they show to be reasonably equivalent with β within the uncertainty.

A number of experimental results of the Néel temperature of $h\text{-YMnO}_3$ and relevant critical exponents have been summarized in table 3.1. The table also includes the theoretical values of the same critical exponents in various models.

There have been considerable difficulty in locking down a specific universality

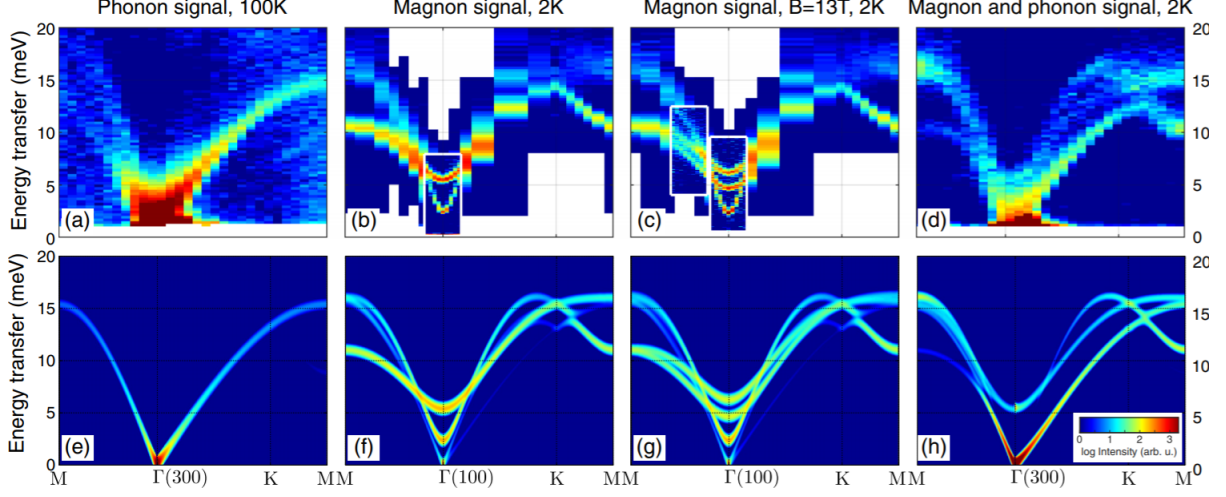


Figure 3.10: *Left: plot a-d show the measured dispersion relations of h - $YMnO_3$, a shows the phonon dispersion at $\mathbf{q} = (300)$ while b and c show the magnon dispersion at $\mathbf{q} = (300)$ with b being with 0 applied field and c being with an applied field of 13T clearly showing that the upper mode is degenerate and splits into two separate modes with an applied field. d then shows both the magnon and the phonon dispersions at $\mathbf{q} = (300)$. Right: The best candidate for the magnetic structure of h - $YMnO_3$. Figure from [46].*

Table 3.1: Table of relevant critical exponents for this thesis. β is the critical exponent for the magnetization \mathbf{M} , γ is the critical exponent for the magnetic susceptibility, and ν is the critical exponent for the magnetic correlation length [13]. The table also include the value of the Néel temperature T_N found by other studies.

theoretical models	T_N [K]	β	γ	ν
2D 3d XY		0.345	1.316	0.669
1D 3d Ising		0.326	1.2378	0.6312
1D 2d Ising		0.125	1.75	1
3D 3d Heisenberg		0.367	1.388	0.707
Mean Field		0.5	1	0.5
Experiments				
Holm-Dahlin et al. [3] (elastic)	72.11 ± 0.05	0.206 ± 0.003	-	-
Holm-Dahlin et al. [3] (inelastic)	72.4 ± 0.3	0.24 ± 0.02	-	-
Chatterji et al. [30]	69.89 ± 0.05	0.295	0.97	0.45
Roessli et al. [41]	72.1 ± 0.05	0.187	-	0.57
Kawamura [47]		0.25	1.1	0.53



Figure 3.11: *Picture of the sample mounted on its aluminium holder.*

class of h -YMnO₃. as evident from table 3.1 none of the studies cited here match the critical exponents of any of the theoretical universality classes well. It has been proposed [3, 41, 47] that triangular frustrated systems could have a completely new universality class.

3.8 Experimental Setup

3.8.1 The sample

The sample used is of hexagonal yttrium-manganite with a small doping of 2% Europium $h - (\text{Y}_{0.98} \text{Eu}_{0.02}) \text{MnO}_3$. The Europium doping was discovered after the experiments had been conducted, however a doping this small is not expected to have any significant influence on the sample, which should behave almost exactly as pure h -YMnO₃ [48][49]. Because this small Europium doping is expected to be negligible the sample will continue to be referenced as just h -YMnO₃ throughout this thesis. The sample is a rod with a total mass of 5.25 g mounted with glue on an aluminum holder, see figure 3.11. The sample quality is in general of good quality with a single phase and limited mosaicity. The quality of the samples were assessed using X-ray and neutron Laue diffraction spectroscopy by Sonja Holm-Dahlin for her PhD used on the same sample [10]. The most recent study where the lattice parameters were determined on the sample used in this work are by Holm-Dahlin et al. [3] and the lattice parameters of this sample of h -YMnO₃ are $a = b = 6.108 \text{ \AA}$ and $c = 11.39 \text{ \AA}$.

3.8.2 Measurements

Elastic measurements were done at the RITA-II instrument at PSI, see section 3.5.3, using the monochromatic three-axis imaging mode with a constant incoming and final energy of 5.0 meV [50]. A beryllium filter were placed on the outgoing side, while the collimations were 80' incoming and the imaging mode of RITA-II gives the instrument a natural outgoing collimation of 40'. The scans were done in the Across the magnetic Bragg peak at $\mathbf{q} = (0\bar{1}0)$.

For the inelastic measurements the setup was very similar, except of course

that the incoming energy of the neutrons were varied, while the final energy were fixed at 5.0 meV. This gives an energy resolution of about 0.2 – 0.3 meV and a resolution in \mathbf{q} -space of 0.015 r.l.u.. [51]. The energy scans were done at constant $\mathbf{q} = (100)$.

In all measurements an orange ILL-type 1.5 K cryostat was used to control the temperature of the sample.

Chapter 4

Experimental Results

This section details the measurements and the analysis of the data on h -YMnO₃. The sample used contains a 2% europium doping, but as stated in section 3.8 this is not expected to have any influence on the data, as such the sample will be referred to as simply h -YMnO₃.

This section is split into three subsections, the first two details the results of the elastic and inelastic neutron scattering measurements respectively, while the third one contains a recap of these results, and some calculations of other critical exponents based on the measured critical exponents from the experiments.

4.1 Results of the Elastic Measurements

In this section the results from the elastic neutron scattering measurements at the magnetic Bragg peak at $\mathbf{q} = (0\bar{1}0)$ will be explained. Much of the analysis is to determine the correct fitting function for the data at low temperatures to find a well suited instrument resolution function. Having a good description of the instrument resolution function allows the critical scattering close to the Néel temperature, T_N , to be found as the additional scattering occurring close to the magnetic phase transition. Both T_N and the critical exponents, β , γ , and ν , associated with the critical phase transition are found. The introduction to T_N and the critical exponents can be found in section 2. In addition a discussion about some of the choices one needs to make during this type of analysis is included.

4.1.1 Fitting the line forms

Several line forms are used for fitting data in this section. For an introduction to the line forms used see section 3.6.

4.1.2 The instrument resolution function

First the instrument resolution function need to be determined. To do this longitudinal scans were made across a magnetic Bragg peak located at $\mathbf{q} = (0\bar{1}0)$ at low temperatures, and fitted to an appropriate resolution function. Critical scattering will start to be a relevant factor at higher temperatures close to the Néel temperature. Therefore only data points significantly lower than T_N would

Table 4.1: Table of reduced χ^2 values for the Voigt, Gaussian, and Lorentzian resolution functions at low temperatures

Temperature [K]	Voigt reduced χ^2	Gaussian reduced χ^2	Lorentzian reduced χ^2
1.5	1.86	2.27	248
1.7	1.42	2.16	240
2.0	1.68	2.38	247
3.0	1.78	2.22	243
4.0	1.24	1.97	236
5.0	1.26	2.09	242
5.0	1.25	2.02	231
6.0	1.26	2.09	241
7.0	1.73	1.91	251
8.0	2.04	2.49	247
9.0	1.36	2.23	235
10.0	1.51	2.21	251
10.0	1.38	2.21	232
15.0	1.69	2.19	239
20.0	1.63	2.22	233
25.0	1.06	1.89	226
30.1	1.33	2.06	221
35.1	1.29	2.11	219
37.0	1.22	1.97	217
39.0	1.41	2.03	229

be used to determine the instrument resolution function. Previous work suggest that $T_N \approx 70\text{K}$, therefore only temperatures in the range $[0\text{K}; 40\text{K}]$ would be used for this, yielding 20 data points to determine a proper resolution function.

Several instrument resolution functions were considered for use in this thesis. Namely the Gaussian function, the Lorentzian function, and the convolution of the two, the Voigt function. All three types of possible resolution functions were fitted to data and compared to get the best fit, see figure 4.1 for six examples of resolution function fits at different temperatures, figure 4.2 shows the same data and fits, but with a logarithmic y-scale. Both the χ^2 value and visual inspection were used to determine the quality of the fits.

The Lorentzian function fits the data quite poorly, while both the Gaussian and Voigt does it quite well. From the non logarithmic plots it can be seen that the Gaussian consistently does not fit the top of the peak well, while the Voigt does a much better job at this. In addition there seems to be a small broad tails on either side as can be clearly seen in the logarithmic plots. The Voigt function catches some of the scattering in these tails.

The Voigt function appears visually to be a superior resolution function compared to both the Gaussian and especially the Lorentzian. This is also confirmed by the reduced χ^2 values for the different functions, which can be seen in table 4.1. The reduced χ^2 is closer to one for the Voigt compared to the Gaussian in all cases, while the value for the Lorentzian is much bigger.

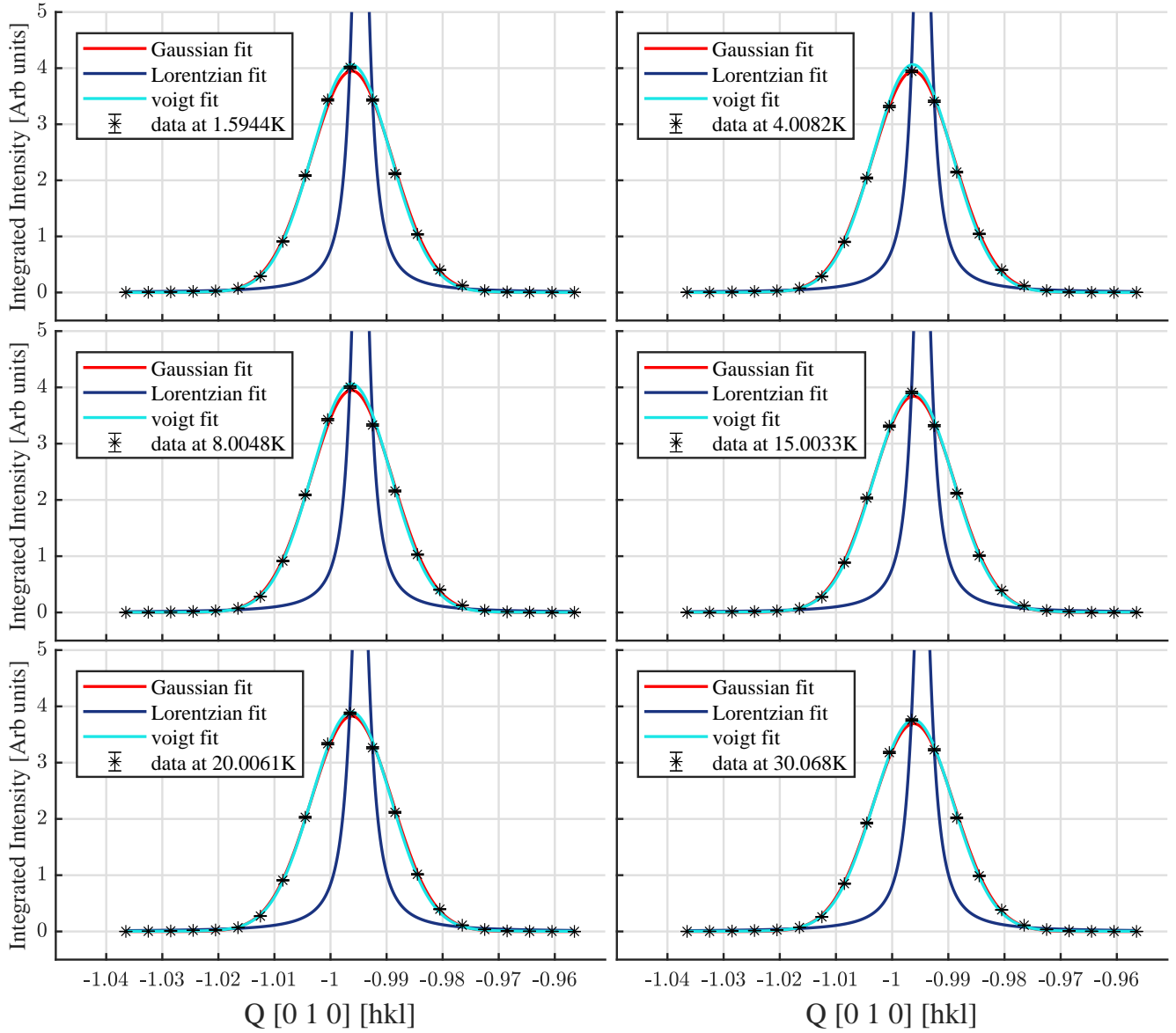


Figure 4.1: Scans of YMnO₃ across the magnetic Bragg peak at $\mathbf{q} = (0\bar{1}0)$ at low temperatures. The data represents the scattering of the magnetic Bragg peak convoluted by the resolution function of the instrument. At low temperatures the Bragg peak is assumed to be a delta function, the measured signal is therefore just the resolution function. Three different line forms were fitted to the data to determine the best model for the resolution function, the Lorentzian (dark blue), Gaussian (red), and the Voigt function (cyan).

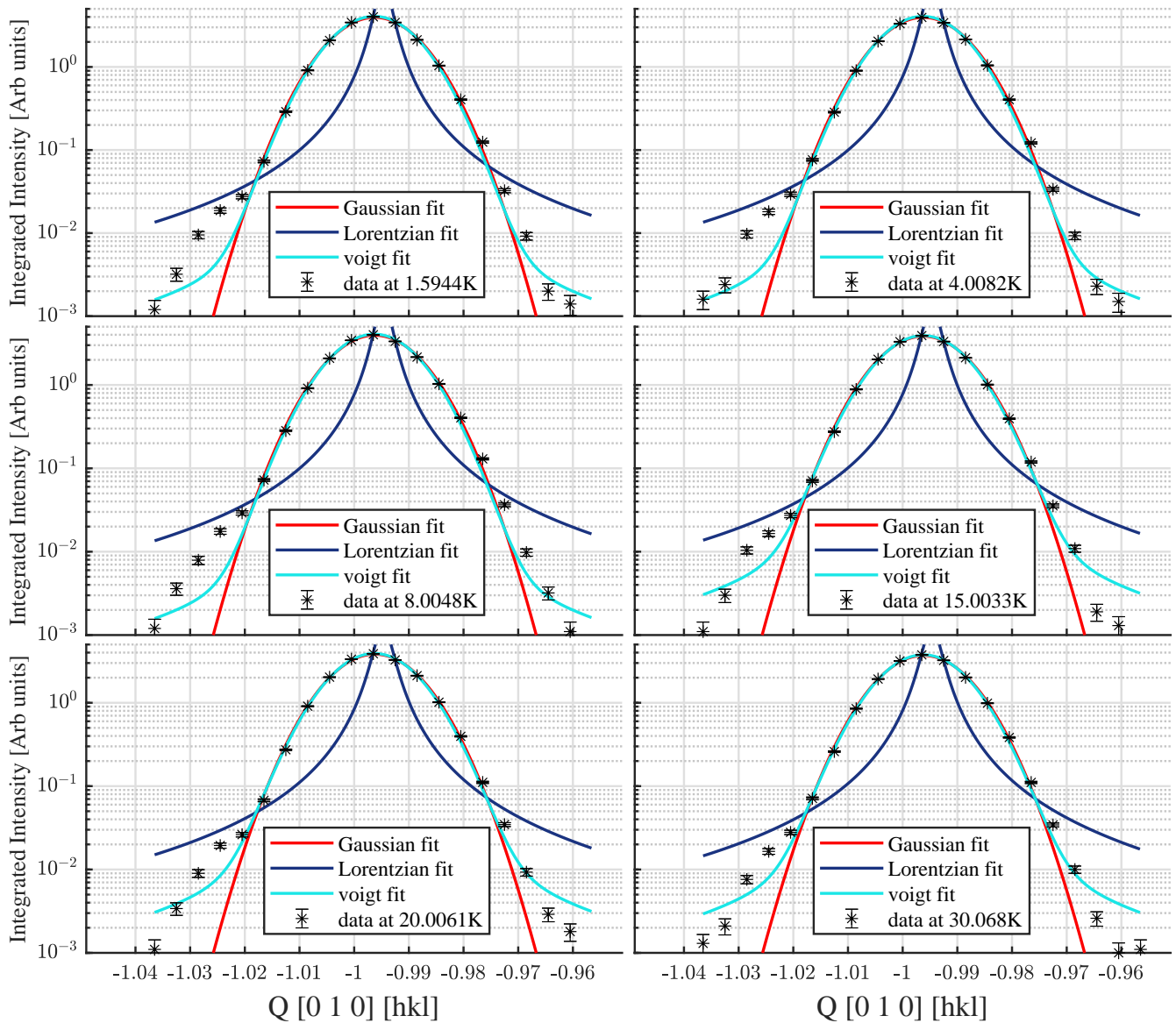


Figure 4.2: Same data and fits as in figure 4.1, but with a logarithmic y-scale. These plots clearly reveal that there is some small, but broad tail in the resolution function of RITA-II. The logarithmic plots confirm that the Gaussian (red), Voigt (cyan) fits are indeed superior to the Lorentzian (dark blue). In addition, while far from perfect, the Voigt does at least catch some of the broadening at the tails of the peak, thus indicating that it is superior to the Gaussian.

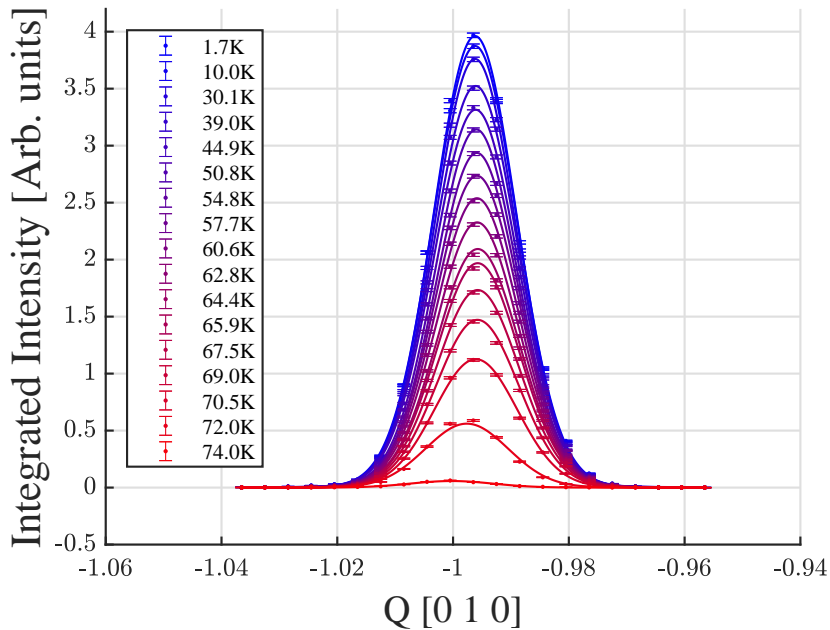


Figure 4.3: *Longitudinal scans of $YMnO_3$ across the magnetic Bragg peak at $\mathbf{q} = (0\bar{1}0)$ at various temperatures from base to just above the Néel temperature $T_N \approx 72K$. Single Voigt profiles have been fitted to all data.*

The Voigt function clearly outperforms the other candidates both with respect to the reduced χ^2 in addition to being visually better. As such the Voigt function was chosen as the instrument resolution function for this thesis.

The parameters of the instrument resolution function was determined as the average width of the Gaussian part and the average width of the Lorentzian part of the Voigt function. The remaining data points at higher temperatures were fitted to Voigt profiles with the Gaussian and Lorentzian widths locked to the values found at low temperatures, while the intensity, center and background were free parameters. Examples of Voigt profiles at various temperatures can be seen in figure 4.3 where data taken at lower temperatures are in blue, and higher temperatures are in red.

4.1.3 Fitting the critical scattering

To fit the critical exponent, β , of the power law relation between the magnetization and the temperature, the critical region must be determined, see section 2.5.2. In the critical region the relationship between M and T is a power law, which will look linear when plotted on double logarithmic axes. One method is to make an initial guess of T_N , and then plot the reduced temperature $\frac{T_N - T}{T_N}$ versus the intensity. A good guess of T_N will give a long range of values where there is a power law relation and thus a long range which looks linear on double logarithmic axes, a bad guess on the other hand will give a shorter range. Several plots have been made starting from a guess of $T_N = 71.1K$ in increments of 0.2K, see figure 4.4, enough plots were made to be sure that the maximum

linear range (red data points) was found.

From these plots it was determined that a guess of $T_N = 71.5\text{K}$ was the best initial approximation of the Néel temperature because it had the longest linear range, spanning from 53.8K to 70.0K while both lower and higher guesses of T_N gave shorter ranges. The range of temperatures from 53.8K to 70.0K is then the range in which there is a power law relation between the magnetization and the temperature. The data in this range were fitted to the following power law based on equation 2.5.20

$$I = I_{bkg} + I_0 \left(\frac{T_N - T}{T_N} \right)^{2\beta} \quad (4.1.1)$$

where I is the integrated intensity of the $\mathbf{q} = (0\bar{1}0)$ reflection, I_{bkg} is the background intensity coming from the nuclear contribution to the scattering, I_0 is the intensity, while both T_N and 2β were free parameters in this fit. This result can be seen in figure 4.5 where the red data points were fitted to a power law. A Néel temperature of $T_N = 71.53 \pm 0.05$ and the critical exponent $\beta = 0.179 \pm 0.002$ were found. Evidently as the temperature approaches T_N the relationship between the scattering intensity and the temperature is no longer described by a power law due to critical scattering happening in this temperature region. Critical scattering causes Lorentzian Broadening of the signal close to T_N , see section 3.3.6, this scattering can be fitted by a Lorentzian function convoluted by the resolution function, the convolution of a Voigt function with a Lorentzian yields just another Voigt function where the width of the Lorentzian contribution is just the sum of the two Lorentzian Widths, see section 3.6. In the region where critical scattering occurs there might still be some contribution from the magnetic scattering, in order to fit the critical scattering two Voigts were used, one for the magnetic scattering where the Gaussian and the Lorentzian width were locked by the resolution function, and then one for the critical scattering where only the Gaussian width were locked from the resolution function, but where the Lorentzian width was allowed to be larger than the Lorentzian width of the resolution function, since the critical scattering should broaden the signal.

This yielded figure 4.6 where the total fit of the magnetic and critical scattering give the blue fit, while the magnetic scattering contribution is given in cyan and the critical scattering contribution is given in red.

4.1.4 The Néel temperature and critical exponents

By removing the critical scattering and using only the magnetic part of the fit from figure 4.6, it is possible to extend the power law fit with equation 4.1.1 from figure 4.5 all the way to T_N . This can be seen in figure 4.7. The uncertainties close to T_N become rather large. The widths of the scattering from the Bragg peak and the critical scattering are very comparable very close to T_N , which means the fitting routine has a hard time distinguishing between the two very close to the Néel temperature, yielding higher uncertainties very close to the phase transition.

Separating the scattering into the magnetic signal and the critical scattering signal only gave a small adjustment to the value of the Néel temperature and β . A value of $T_N = 71.48 \pm 0.02\text{K}$ is in general agreement with other publications which gives finds T_N to be in the range of roughly 70 – 75K, see table 4.2.

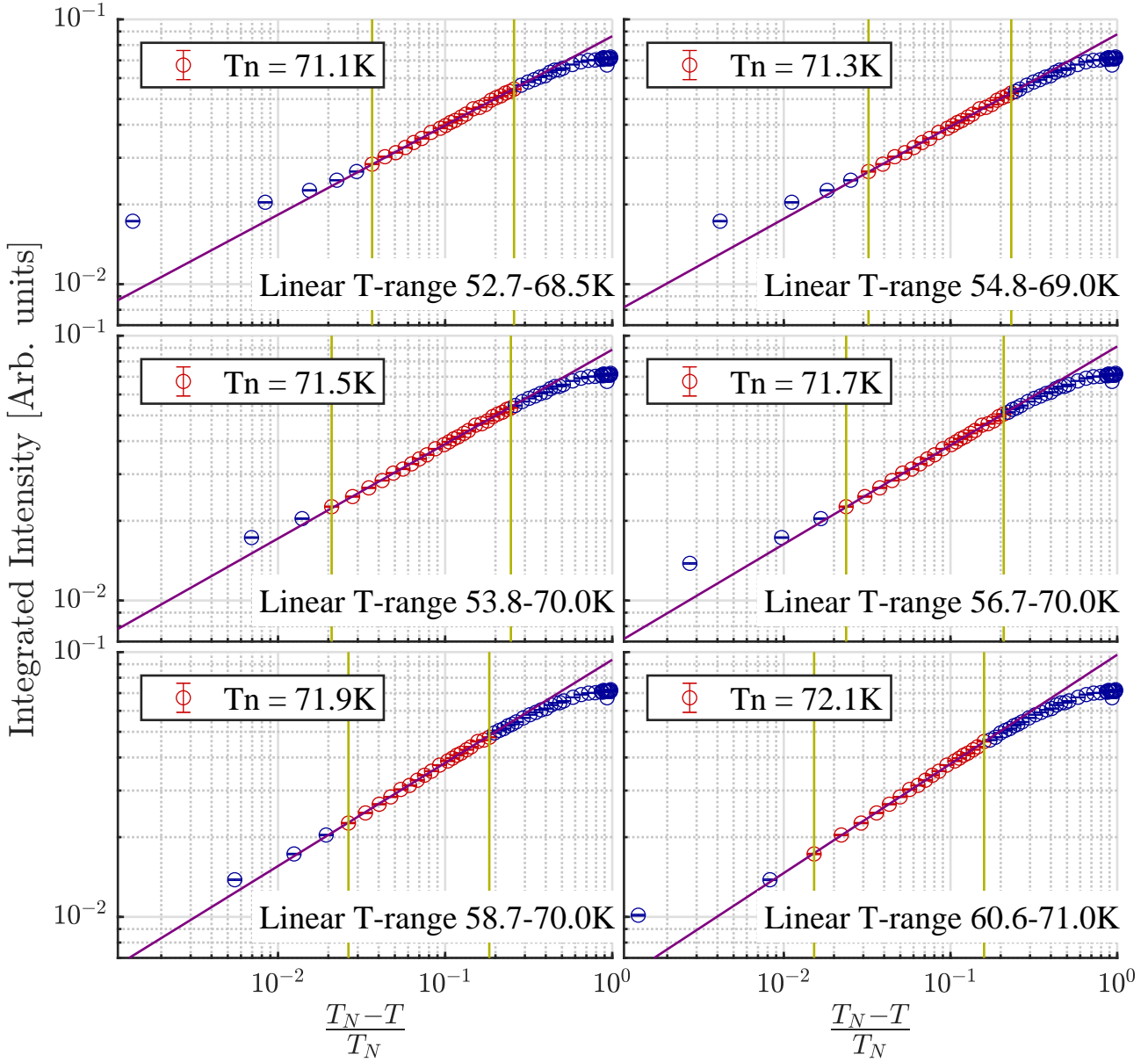


Figure 4.4: Double logarithmic plots of the reduced temperature $\frac{T_N - T}{T_N}$ versus the integrated intensity for various assumed values of the Néel temperature T_N . The part of the data that has a power law relation will look linear when plotted with double logarithmic axes. The closer the assumed value of T_N is to the true value the larger range of temperatures will look linear.

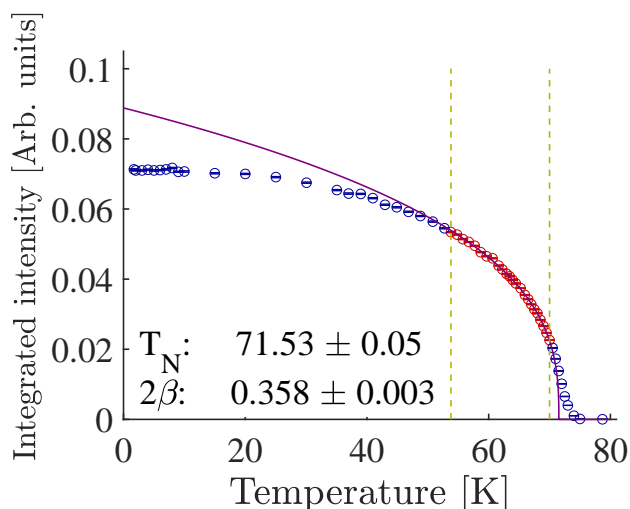


Figure 4.5: *The integrated intensity of the scattering versus the temperature. The optimal fitting range determined from the plots in figure 4.4 are bounded by the two vertical lines, outside of these data points in blue represent data that were not included in the fit. A power law, equation 4.1.1, have been fitted to the red data points with the purple line showing the fit. The fit finds the values of $T_N = 71.53 \pm 0.05$ and $\beta = 0.179 \pm 0.002$.*

The critical exponents are all fitted to the power law relations detailed in section 2.5.2.

The value of $\beta = 0.179 \pm 0.002$ is quite close to the value found by Roessli et al [41] and fairly close to Holm-Dahlin et al [3], but quite far from the value found by e.g. Chatterji [30]. It also differs from the value predicted by various models, coming closest to that predicted by a 1D 2d Ising model, which gives $\beta = 0.125$, which is still far away from the result found in this work.

An estimate of the critical exponent γ can be determined by fitting the intensity of the critical scattering to a power law based on 2.5.22

$$I_{Critical} = A \left(\frac{T_N - T}{T_N} \right)^{-\gamma} \quad (4.1.2)$$

where A is the amplitude of the critical scattering. The critical scattering below and above T_N from figure 4.6 were fitted to the power law in equation 4.1.2. This is done in figure 4.8. where the data points and fit in yellow is the critical scattering below T_N which yielded $\gamma = 1.12 \pm 0.02$ from the fit. The data points and fit in blue are the critical scattering above T_N where the fit gave $\gamma = 1.063 \pm 0.002$. This result is very close to the theoretical value of 1 found in a mean field model. And also in good agreement with the results of Chatterji [30] and Kawamura [47], which posted values of $\gamma = 0.97$ and 1.1 respectively. Finally the HWHM of the critical scattering were also fitted to a power law to get the critical exponent ν based on 2.5.21.

$$HWHM = A \left(\frac{T_N - T}{T_N} \right)^{\nu} \quad (4.1.3)$$

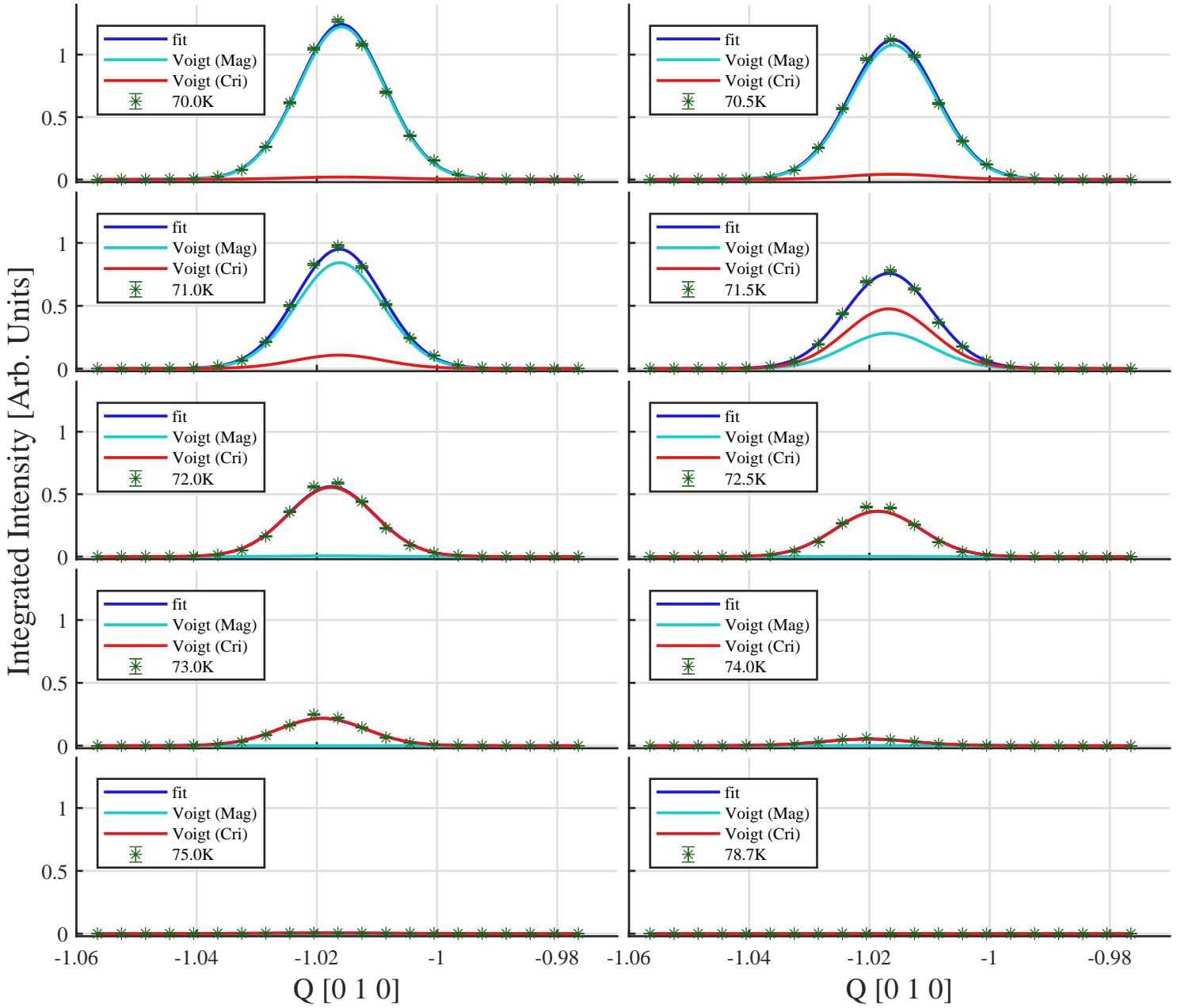


Figure 4.6: Longitudinal scans of $YMnO_3$ in the critical region. Both the magnetic Bragg peak (cyan) and the critical scattering (red) contributes to the measured scattering in this temperature region. To fit this two Voigt profiles have been fitted to all data, the sum of which is the blue fit line. The first one, in cyan, is the scattering from the magnetic Bragg peak which has both its Gaussian and Lorentzian widths locked by the instrument resolution function. The other from the critical scattering, in red, where the Lorentzian width were a free parameter, with the restriction that the fit had to find a width larger than that of the instrument resolution function.

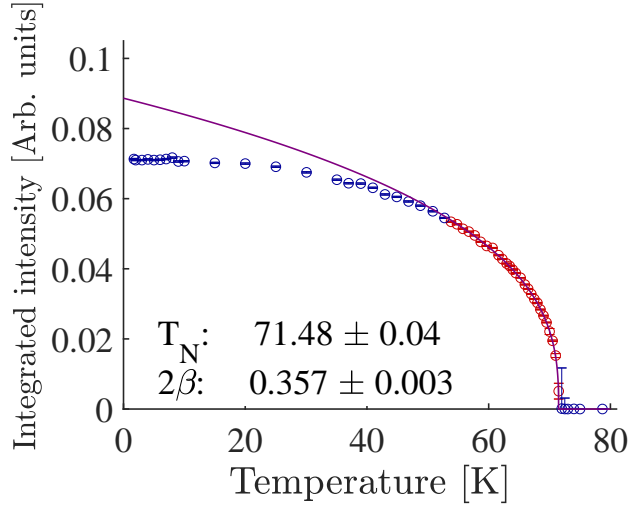


Figure 4.7: *The integrated intensity of the scattering from the magnetic Bragg peak versus temperature. The critical scattering close to T_N has been excluded from this fit, see figure 4.6, leaving only scattering from the Bragg peak. This is used to make a small correction to the fit from figure 4.5 where the temperature range which was fitted have been extended all the way to T_N . This changes the values found earlier to $T_N = 71.48 \pm 0.002K$ and $\beta = 0.179 \pm 0.002$.*

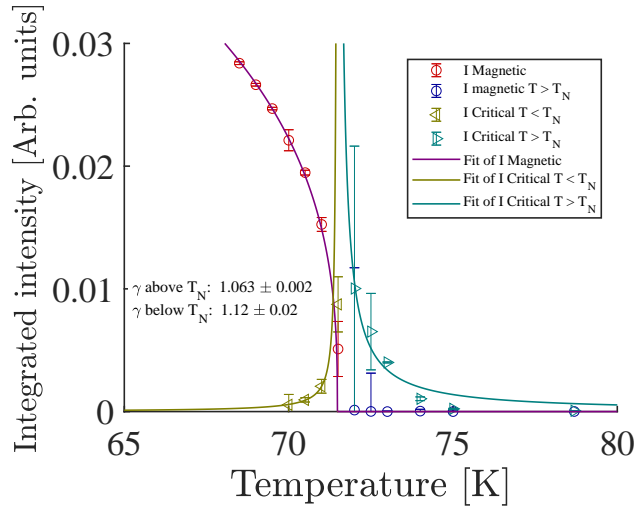


Figure 4.8: *Intensity of various contributions to the scattering versus temperature close to the Néel temperature. The red data points are the intensity of the scattering from the magnetic Bragg peak below T_N with a power law in purple fitted to it, see figure 4.7, while the blue data points are the intensity of the magnetic Bragg peak above T_N , all of which are 0. In addition to this, the critical scattering are included with points below T_N in yellow and above in cyan. A power law fit to both of these data ranges are included in the same color as the data points. The power law fit to the critical scattering below T_N gives $\gamma = 1.12 \pm 0.02$ while the power law fit to the critical scattering above T_N gives $\gamma = 1.063 \pm 0.002$.*

The fits of the HWHM above and below T_N can be seen in figure 4.9. The left figure shows the HWHM of the critical scattering below T_N , while the right shows the same for the critical scattering above T_N . The determined values of ν is 6.3 ± 0.2 for the data points below T_N , while $\nu = 4.1 \pm 1.0$ above T_N . Both of these values differ greatly from both the theoretical models and other published experimental results. These all give values of ν of 1 or less, see table 4.2 where as the ones found here both are quite higher than 1. The reason for this is not immediately clear, however a yet to be published paper by Janas et al [52] investigates the inelastic, but coherent, scattering in h -YMnO₃. They report persistent coherent inelastic scattering far beyond what you would expect the critical range to be on both sides of T_N . This they claim is due to the competing interactions within the system due to the fact that it is a geometrically frustrated system which causes a highly extended critical range. This additional scattering might influence the properties in some yet unknown way, but could maybe explain why the value of ν is so far from anything seen before. All these results are summarized in table 4.2.

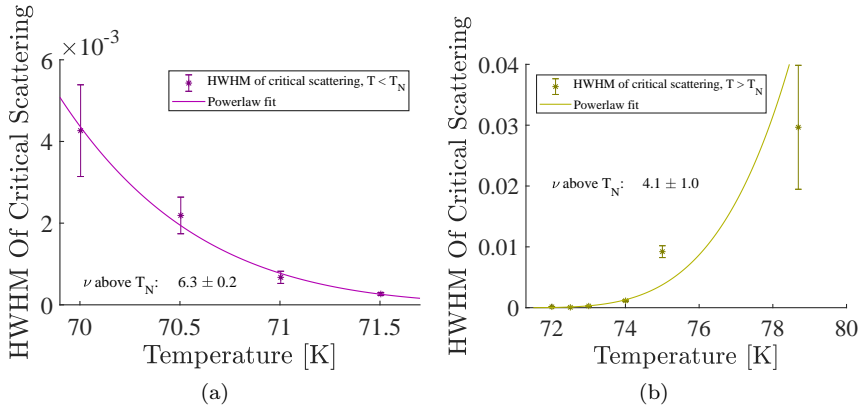


Figure 4.9: *The HWHM of the critical scattering fitted to power laws gives the critical exponent ν . On the left is the data below T_N which give a value of ν is 6.3 ± 0.2 . Right: HWHM of the critical scattering above T_N , which give $\nu = 4.1 \pm 1.0$*

4.1.5 Variational analysis of the temperature range used for fitting T_N and β

The method of plotting the intensity versus the reduced temperature on double logarithmic axes, as was done in figure 4.4, to determine the data range in which a power law can be fitted to get T_N and β is prone to human error and bias, as you have to make a choice on which data points are a part of the linear part and which are not. Some points might be included or omitted that should actually have been left out or used. The effects of including points or not can be investigated, by simply exploring the results one can obtain for T_N and β , by varying the highest and lowest temperature included in the power law fits.

To this end the plots in figure 4.10 were made. The color of the data points dictate the high end of the temperature range used for the power law fits, while

the x-axes show the low end of the temperature range used. The y-axes then show the found values of the Néel temperature T_N for figure a) and the values of 2β for figures b).

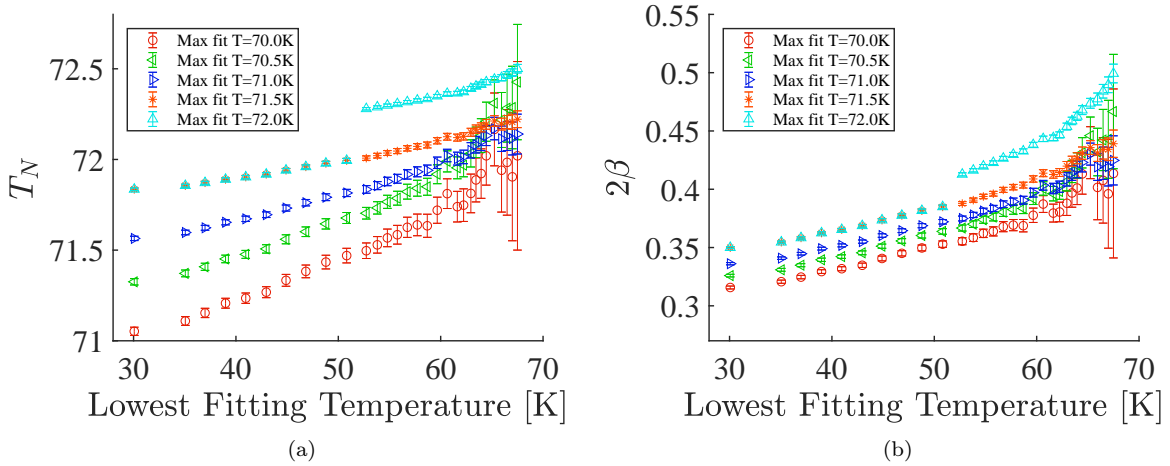


Figure 4.10: *Variational analysis of the temperature fitting range. The color of the points determine the highest temperature of the fitting range used, e.g. the highest temperature used in the fits for all the green points are 70.5K, while the x-axes tells the lowest temperature used in the fits. The left plot has the Néel temperature, T_N , one obtains by fitting a power law to the data in the temperature range from the value on the x-axis to the temperature indicated by the color of the data point. The right plot has the value of 2β . The obtained values of T_N and 2β seem to increase almost linearly with the lowest temperature used in the fits, up until a temperature close to the maximum temperature. See figure 4.12 for a zoomed in version of this area.*

These plots clearly show that the values one can obtain for T_N and β can vary quite substantially given ones choice of data points to include. This clearly shows that great caution should be used when using the method of double logarithmic plots to determine ones data range. Especially a few features show themselves using this method. First there is a general small bump in the values of T_N and β just above using 60K as the lowest temperature in the fit, this shows that the results obtained can be very delicate and vary quite substantially with the addition of just one more data point. An even more extreme example of this is that the data range that has $T = 72K$ (cyan) as the highest temperature give the same results as the range with $T = 71.5K$ (orange) as the highest temperature up until just above 50K after which the cyan data range makes a large jump and parts ways with orange for good. The difference between including the one point or not is substantial and the difference can be seen in figure 4.11, where two fits have been made using 72K as the highest temperature in the fitting range, the red fit does not include the point while the cyan fit does include the point.

Perhaps a more robust method of determining the data range to be fitted

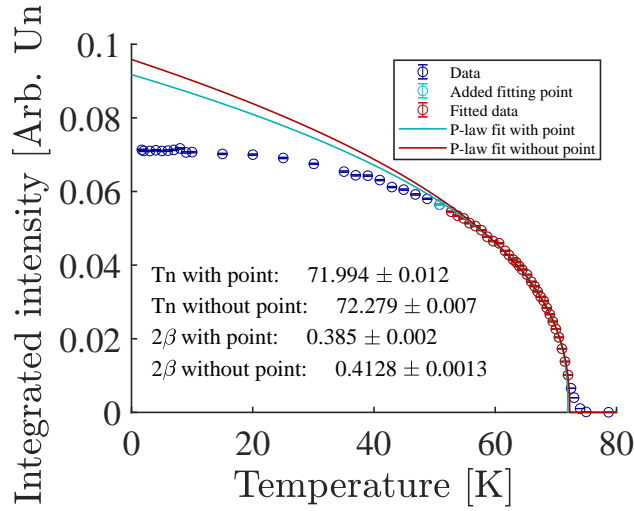


Figure 4.11: *The results from the power law fit can vary a great deal just by including one more point in the fit. This plot shows two fits, the first one in the red uses the red data points only. The cyan fit uses the red data points, but also includes the cyan data point in the fit. Whether the cyan point is included or not changes the values of T_N and 2β by quite a margin. Especially 2β changes by about 7%*

can be found. In general there seem to be a tendency in figure 4.10 that the value of T_N and β that is obtained rises somewhat linearly with the choice of the lower bound of temperature, up to a certain temperature after which the values of T_N and β rises more sharply for a few points, and after this they seem to be more constant and reaches what could be called a plateau, see figure 4.12, which is a zoomed in version of figure 4.10.

A plateau is reached for the data ranges that has a maximum fitted temperature of $T = 70.0K$ (red), $T = 71.0K$ (blue), and $T = 71.5K$ (orange). The green points that has a maximum temperature range of $T = 70.5K$ also show some signs of plateauing, but the final data point makes quite a jump upwards. No plateauing happens for the one that has a maximum fitted temperature of $T = 72K$ (cyan), this could perhaps indicate that $T = 72K$ is above or too close to the Néel temperature.

Since less data points are used in the fit to determine T_N and β the closer the lowest temperature gets to the highest, the uncertainty of the results also increases, so this tendency of plateauing could also just be an artifact of having less data points available. Also the uncertainty is too high in the region where the values of T_N and β plateau, to safely say whether the results show that the temperature ranges that has a maximum below $72K$ plateau at the same level of T_N and β or if they depend on the choice of the maximum temperature chosen.

If they do not depend on the maximum temperature chosen, as long as it is below T_N , then finding this plateau could be an entirely novel method of determining T_N and β , which could be more robust than the double logarithmic plot method. However it would require a larger number of data points close to

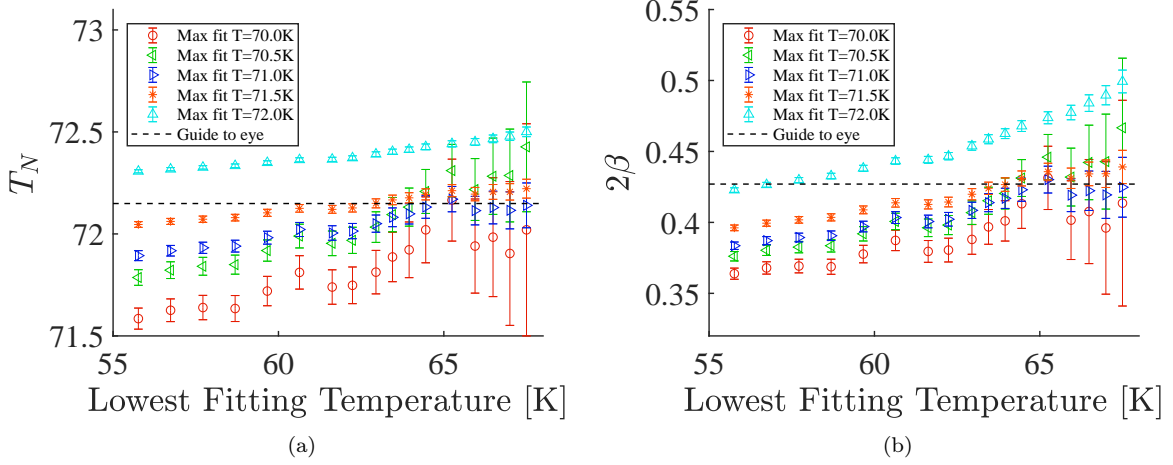


Figure 4.12: Zoomed in version of figure 4.10 showing the values of T_N and 2β one obtain as the lowest fitting temperature approaches the highest one. The tendency changes from resembling a linear trend to a more steep increase in the values found, to a plateau as the lowest fitting temperature comes very close to the highest. The fact that the values of T_N and 2β seems to find a stable plateau might indicate a novel way to determine the temperature range one should use when fitting, as an alternative to the double logarithmic plot method used in figure 4.4. The dashed black line in both plots indicate an estimate where the value of T_N and β would be, if the plateau model explained in the text were used.

the critical temperature to reduce the uncertainty, verify that this plateauing does in fact happen, and to determine T_N and β from it.

Assuming this method does work though, it would probably yield values of T_N and β close to the constant values indicated by the dashed black line in both plots of figure 4.12, meaning that $T_N \approx 72.15$ and $\beta \approx 0.22$. The dashed black line is not a fit, rather an estimate based on the region of plateauing.

4.2 Results of the Inelastic Neutron Scattering Measurements

This section details the findings from the data analysis of the inelastic neutron scattering measurements. The main goal here is to determine whether the excitation energy of the magnons, see section 2.3, depends on the temperature in a similar fashion as the magnetization, meaning that the same critical exponent associated with the magnetization, β , also determines the excitation energy of a magnon close to T_N .

4.2.1 Fitting the magnon

The inelastic neutron scattering scans reveal two distinct magnon modes at low temperatures, see figure 4.13. This is in general agreement with the literature on h -YMnO₃, [43, 53, 54, 55, 56, 3], however 3 modes actually exist, the upper mode is degenerate and is actually two modes as shown by Holm et al in [46] as it splits into two separate modes when an external magnetic field is applied. Since all the experiments in this paper were made with 0 applied field, these two higher modes are generally considered as one in this thesis. At the lowest temperature the lower magnon is situated at an energy transfer of about $\hbar\omega = 2.3$ meV while the upper magnons is at $\hbar\omega = 5.4$ meV. This is in good agreement by the findings of Holm-Dahlin, Chatterji, and Sato [3, 43, 53]. As the temperature is increased the energies of the two magnon modes are lowered with the lowest one seemingly approaching $\hbar\omega = 0$ as the temperature approaches the Néel temperature, but the mode is completely absorbed by the quasi-elastic scattering line close to T_N , because the amplitude of it increases enormously as the temperature approaches T_N . The energy of the higher modes does not go to 0, but the amplitude of it does as T_N is approached.

The data shows the existence of two magnon modes and a central quasi-elastic scattering mode at $\hbar\omega = 0$. The central quasielastic scattering has been fitted to a simple Lorentzian line shape, while the two magnon modes have been fitted to a skewed Gaussian each. The Gaussians are skewed due to a combination of factors, one contributing factor is the instrument resolution function for the momentum transfer, and second, the density of states follow a step function at the minimum magnon mode. These two contributions skew the Gaussians.

$$\begin{aligned}
 I(E) &= I_{Lorentz}(E) + I_{magnon_1}(E) + I_{magnon_2}(E) + Bkg \\
 &= I_L \frac{\sigma_L}{\pi \left(\sigma_L^2 + (E - \mu_L)^2 \right)} \\
 &\quad + \frac{I_{m_1}}{\sigma_{m_1} \sqrt{2\pi}} \exp \left(-\frac{1}{2} \left(\frac{E - \mu_{m_1}}{\sigma_{m_1}} \right)^2 \right) \left[1 + \operatorname{erf} \left(\gamma_{m_1} \frac{E - \mu_{m_1}}{\sigma_{m_1} \sqrt{2}} \right) \right] \\
 &\quad + \frac{I_{m_2}}{\sigma_{m_2} \sqrt{2\pi}} \exp \left(-\frac{1}{2} \left(\frac{E - \mu_{m_2}}{\sigma_{m_2}} \right)^2 \right) \left[1 + \operatorname{erf} \left(\gamma_{m_2} \frac{E - \mu_{m_2}}{\sigma_{m_2} \sqrt{2}} \right) \right] \\
 &\quad + Bkg
 \end{aligned} \tag{4.2.1}$$

for the Lorentzian the fitted parameters are the peak intensity I_L , the center μ_L , and the width σ_L . Each of the skewed Gaussians are fitted with the same

parameters, the subscript $n=1$ denotes the lower magnon mode and the the subscript $n=2$ denotes the higher magnon modes, since we have no applied field, these are just fitted by one function, since they are completely degenerate at 0 applied field. The parameters are I_{m_n} is the peak intensity, μ_{m_n} is the center, the width is σ_{m_n} , and finally γ_{m_n} is the skewness parameter of the skewed Gaussians. In addition a flat background was included in the fitting function. The fits at all temperatures can be seen in figure 4.13. Where the total fit is in red, the greenish line is the skew Gaussian fit of the lower magnon mode, the blue line is the fit of the higher magnon modes, and turquoise is the Lorentzian fit of the quasi-elastic scattering. At temperatures above $T = 71.75\text{K}$ the fitting function, equation 4.2.1, no longer converged to anything meaningful. As such these data series were not fitted. All the fitting parameters are plotted in figure A.1 found in the appendix.

When fitting a skewed Gauss the position of the center of the Gaussian is different from the position of the peak of the curve, the difference is dependent on the skewness γ . In this work the position of the peak was numerically determined using the maximum point of the given fit to a skew Gaussian.

4.2.2 Finding β using the magnon

It is expected from spin wave theory in an anisotropic Heisenberg model that the excitation gap, Δ , of the low magnon mode is proportional to the effective spin $\Delta \propto \langle S \rangle$. It is well documented in the literature that the spin waves of $h\text{-YMnO}_3$ can be reasonably modeled by a Heisenberg Hamiltonian including in and out of plane anisotropies [43][53]. Therefore it is expected that the excitation gap also shows a power law critical behavior in the vicinity of T_N

$$\Delta \propto \left(\frac{T_N - T}{T_N} \right)^\beta \quad (4.2.2)$$

similar to the magnetization, see equation 4.1.1. The only difference being that the exponent here is just β instead of 2β . Fitting this power law to the temperature vs the excitation gap yields figure 4.14. The fit is only made to the data in the same temperature range as the magnetization data, figure 4.5, to ensure that the findings can be easily compared between the two. This method gives a value for $T_N = 73 \pm 2\text{K}$, which is consistent with the findings of T_N from the magnetization within one standard deviation. The value of $\beta = 0.28 \pm 0.08$ is consistent with the previously found value of $\beta = 0.179 \pm 0.002$ within two standard deviations. The uncertainties here are fairly high due to the small number of data points within the fitted temperature range, but the data certainly supports that the critical exponent β is similar for the temperature dependence of the magnetization and the excitation gap of the lower magnon mode. This value agrees well with that found by Holm-Dahlin et al [3].

4.2.3 Novel critical exponents

The fits in figure 4.13 showed that the gap Δ exhibited power law behavior in the vicinity of the Néel temperature. However a closer look at the fitting parameters in figure A.1 shows that the intensity and width of the Lorentzian fitting function used to determine the properties of the quasi-elastic scattering

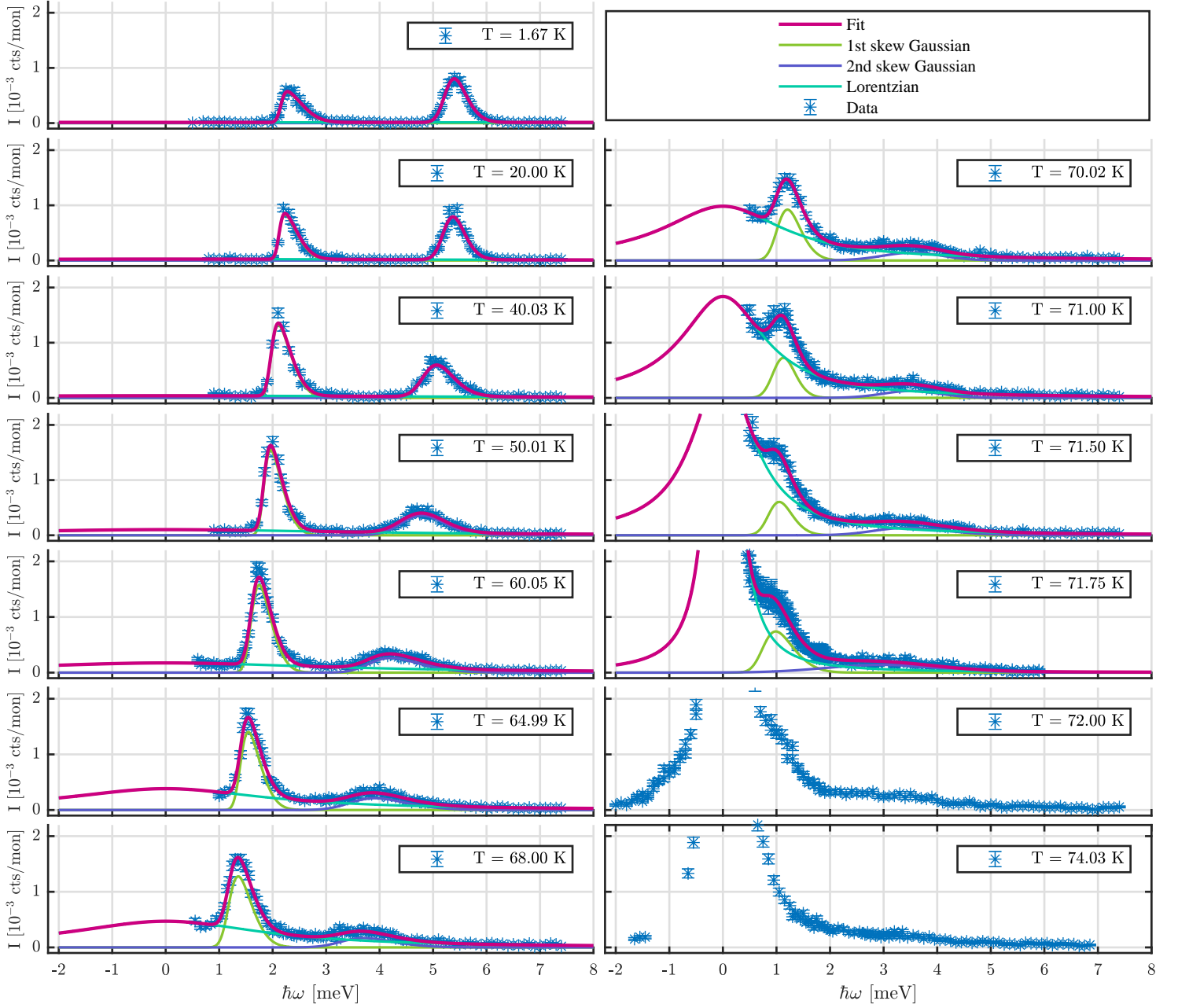


Figure 4.13: *Fits of the inelastic neutron scattering data. The two magnon modes are fitted to skewed Gaussians, where the lower magnon mode is in dirty green, and the higher magnon modes is in blue. The quasi-elastic neutron scattering data is fitted to a turquoise Lorentzian shape and the sum of the fits are in red. The fitting function can be seen in equation 4.2.1. As the temperature rises the quasi-elastic scattering increases, while the peak intensity of the higher magnon modes decreases. The energy transfer of the lower magnon mode goes from $\hbar\omega = 2.3$ meV to 0 as the temperature approaches T_N .*

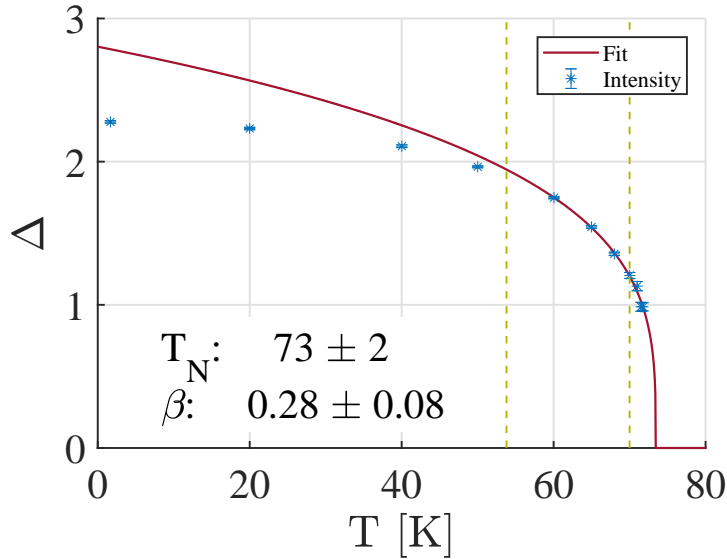


Figure 4.14: Power-law fit of the excitation gap, Δ , vs temperature. The fitted function is 4.2.2. The critical exponent $\beta = 0.28 \pm 0.08$ is similar to the value of β found from the relation between magnetization and temperature. The Néel temperature $T_N = 73 \pm 2K$ is also in agreement with previous findings in this work.

centered at $\hbar\omega = 0$ meV could also have power law like behavior. Normally the intensity and width of this scattering is measured in \mathbf{q} -space and fitted to power laws giving the critical exponents γ and ν respectively as was done above. However no prior examples of fitting the intensity and width in energy-space have been found in the literature search, nor any theoretical predictions of this. In figure 4.13 it is clear that the quasi-elastic scattering centered at $\hbar\omega = 0$ meV rises in intensity as the temperature approaches T_N . This rise in intensity of the Lorentzian part of equation 4.2.1 were fitted to a power law similar to equation 4.1.2, with the new critical exponent ζ

$$I_{Critical} \propto \left(\frac{T_N - T}{T_N} \right)^{-\zeta} \quad (4.2.3)$$

This power law fits the data well and can be seen in figure 4.15 giving the following values for $T_N = 74.0 \pm 0.5$ and $\zeta = 0.72 \pm 0.07$. This value of T_N is within one standard deviation of the value of $T_N = 73 \pm 2$ found using the excitation gap of the magnon, but quite far from $T_N = 71.48 \pm 0.04$ found from the magnetization. The value of the new critical exponent $\zeta = 0.72 \pm 0.07$ is significantly smaller than those usually found for γ , see table 4.2, so while both of these critical exponents come from the intensity of the critical scattering they do not seem to be related based on this data.

The evolution of the width of the Lorentzian of the quasi-elastic neutron scattering centered at $\hbar\omega = 0$ as the temperature approaches T_N were also fitted to a power law. In a similar manner to ζ a power law with a new critical

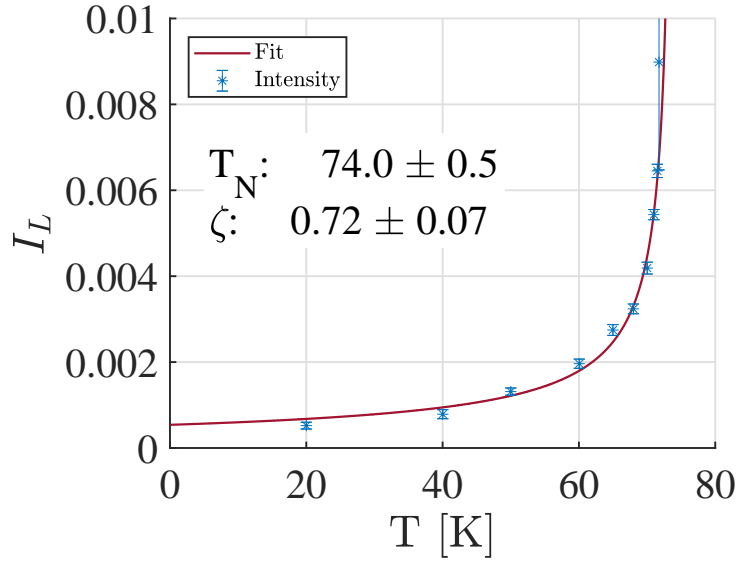


Figure 4.15: Plot of the peak intensity of the quasi-elastic scattering I_L . The intensity rises sharply as the temperature approaches the temperature of the critical phase transition T_N . The fit to the data is the power law function given in equation 4.1.2. The following values are found $T_N = 74.0 \pm 0.5$ and $\zeta = 0.72 \pm 0.07$.

exponent ρ is defined as

$$HWHM \propto \left(\frac{T_N - T}{T_N} \right)^\rho. \quad (4.2.4)$$

This power law relation resembles that of ν used to fit the width of the elastic critical scattering in \mathbf{q} -space, see equation 4.1.3. The fit of the HWHM of the Lorentzian can be seen in figure 4.16 and seem to fit the data well. The value of $T_N = 71.79 \pm 0.04$ is in general agreement with previous results, interestingly it is closer to the magnetization result of $T_N = 71.48 \pm 0.04$, rather than the values of T_N found previously from the inelastic neutron scattering data.

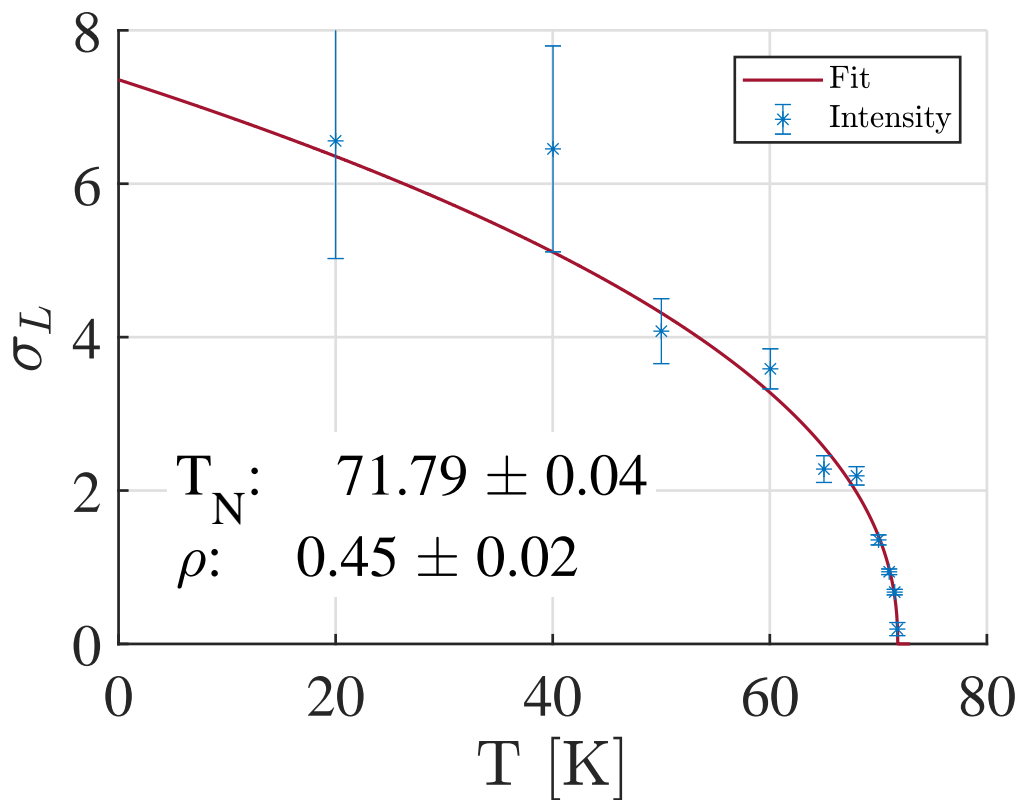


Figure 4.16: The HWHM of the quasi-elastic scattering, σ_L , decreases as T_N is approached. The data has been fitted to the power law function in equation 4.1.3 giving the following values for $T_N = 71.79 \pm 0.04$ and $\rho = 0.45 \pm 0.02$.

Table 4.2: Table of relevant critical exponents for this thesis. β is the critical exponent for the magnetization \mathbf{M} , γ is the critical exponent for the magnetic susceptibility, and ν is the critical exponent for the correlation length [13]. The novel exponents ζ and ρ are presently just measured in the current work, but their significance remain unknown.

Theoretical models		T_N [K]	β	γ	ν	ζ	ρ
2D 3d XY			0.345	1.316	0.669	-	-
1D 3d Ising			0.326	1.2378	0.6312	-	-
1D 2d Ising			0.125	1.75	1	-	-
3D 3d Heisenberg			0.367	1.388	0.707	-	-
Mean Field			0.5	1	0.5	-	-
Experiments							
Ω	Holm-Dahlin et al. [3] Elastic data	72.11 ± 0.05	0.206 ± 0.003	-	-	-	-
	Holm-Dahlin et al. [3] Inelastic data	72.4 ± 0.3	0.24 ± 0.02	-	-	-	-
	Chatterji et al. [30]	69.89 ± 0.05	0.295	0.97	0.45	-	-
	Roessli et al. [41]	72.1 ± 0.05	0.187	-	0.57	-	-
	Kawamura [47]		0.25	1.1	0.53	-	-
Present work							
Elastic data		71.48 ± 0.04	0.179 ± 0.002	$1.063 \pm 0.002 (> T_N)$	$4.1 \pm 1.0 (> T_N)$	-	-
				$1.12 \pm 0.02 (< T_N)$	$6.3 \pm 0.2 (< T_N)$	-	-
Inelastic data Δ		73 ± 2	0.28 ± 0.08	-	-	-	-
Inelastic data I_L		74.0 ± 0.5	-	-	-	0.72 ± 0.07	-
Inelastic data σ_L		71.79 ± 0.04	-	-	-	-	0.45 ± 0.02

Chapter 5

Summarizing Discussion and Conclusion

5.1 Summary of the Results

The measured values of the Néel temperature, T_N , and the critical exponents β , γ , and ν in addition to the previous results by other studies found in table 3.1 are all included in table 4.2 as well as the new exponents ζ and ρ unique to this study.

The values obtained for T_N matches the results of previous studies well, all lying in the range from 71.4K to 74K. For the elastic neutron scattering data the value of β matches the one found by Roessli et al nicely, while γ is very close to that expected from mean field theory. ν on the other hand is very far from both theoretical models and previous studies, but as previously stated in section 4.1.4 this could be due to the competing interactions due to frustration that create a highly extended critical range as explained in the article by Janas et al [52].

The value of β from the inelastic neutron scattering measurements matches well with the results obtained by Chatterji et al. The meaning of the new exponents ζ and ρ , related to the intensity and width of the quasi-elastic scattering centered at $\hbar\omega = 0$ respectively, are unknown. It is however, remarkable how well the width of the critical scattering measured in \mathbf{q} by Chatterji et al matches the evolution of the width in energy measured in this work.

in section 2.5.4 several scaling laws between various critical exponents were introduced. Due to the fact that the values obtained for ν cannot be trusted as discussed above, the scaling laws that include ν , such as equation 2.5.24 and 2.5.26, are not expected to give meaningful results. The critical exponent for the specific heat, α however, only depend on β and γ . To calculate α equation 2.5.27 can be reformed into

$$\alpha = 2 - 2\beta - \gamma \tag{5.1.1}$$

which yields $\alpha = 0.52$. This is a quite high value compared to the results by Tachibana et al. [57] measured the specific heat capacity as a function of temperature. The specific heat capacity were measures by a relaxation method

using a PPMS. Tachibana et al report a value of $\alpha = -0.16$ which correspond well to a the expected value of $\alpha = -0.12$ in the standard Heisenberg model.

5.2 The Néel Temperature

In this thesis the Néel temperature have been measured in several ways, both with elastic and inelastic neutron scattering. The signal strength of the elastic neutron scattering data is significantly higher than of the inelastic. Therefore the value of $T_N = 71.48 \pm 0.04$ obtained from the elastic neutron scattering data will be considered the most reliable estimate of the critical temperature in this work. The reliability of the log-log plot method to determine the critical range is a fair method, though one that should be used cautiously as discussed in section 4.1.5 and later in section 5.4. The critical scattering close to T_N were fitted such that the temperature dependency of the magnetization could be fitted all through the critical range as seen in figure 4.7 and 4.8. Fitting the power-law relation all the way to T_N in this fashion makes the values obtained for T_N and also β from the elastic neutron scattering data more reliable.

The results obtained here generally agree well with other results reported in the literature, especially that of Roessli et al. and Holm-Dahlin et al. [41, 3].

The study by Holm-Dahlin et al. [3] is based on the same data, and thus is expected to agree well with this study. Some differences are present though Holm-Dahlin et al. reports a slightly higher T_N for their elastic data. However this discrepancy is easily explained by them having a chosen a fitting range for their power law of 60 – 71.2 K while the one used in this thesis was from 53.8 – 70.0 K. From figures 4.10 and 4.12 in this thesis, their result for $T_N = 72.11$ K is also obtained if the same fitting range is used. Interestingly Holm-Dahlin et al. have hit the small 'bump' in T_N that happens when the minimum temperature of the fitting range is just around 60K, had they used a slightly lower or higher lowest fitting temperature, they would most likely have obtained a fractionally lower value of T_N .

There is quite a difference between the optimal fitting range used in this work and in the article by Holm-Dahlin et al. [3] despite the analysis being done on the same data. In their article they describe the log-log method as a robust method, however the rather large difference between their fitting range and the one used in this work questions this claim.

Another difference between the analysis conducted here and that of Holm-Dahlin is that they used Gaussian line-shapes for all their fits, while Voigts have been used here. The Voigt function is superior in fitting the data from RITA-II as demonstrated in table 4.1. This gives this study the advantage that with a better fitted line-shape of the resolution function deviations from this will be more easily identified. This can perhaps explain why a longer fitting range was achieved in this work compared to theirs and why some critical scattering were found in this work.

Chatterji et al. [43] reports a significantly lower $T_N = 69.89$ K compared to this analysis. Their experiment however were done on a thermal two-axis diffraction spectrometer as opposed to a cold triple axis spectrometer. Curiously they do not show the existence of any critical scattering close to T_N in

figures 2 a) and b) of their article. This is in contrast to the presence of critical scattering found in this work as can be seen in figures 4.5 through 4.8. It is not clear why they do not see any critical scattering, however there seems to be a quite significant difference in both method and analysis that it is perhaps not surprising that the results they obtain differ from those found in this thesis.

5.3 Critical Exponents

Several critical exponents were computed in this thesis. Primarily β , γ , and ν from power law fits to the magnetization, the intensity of the critical scattering, and the width of the critical scattering respectively. In addition a value of α were determined from a scaling law.

Both $\beta = 0.179 \pm 0.002$ as well as $\gamma = 1.063 \pm 0.002$ above and $\gamma = 1.12 \pm 0.02$ below T_N respectively, fits decently with previous studies though not the same ones. β is, like the critical temperature, in general agreement with the studies of both Roessli and Holm-Dahlin while γ is quite close to the value found by Chatterji et al. and Kawamura. Neither Roessli nor Holm-Dahlin have determined γ however, as such no comparison to these studies can be made for γ .

Both the value above T_N of $\nu 4.1 \pm 1.0$ and below $\nu = 6.3 \pm 0.2$ found in this work is much higher than should be theoretically possible, and does not remotely agree with anything reported in the literature. It is most likely due to some error in the methodology used in this thesis, and the value of ν found here should not be given any credence.

In general the values of the critical exponents found here does not support assigning any known universality class to h -YMnO₃. As such this study agrees with Holm-Dahlin et al. [3] and the yet to be published study by Janas et al. [52] that a new universality class is needed for triangular anti-ferromagnets.

The value of $\beta = 0.28 \pm 0.08$ from the inelastic neutron scattering data associated with the excitation gap of the lower magnon mode, matches that of the value of $\beta = 0.179 \pm 0.002$ associated with the magnetization from the elastic data within two standard deviations. As such this work corroborates the conclusion by Holm-Dahlin et al. [3] that the two β 's are indeed the same.

In addition two completely new critical exponents have been determined in this work, namely $\zeta = 0.72 \pm 0.07$ and $\rho = 0.45 \pm 0.02$ which are related to the intensity of the quasi-elastic scattering centered at $\hbar\omega = 0$ and the width of the same. As these are computed in energy transfer $\hbar\omega$ and not in \mathbf{q} these are to the authors best knowledge completely novel critical exponents, though they do mimic the function of γ and ν in \mathbf{q} .

The consequence, or indeed usefulness, of these are currently unknown and hard to speculate on, but perhaps the addition of these and perhaps more critical exponents could lead to some interesting new revelations eventually. Curiously the value of ρ is close to the value of ν found by both Chatterji and Roessli, since both ρ and ν relates to the width of scattering there may be a connection, but this is purely speculation at this point and beyond the scope of this thesis.

5.4 The Fitting Method in Light of the Variational Analysis

Perhaps the most immediately relevant new result of this work is the variational analysis of the fitting parameters from section 4.1.5. This show that one should use caution when applying the log-log plot method in determining the critical range of neutron scattering data. The result of an analysis is quite sensitive to the exact critical range that is chosen, as such the log-log plot method is not a very robust method. This is exemplified in the difference between the results obtained here and those by Holm-Dahlin et al. [3] even though both studies are based on the same dataset. An alternative approach to measuring the critical range is to measure the critical scattering away from a Bragg-peak as a function of temperature, however doing this will cause the signal strength to be weaker.

The variational analysis however also indicated that a new method to determine the critical range might exist. In this new method one selects a given maximum fitting temperature and then plots the results of either the critical temperature or β versus the lowest temperature in the fitting range, which is then systematically varied. This can then be repeated for a new maximum fitting temperature allowing one to systematically vary the fitting range and computing all the possible values of the critical temperature and β that can be obtained from the data.

As shown in figure 4.12 there seems to be a tendency that the result obtained for both T_N and β quickly increases as the lowest fitting temperature rises after which the results converges to a specific value and appear to plateau. The plateauing happens for all maximum fitting temperatures, except 72 K (cyan), at a lowest fitting temperature of about ~ 64 K. Due to less and less data points being used in the fits as the lowest fitting temperature approaches that of the maximum fitting temperature the uncertainty gets rather large, so it is not clear whether this is a real effect or not.

If the plateau is an indication of a true critical range, then the critical range used both here and by Holm-Dahlin et al. [3] to fit the magnetization as a function of temperature to a power-law are too large and especially begins at a too low temperature. The fact that the obtained results using the highest fitting temperature of 72 K does not plateau is very interesting. 72 K is very close to T_N , as such the lack of a plateau might indicate that the maximum fitting temperature is too high.

A new approach could then be devised based on this analysis where the lower bound on the critical region is found by the onset of plateauing while the upper bound is set by the highest maximum fitting temperature where plateauing still occurs. This method, if valid, could perhaps be a more robust method to determine the critical range. The supposed true critical range in this data can then be gauged from this method and would be roughly 64-71 K. An estimate of where this method would find the values are provided by the dashed black line in figure 4.12 and would yield approximately $T_N \approx 72.15$ and $\beta \approx 0.22$. Both of these values are somewhat higher than those found by the log-log plot method in this work, though further study is required to validate if these are more correct than those otherwise reported here.

Chapter 6

Outlook

The critical exponents found here and in other studies do not correspond to any known universality class. As such further theoretical modeling is needed to find a new universality class for triangular frustrated magnets such as h -YMnO₃, in addition further studies of all the critical exponents of h -YMnO₃ will aid in this endeavor.

Further study would be needed to confirm whether the proposed method to determine the critical range is useful or not. In this work the uncertainty of the fitted values of T_N and β at the onset of the proposed plateauing were becoming too large to assess whether the effect is real or not.

A further study to validate this method would need a good deal more measurements at temperatures from perhaps 10 or 15 K below T_N all the way to the critical temperature such that the uncertainty can be decreased sufficiently to see if this plateauing does in fact occur.

Finally it would be interesting to see what can come from the novel critical exponents ζ and ρ if anything. This would require both considerable experimental and theoretical work, to investigate the nature of critical exponents related to inelastic neutron scattering .

Chapter 7

Bibliography

- [1] Gustau Catalan and James F. Scott. Physics and applications of bismuth ferrite. *Advanced Materials*, 21(24):2463–2485, 2009.
- [2] Seoungsu Lee, W. Ratcliff, S-W. Cheong, and V. Kiryukhin. Electric field control of the magnetic state in BiFeO₃ single crystals. *Applied Physics Letters*, 92(19):192906, 2008.
- [3] Sonja Holm-Dahlin, Sofie Janas, Andreas Kreisel, Ekaterina Pomjakushina, Jonathan White, Amy Fennell, and Kim Lefmann. The magnetic phase transition and universality class of h-ymno₃ and h-(y0.98 eu0.02)mno₃ under zero and applied pressure. *Quantum Beam Science*, 2:16, 08 2018.
- [4] Stephen Kittel. *Introduction to Solid State Physics*. 8th ed. Wiley, 2005.
- [5] Wikipedia. Crystal structure. https://en.wikipedia.org/wiki/Crystal_structure, 2018. [Online; accessed 16-august-2018].
- [6] Massa Werner. *Crystal Structure Determination*. Springer, 2004.
- [7] Turi K. Schäffer. Phonon-magnon coupling in frustrated and multiferroic h-YMnO₃. Master’s thesis, University of Copenhagen, 2014.
- [8] Wikipedia. Brillouin zone. https://en.wikipedia.org/wiki/Brillouin_zone, 2018. [Online; accessed 16-august-2018].
- [9] Kim Lefmann. Neutron scattering: Theory, instrumentaion, and simulation, 2016.
- [10] Sonja L. Holm. *Neutron scattering investigations of correlated electron systems and neutron instrumentation*. PhD thesis, University of Copenhagen, 2016.
- [11] Stephen Blundell. *Magnetism in Condensed Matter*. Oxford University Press, 2001.
- [12] Leon Balents. Spin liquids in frustrated magnets. *Nature*, 464:199–208, 03 2010.
- [13] Malcolm F. Collins. *Magnetic Critical Scattering*. Oxford University Press, 1989.

- [14] B. T. M. Willis and C. J. Carlile. *Experimental Neutron Scattering*. Oxford University Press, 2009.
- [15] G. L. Squires. *Introduction to the Theory of Thermal Neutron Scattering*. 3rd ed. Cambridge University Press, 1978.
- [16] T. Chatterji. *Neutron Scattering from Magnetic Materials*. 1st ed. Elsevier, 2006.
- [17] Bas Van Aken, Jean-Pierre Rivera, Hans Schmid, and Manfred Fiebig. Observation of ferrotoroidic domains. *Nature*, 449:702–5, 11 2007.
- [18] J. Valasek. Piezo-electric and allied phenomena in rochelle salt. *Phys. Rev.*, 17:475–481, Apr 1921.
- [19] Aleksandr P Pyatakov and Anatoly Zvezdin. Magnetoelectric and multi-ferroic media. *Physics-Uspokhi*, 55:557, 06 2012.
- [20] Nicola A. Hill. Why are there so few magnetic ferroelectrics? *The Journal of Physical Chemistry B*, 104(29):6694–6709, 2000.
- [21] K.F. Wang, J.-M. Liu, and Z.F. Ren. Multiferroicity: the coupling between magnetic and polarization orders. *Advances in Physics*, 58(4):321–448, 2009.
- [22] D. Khomskii. Classifying multiferroics: Mechanisms and effects. *Physics Online Journal*, 2:20, March 2009.
- [23] Neil G. Connelly, Ture Damhus, Richard M. Hartshorn, and Alan T. Hutton. *Nomenclature of Inorganic Chemistry*. RSC Publishing, 2005.
- [24] Hasung Sim, Joosung Oh, Jaehong Jeong, Manh Duc Le, and Je-Geun Park. Hexagonal $RMnO_3$: a model system for two-dimensional triangular lattice antiferromagnets. *Acta Crystallographica Section B*, 72(1):3–19, Feb 2016.
- [25] Jonas Okkels Birk. Kritiske faseovergange i coo nanopartikler studeret med neutronspreddning. Master’s thesis, University of Copenhagen, 2009.
- [26] L. D. Landau and E. M. Lifshitz. *Statistical Physics*. 3rd ed. Elsevier, 2013.
- [27] Paul Scherrer Institut. Sinq homepage. <https://www.psi.ch/sinq/>. [Online; accessed 16-august-2018].
- [28] Paul Scherrer Institut. RITA-II. <https://www.psi.ch/sinq/ritaii/rita-ii/>. [Online; accessed 16-august-2018].
- [29] U. Stuhr, B. Roessli, S. Gvasaliya, Henrik Ronnow, Uwe Filges, D. Graf, A. Bollhalder, D. Hohl, R. Bürge, M. Schild, L. Holitzner, Kaegi C, P. Keller, and T. Mühlebach. The thermal triple-axis-spectrometer eiger at the continuous spallation source sinq. *Nuclear Instruments and Methods in Physics Research Section A: Accelerators, Spectrometers, Detectors and Associated Equipment*, 853, 02 2017.
- [30] Tapan Chatterji. *Neutron Scattering from Magnetic Materials*. Elsevier, 2005.

- [31] Donald H. Perkins. *Introduction to High Energy Physics*. 4th ed. Cambridge University Press, 2000.
- [32] Jens Jensen and Allan R. Mackintosh. *Rare Earth Magnetism*. Oxford Science Publications, 1991.
- [33] Kenneth S. Krane. *Introductory Nuclear Physics*. 3rd ed. Wiley, 1987.
- [34] Weston M. Stacey. *Nuclear Reactor Physics*. Wiley, 2007.
- [35] Hans Maier-Leibnitz Zentrum. MLZ source. <https://mlz-garching.de/englisch/neutron-research/neutron-source.html>. [Online; accessed 14-september-2018].
- [36] Paul Scherrer Institut. SINQ source. <https://www.psi.ch/media/the-sinq-neutron-source>. [Online; accessed 14-september-2018].
- [37] JJ X-ray. Jj x-ray homepage. <https://www.jjxray.dk/>. [Online; accessed 26-september-2020].
- [38] Z. Yamani, Z. Tun, and D. H. Ryan. Neutron scattering study of the classical antiferromagnet MnF_2 : a perfect hands-on neutron scattering teaching coursespecial issue on neutron scattering in canada. *Canadian Journal of Physics*, 88(10):771–797, 2010.
- [39] *Diffraction Lineshapes*, pages 423–456. Springer Berlin Heidelberg, Berlin, Heidelberg, 2008.
- [40] Alexandra S. Gibbs, Kevin S. Knight, and Philip Lightfoot. High-temperature phase transitions of hexagonal YMnO_3 . *Phys. Rev. B*, 83:094111, Mar 2011.
- [41] B. Roessli, S. N. Gvasaliya, E. Pomjakushina, and K. Conder. Spin fluctuations in the stacked-triangular antiferromagnet YMnO_3 . *Journal of Experimental and Theoretical Physics Letters*, 81(6):287–291, Mar 2005.
- [42] Mario Poirier, Francis Laliberté, Loreynne Pinsard-Gaudart, and Alexandre Revcolevschi. Magnetoelastic coupling in hexagonal multiferroic YMnO_3 using ultrasound measurements. *Phys. Rev. B*, 76:174426, Nov 2007.
- [43] Tapan Chatterji, S. Ghosh, A. Singh, L. P. Regnault, and M. Rheinstädter. Spin dynamics of YMnO_3 studied via inelastic neutron scattering and the anisotropic hubbard model. *Phys. Rev. B*, 76:144406, Oct 2007.
- [44] T. Lancaster, S. J. Blundell, D. Andreica, M. Janoschek, B. Roessli, S. N. Gvasaliya, K. Conder, E. Pomjakushina, M. L. Brooks, P. J. Baker, D. Prabhakaran, W. Hayes, and F. L. Pratt. Magnetism in geometrically frustrated YMnO_3 under hydrostatic pressure studied with muon spin relaxation. *Phys. Rev. Lett.*, 98:197203, May 2007.
- [45] Seongsu Lee, Alexander Pirogov, Misun Kang, Kwang-Hyun Jang, M Yone-mura, Tomohiro Kamiyama, S-W Cheong, Fabia Gozzo, Namsoo Shin, H Kimura, Y Noda, and Je-Geun Park. Giant magneto-elastic coupling in multiferroic hexagonal manganites. *Nature*, 451:805–8, 03 2008.

- [46] Sonja Holm-Dahlin, Andreas Kreisel, Turi Kirstine Schäffer, August Bakke, Mads Bertelsen, Ursula Bengård Hansen, Maria Retuerto Millan, J. Larsen, D. Prabhakaran, P.P. Deen, Z. Yamani, Jonas Okkels Birk, U. Stuhr, Ch. Niedermayer, A.L. Fennell, Brian Møller Andersen, and Kim Lefmann. Magnetic ground state and magnon-phonon interaction in multiferroic h-y-mno₃. *Physical Review B (Condensed Matter and Materials Physics)*, 97(13), 2018.
- [47] Hikaru Kawamura. Review article: Universality of phase transitions of frustrated antiferromagnets. *Journal of Physics-condensed Matter - J PHYS-CONDENS MATTER*, 10:4707–4754, 06 1998.
- [48] V. Goian, S. Kamba, C. Kadlec, D. Nuzhnyy, P. Kužel, J. Agostinho Moreira, A. Almeida, and P.B. Tavares. Thz and infrared studies of multiferroic hexagonal Y_{1-x}Eu_xMnO₃ ($x = 0 - 0.2$) ceramics. *Phase Transitions*, 83(10-11):931–941, 2010.
- [49] Sonu Namdeo. *Synthesis and characterization of novel perovskite multiferroics*. PhD thesis, Devi Ahilya University, 2014.
- [50] C.R.H. Bahl, P. Andersen, S.N. Klausen, and K. Lefmann. The monochromatic imaging mode of a rita-type neutron spectrometer. *Nuclear Instruments and Methods in Physics Research Section B: Beam Interactions with Materials and Atoms*, 226(4):667 – 681, 2004.
- [51] C.R.H. Bahl, K. Lefmann, A.B. Abrahamsen, H.M. Rønnow, F. Saxild, T.B.S. Jensen, L. Udby, N.H. Andersen, N.B. Christensen, H.S. Jakobsen, T. Larsen, P.S. Häflicher, S. Streule, and Ch. Niedermayer. Inelastic neutron scattering experiments with the monochromatic imaging mode of the rita-ii spectrometer. *Nuclear Instruments and Methods in Physics Research Section B: Beam Interactions with Materials and Atoms*, 246(2):452 – 462, 2006.
- [52] Sofie Janas, Jakob Lass, Ana Elena Țuțueanu, Morten Haubro, Christof Niedermayer, U. Stuhr, Guangyong Xu, Dharmalingam Prabhakaran, Pascale Deen, Sonja Holm-Dahlin, and Kim Lefmann. Classical spin liquid or extended critical range in h-y-mno₃?, 06 2020.
- [53] T. J. Sato, S. H. Lee, T. Katsufuji, M. Masaki, S. Park, J. R. D. Copley, and H. Takagi. Unconventional spin fluctuations in the hexagonal antiferromagnet YMnO₃. *Phys. Rev. B*, 68:014432, Jul 2003.
- [54] Franz Demmel and Tapan Chatterji. Persistent spin waves above the néel temperature in YMnO₃. *Phys. Rev. B*, 76, 12 2007.
- [55] Stéphane Pailhès, Xavier Fabreges, Louis-Pierre Regnault, L. Pinsard-Godart, Isabelle Mirebeau, F. Moussa, Martine Hennion, and Sylvain Petit. Hybrid goldstone modes in multiferroic YMnO₃ studied by polarized inelastic neutron scattering. *Physical Review B - PHYS REV B*, 79, 04 2009.
- [56] Sylvain Petit, F Moussa, Martine Hennion, Stéphane Pailhès, L. Pinsard-Godart, and A. Ivanov. Spin phonon coupling in hexagonal multiferroic YMnO₃. *Physical review letters*, 99:266604, 01 2008.

- [57] Makoto Tachibana, Junichiro Yamazaki, Hitoshi Kawaji, and Tooru Atake. Heat capacity and critical behavior of hexagonal YMnO₃. *Phys. Rev. B*, 72, 08 2005.

Appendix A

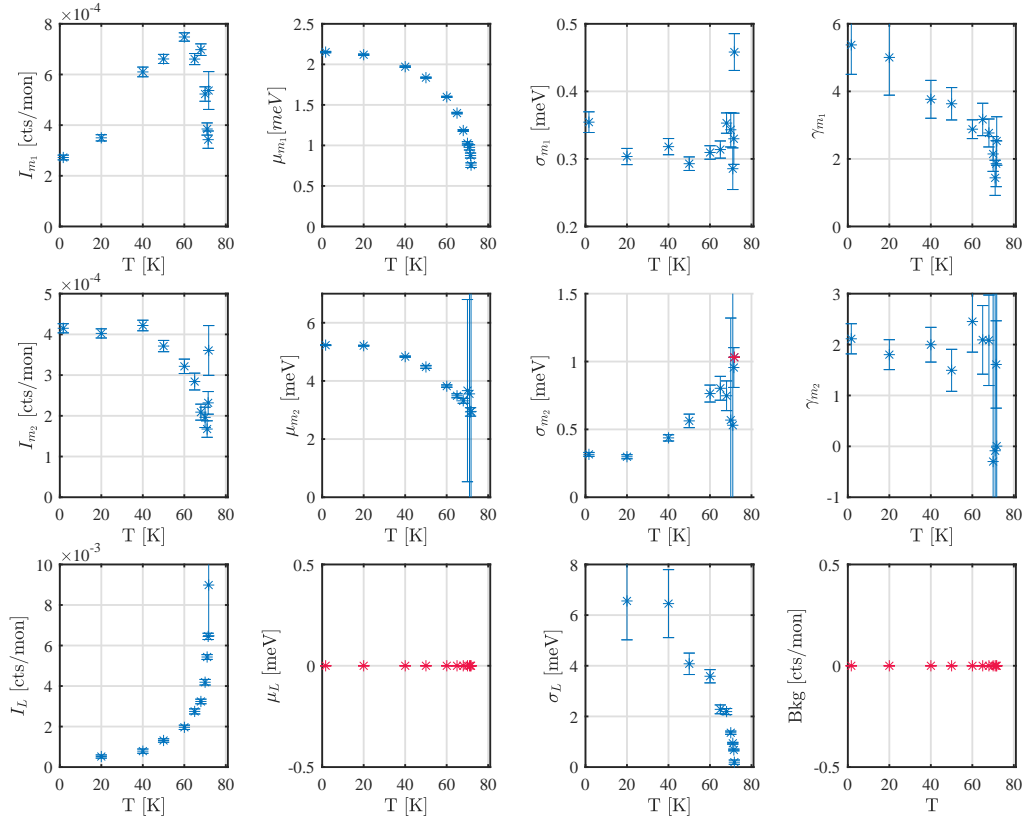


Figure A.1: All fitting parameters for the fits seen in figure 4.13 using the fitting function in equation 4.2.1. Blue indicates free parameters while red indicates locked parameters. The center of the quasi-elastic scattering is locked at $\hbar\omega = 0$ meV for all fits. The background were also locked to 0 because whenever the fitting routine was allowed to fit with a nonzero background it consistently found a negative background, which is physically impossible. The final fit at $T = 71.75K$ also had a locked width of the higher magnon mode, this was done because otherwise the fit in general would not converge to anything meaningful. It was assumed to be the same as the fit at $T = 71.50K$.